

POLITECNICO DI TORINO

Automotive engineering master's degree course

Master's degree thesis



**Lumped parameter models and computational fluid dynamics
simulations for the design and optimization of cooling systems
for high-performance electric vehicle battery packs**

Supervisor

Professor Andrea Tonoli

Candidate

Mattia Larini

Co-supervisor

Engineer Ugo Gillone

October 2021

Acknowledgments

I would like to thank Professor Andrea Tonoli for support, great professionalism and kindness during the most important period of my university career.

A special thanks to all the Podium staff for the support and kindness received. In particular, I would like to underline the great availability and professionalism of the engineers Ugo Gillone and Jonathan Brivio. Special thanks also to the CEO Francesco Monti and engineer Federico Micca.

I would also like to thank Luca Ravera, Sandeep Patil and all ESI Group employees for licensing “Visual-Environment” an Intelligent and Advanced User Interface for OpenFOAM. All the fluid dynamics and thermo-fluid dynamics simulations present in the thesis were carried out using the ESI software.

I would like to thank Professor Renzo Arina for CFD advice.

A heartfelt thanks goes to Gianmaria Aghem, pilot and owner of BLIZZ PRIMATIST. Thanks for your kindness, cheerfulness and helpfulness.

Last but not least, I want to thank my parents Anna Rita and Marco, my love Eleonora, my friends Maria Vittoria, Federico, Luca, Lorenzo, Giulio, Anna Maria, Francesca, Alessandro, Stefano and all relatives and other friends who supported me during my university career. If I have done or will ever do something right in my life, it surely has been or will be thanks to you.



Abstract

This thesis focuses on the use of computational thermo-fluid dynamics simulations and lumped parameter models for the design, optimization, and verification of two cooling systems for high-performance electric vehicle battery packs.

The discussion chronologically follows the work carried out during the pre-graduate internship at the engineering design company Podium Advanced Technologies.

The first chapter of the paper describes the main cooling systems for battery packs of electric vehicles, used in the automotive industry, identifying the positive and critical aspects.

The second chapter describes the design of the air-cooling system for the battery pack of the BLIZZ PRIMATIST vehicle. The discussion begins by identifying the project objective and describing the main characteristics of the vehicle. Subsequently, the effect of natural convection on the cooling of the battery pack with and without box cover is analysed through experimental tests. The discussion continues by describing the first configuration of the battery cooling system and the relative lumped parameter model for verifying the thermal behaviour. Subsequently, the final configuration and the related lumped parameter model used to predict the effectiveness of cooling is presented. The chapter concludes with the comparison between the maximum cell temperature predicted by the thermal model and that obtained experimentally on the day of the test on the track.

The third chapter describes the balancing and validation process of the hydraulic system for cooling the battery pack of a high-performance electric vehicle. The battery pack uses a mixture of water and ethylene glycol that flows inside flexible elements to cool the cells. The chapter opens with the identification of the project objective; subsequently, the CFD simulations used to determine the pressure drop along the coolers are described. The discussion continues by describing the characteristics of a simplified battery pack used to validate the hydraulic and thermal results obtained through CFD simulations and lumped parameter models. The flow distribution along the coolers of the simplified battery pack is then evaluated. The chapter continues with the description of the thermo-fluid dynamics simulation and the lumped parameter thermal model used to simulate the maximum cell temperature reached.

Validation of thermal simulation results is done by testing the simplified battery pack. The chapter concludes by identifying the pressure drop across the entire battery pack and describing the lumped hydraulic model used to balance the coolant flow rate.

The fourth chapter of the paper summarizes the results obtained through the analysis of the conclusions of the two previous chapters. By comparing the project objectives with the results of the experimental tests, it is possible to confirm the validity of lumped parameter models and fluid dynamics simulations for the design, balancing and verification of cooling systems for battery packs.

Index

1	BATTERY PACK COOLING SYSTEMS	1
1.1	Cells overview.....	1
1.2	Battery pack cooling systems overview.....	2
1.2.1	Medium to regulate battery temperature	3
2	BLIZZ PRIMATIST	7
2.1	Problem statement	7
2.2	BLIZZ PRIMATIST overview.....	8
2.2.1	Technical data.....	10
2.3	Battery pack	12
2.3.1	Overview	12
2.3.2	Cell configuration	13
2.3.3	Module components.....	14
2.3.4	Battery pack natural convection cooling test.....	15
2.4	Battery cooling design 1	17
2.4.1	Overview	17
2.4.2	Simscape model with lumped parameters	18
2.5	Battery cooling design 2	27
2.5.1	Overview	27
2.5.2	Simscape model with lumped parameters	29
2.6	Experimental test.....	30
2.6.1	Test results	31
2.7	Conclusions.....	33
3	P084 PROJECT	34
3.1	Problem statement	34
3.2	Fluid dynamics analysis of cooling components.....	35
3.2.1	Introduction	35
3.2.2	Geometry and parameters.....	35
3.2.3	Simulation setup	37
3.2.4	Mesh generation	39
3.2.5	Grid Independence Study.....	41
3.2.6	Steady state simulations results	44
3.2.7	Transient simulation results.....	53
3.2.8	Validation.....	54
3.3	Minimodules	55

3.3.1	Problem statement	55
3.3.2	Introduction	55
3.3.3	Validation of pressure drop along coolers.....	59
3.3.4	Flow distribution.....	64
3.3.5	Conclusions	66
3.3.6	Simplify battery pack thermal analysis	68
3.3.6.1	Computational Thermal Fluid Dynamics simulation.....	68
3.3.6.2	Simscape 1D thermal model.....	74
3.3.6.3	Validation of thermal simulations.....	75
3.4	Full battery pack.....	78
3.4.1	Overview	78
3.4.2	Inlet piping	80
3.4.3	Outlet piping.....	81
3.4.4	Full system hydraulic balance	82
3.4.4.1	Hardy Cross Method	84
3.4.4.2	Coolant volume flow rate at 70 lpm.....	86
3.4.4.3	Coolant volume flow rate at 50 lpm.....	93
3.4.5	Total pressure drop	96
4	CONCLUSIONS	98
4.1	BLIZZ PRIMATIST.....	98
4.2	PROJECT P084.....	98

List of figures

Figure 1: Air cooling system.....	3
Figure 2: Liquid cooling system.....	4
Figure 3: HVAC temperature management system.....	4
Figure 4: Refrigerant cooling system.....	5
Figure 5: Coolant & refrigerant cooling system.....	5
Figure 6: Liquid immersion cooling system.....	6
Figure 7: Bertone Z.E.R.....	8
Figure 8: BLIZZ PRIMATIST.....	9
Figure 9: Tubular frame.....	10
Figure 10: Battery Pack.....	10
Figure 11: Front suspension.....	11
Figure 12: Rear suspension.....	11
Figure 13: Transmission and cooling.....	11
Figure 14: Electric motor.....	11
Figure 15: Battery pack (top).....	12
Figure 16: Battery pack (side).....	13
Figure 17: Bus bars and wire bonding.....	14
Figure 18: Battery module (side view).....	14
Figure 19: Cooling system structure (first version).....	17
Figure 20: Lumped parameter thermal model of cooling system.....	18
Figure 21: Schematic of a tube bank in cross flow.....	20
Figure 22: Tube arrangements in a staggered bank.....	21
Figure 23: Flow conditions for staggered tubes.....	21
Figure 24: Boundary layer development and Nusselt number distribution on a heated horizontal cylinder.....	23
Figure 25: End view of flow at bottom surface of cold plate.....	
Figure 26: End view of flow at top surface of hot plate.....	25
Figure 27: Buoyancy-driven flows on horizontal cold ($T_s < T_\infty$) and hot ($T_s > T_\infty$) plates: (a) Top surface of cold plate. (b) Bottom surface of cold plate. (c) Top surface of hot plate. (d) Bottom surface of hot plate.....	26
Figure 28: Cooling system structure (ultimate version).....	27
Figure 29: Cooling system layout.....	28
Figure 30: Lumped parameter thermal model of cooling system (ultimate version).....	29
Figure 31: Short cooler CAD model.....	36

Figure 32: Long cooler CAD model.....	36
Figure 33: Short cooler mesh representation.....	39
Figure 34: Sectional view of short cooler mesh.....	39
Figure 35: Detail of volumetric controls on the holes.....	40
Figure 36: Detail of the cylindrical volumetric control.....	41
Figure 37: Short 1.9 mm cooler pressure contour.....	44
Figure 38: Short 1.9 mm cooler velocity contour (streamlines representation).....	45
Figure 39: Short 1.8 mm cooler pressure contour.....	46
Figure 40: Short 1.8 mm cooler velocity contour (streamlines representation).....	48
Figure 41: Long 2.0 mm cooler pressure contour.....	49
Figure 42: Long 2.0 mm cooler velocity contour (streamlines representation).....	50
Figure 43: Long 2.5 mm cooler pressure contour.....	51
Figure 44: Long 2.5 mm cooler velocity contour (streamlines representation).....	52
Figure 45: Cooler filling stages. Transient CFD simulation.....	53
Figure 46: Simplified battery pack CAD model.....	56
Figure 47: Equivalence between the simplified battery pack and the hydraulic model.....	59
Figure 48: Representation of the study domain mesh.....	70
Figure 49: Representation of the temperature contour of the study domain.....	71
Figure 50: Temperature contour of the cells.....	72
Figure 51: Temperature contour of the flow inside the cooler displayed by streamlines.....	72
Figure 52: Lumped parameter model of the battery pack cooling system.....	74
Figure 53: Position of the NTC sensors used for temperature measurement.....	75
Figure 54: Complete battery pack scheme.....	78
Figure 55: Scheme of a central module of the battery pack.....	79
Figure 56: Scheme of a side module of the battery pack.....	79
Figure 57: Scheme of the inlet ducts represented by hydraulic resistances.....	80
Figure 58: Scheme of the outlet ducts represented by hydraulic resistances.....	81
Figure 59: Representation of the complete battery pack through hydraulic resistances.....	82
Figure 60: Simplification of the lumped parameter hydraulic model through the calculation of equivalent hydraulic resistances.....	83
Figure 61: Schematic diagram of the complete cooling system of the battery pack inside the vehicle.....	97

List of tables

Table 1: Cells characteristics comparison.....	2
Table 2: Cooling systems comparison.....	6
Table 3: Z.E.R. technical data.....	8
Table 4: Category A group VIII-1 record goals.....	9
Table 5: Category A group VIII-2 record goals.....	9
Table 6: Thermal model data.....	19
Table 7: Vacuum pump technical characteristics.....	28
Table 8: Records achieved in Category VIII Class 1.....	33
Table 9: Records achieved in Category VIII Class 2.....	33
Table 10: Coolers geometric parameters.....	36
Table 11: Fluid properties.....	36
Table 12: Surface control levels.....	40
Table 13: Characteristics of the mesh used for the grid independence study.....	41
Table 14: Grid Independence Study results.....	43
Table 15: Coolant flow distribution in the short 1.9 mm cooler.....	46
Table 16: Coolant flow distribution in the short 1.8 mm cooler.....	48
Table 17: Coolant flow distribution in the long 2.0 mm cooler.....	50
Table 18: Coolant flow distribution in the long 2.5 mm cooler.....	52
Table 19: Comparison between simulated and experimental pressure drop values for the different types of Coolers.....	54
Table 20: Usage map to characterize the battery pack.....	57
Table 21: Comparison between real and simplified battery pack.....	57
Table 22: Cell characteristics.....	58
Table 23: Comparison between the hydraulic resistances of the coolers.....	60
Table 24: Comparison between the experimental and simulated pressure drops for the different configurations analysed.....	60
Table 25: pressure drop experimentally calculated along the long and short mini module as a function of the flow rate of the fluid.....	61
Table 26: Comparison between experimental and simulated pressure drop values.....	62
Table 27: Pressure drop values used for the subsequent design phases.....	63
Table 28: Short minimodule Grid Independence Study.....	64
Table 29: Comparison between the pressure drop values along the simplified battery pack obtained experimentally and through CFD simulation.....	66
Table 30: Physical properties of cells and coolers.....	68

List of tables

Table 31: Surface control refinement levels.....	70
Table 32: Physical parameters of the lumped parameter model.....	74
Table 33: Pressure drop and hydraulic resistance in each branch of the inlet ducts.....	80
Table 34: Pressure drop and hydraulic resistance in each branch of the outlet ducts.....	81
Table 35: Pressure drop and hydraulic resistance values for each type of cooler.....	82
Table 36: Values of equivalent hydraulic resistances.....	83
Table 37: Volume flow rate of coolant in each branch of the system.....	84
Table 38: Volumetric flow rate of the coolant inside the battery pack modules following hydraulic balancing.....	92
Table 39: Volumetric flow rate of the coolant inside the battery pack modules following hydraulic balancing.....	95

1 BATTERY PACK COOLING SYSTEMS

This introductory chapter describes the main types of cells and cooling systems for battery packs used in the automotive industry.

1.1 Cells overview

The three types of cells most used on the market are:

- Cylindrical Cells
- Prismatic Cells
- Pouch Cells

Cylindrical cells are the most used as they are inexpensive to produce, widespread, stable, safe and can be used in many industries. Cylindrical cells have a low watt-per-hour price and an higher cell voltage than other technologies (3.7 V).

The positive electrode can be made from different solutions:

- Lithium cobalt oxide (LiCoO₂)
- Lithium manganese oxide (LiMnO₄)
- Lithium iron phosphate (LiFePO₄)

The negative electrode is made of graphite (carbon).

The electrolyte is a liquid made up of lithium salts dissolved in ethylene carbonate.

Lithium-ion prismatic cells are thinner and lighter than cylindrical ones. These cells have a rectangular aluminium or steel case which increases their stability. The design of prismatic cells is not standardized, for this reason, they have a higher watt-per-hour price than cylindrical cells. The non-standard shape allows greater design flexibility and the possibility of stratifying the cells one on top of the other to reduce the volume occupied. Thermal management of prismatic cells is worse than cylindrical ones.

Pouch cells, compared to prismatic cells, do not have an aluminium or steel case but are closed in a soft polymer plastic film or shell. For this reason, they are very light.

Battery pack cooling systems overview

Lithium-polymer batteries (LiPo) use a polymer electrolyte versus a liquid one. Pouch cells are safer than prismatic cells due to the absence of a rigid case which, in case of a cell malfunction, can explode. Compared to Li-ion cells, pouch cells have a higher cost, a lower lifespan and lower stored power.

	Cylindrical	Prismatic	Pouch
Watt-per-hour price	Low	Medium	High
Resistance to deformation	High	High	Low
Ease of welding	High	Low	Low
Resistance to humidity and high temperatures	High	Medium	Low
Thermal management	High	Low	Medium
Stackability	No	High	Medium
Production cost	Low	Medium	High
Lifespan	High	Low	Medium

Table 1: Cells characteristics comparison

Table 1 shows the main characteristics of the three most used cell types.

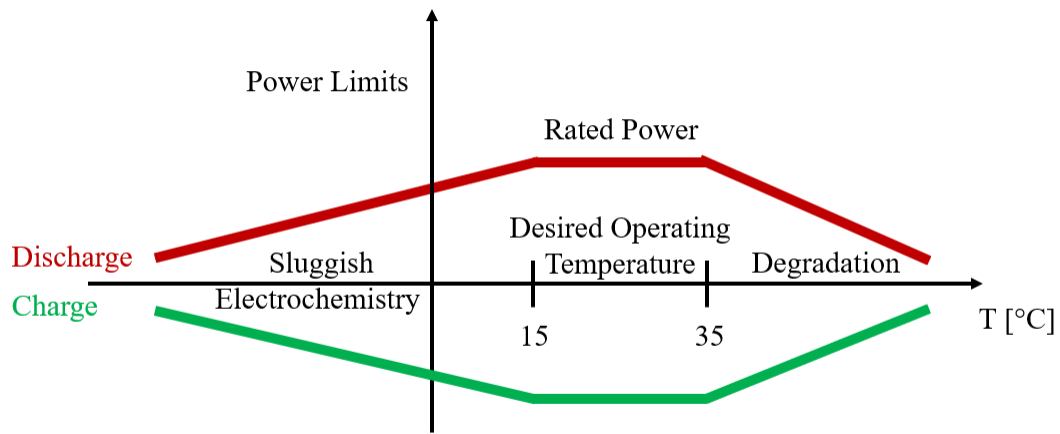
1.2 Battery pack cooling systems overview

Proper thermal management of the Battery Pack is extremely important for:

- Monitoring cells' health, identifying and reporting errors.
- Keeping cells' temperature during use in the optimal range.
- Keeping cells' temperature in the battery pack homogeneous.
- Suppressing any thermal runaway propagation.

The optimal operating temperature range for the battery pack depends on the characteristics of the cells used. Most manufacturers identify the operating temperature as $0\text{ }^{\circ}\text{C} \div 45\text{ }^{\circ}\text{C}$ during the charging phase and $-20\text{ }^{\circ}\text{C} \div 60\text{ }^{\circ}\text{C}$ during the discharge.

However, according to the study conducted by [1], the optimal temperature range for the use of lithium-ion cells is between $15\text{ }^{\circ}\text{C}$ and $35\text{ }^{\circ}\text{C}$. Graph 1 shows the trend of the electrical power supplied and absorbed by the battery pack as a function of the temperature of the cells.



Graph 1: Power trends as a function of the cells temperature

As can be seen from graph 1, if the temperature of the cells goes out of the optimal operating range, there is a progressive decrease in the power limit that the cell can deliver and absorb.

At low temperatures, the speed of chemical reactions, which take place inside the cell to produce energy, decreases. This is due to the contraction of the materials that form the electrodes with the consequent decrease in the motion of the ions in the intercalation spaces. For this reason, the electrodes do not accept the flow of current and the cell loses power and capacity.

Above 35 °C, the cell capacity and the amount of available power begin to decrease. If the cell temperature exceeds 50 °C, the life span of the cell begins to decrease. For temperatures above 70 °C, the threat of thermal runaway arises.

1.2.1 Medium to regulate battery temperature

To keep the temperature of the cells within the optimal operating range, it is necessary to equip the battery pack with cooling and heating systems.

The main mediums used to regulate the temperature of the cells are as follows:

By air

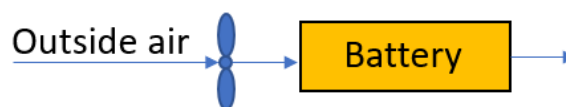


Figure 1: Air cooling system

Battery pack cooling systems overview

This configuration only allows cooling of the battery pack. The system uses the surrounding air to keep the temperature of the cells within the optimal operating range. To increase or decrease the cooling it is possible to modify the rotation speed of one or more fans. This type of cooling cannot be used if the external environment temperature is high. The simplicity of the system makes it excellent for applications where weight and limited space availability are primary factors.

By coolant & air

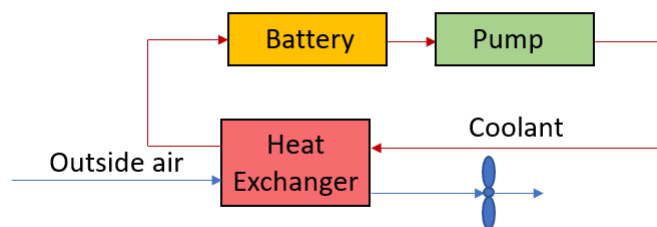


Figure 2: Liquid cooling system

In this case, the cooling system uses a pump to force the passage of the coolant inside the liquid-air heat exchanger. This type of cooling system is more effective than using air alone. The presence of the coolant leads to an increase in weight and complexity of the system.

By air & other medium

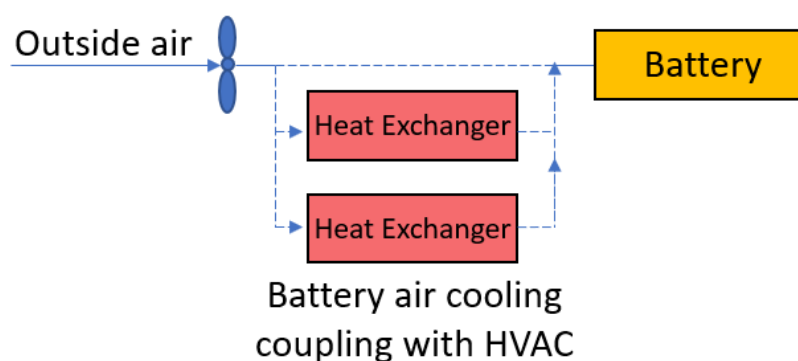


Figure 3: HVAC temperature management system

The temperature regulation system in figure 3 uses an HVAC (Heating, Ventilation, and Air Conditioning) system for thermal management of the battery pack. This system overcomes the criticalities of the two previous layouts at the expense of the

increased complexity of the circuit. In this configuration, in addition to cooling, it is possible to heat the cells of the battery pack.

By refrigerant

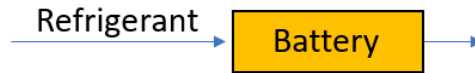


Figure 4: Refrigerant cooling system

The cooling system in figure 4 is similar to the system in figure 1. The main difference is the use of two different cooling mediums. This system does not use air to cool the cells but a refrigerant (R134a, R1234yf). The use of the refrigerant offers a cooling rate 3 times higher than liquid glycol and allows the thermal management of the battery pack to be released from the outside air temperature.

Using a refrigerant as a cooling system offers a faster thermal response than conventional systems. This configuration offers greater control over the safety of the battery pack by allowing the use of sprays to block any thermal runaway propagation.

By coolant & refrigerant

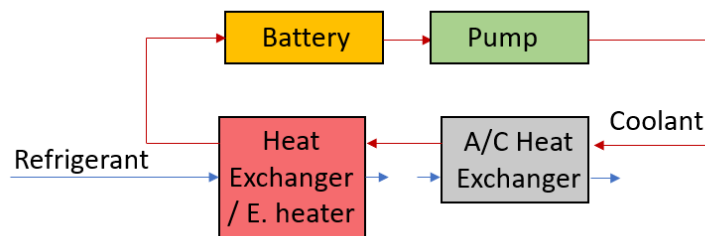


Figure 5: Coolant & refrigerant cooling system

The thermal management system of the battery pack shown in Figure 5 uses a refrigerant instead of air as the input of the heat exchangers. This system allows to cool and heat the cells of the battery pack regardless of the outside air temperature. The negative side of this configuration is given by the complexity of the system and the increase in weight due to the presence of the liquid coolant.

Liquid immersion

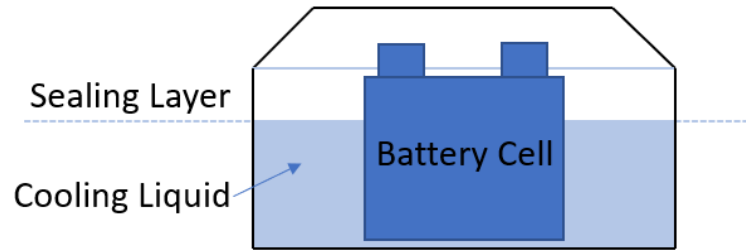


Figure 6: Liquid immersion cooling system

The cooling system in figure 6 uses a liquid to cool the cells immersed inside it. This type of cooling allows an homogeneous distribution of temperature inside the battery pack. The disadvantage of this configuration is the excessive weight of the system. Table 2 summarizes and compares the characteristics of the three main cooling systems for battery packs.

	Air Cooling	Liquid Cooling	Refrigerant Cooling
Cooling/Heating performance	Low	high	Very high
System complexity	Low	High	Medium
Cost	Low	High	Potential Low
Weight	Low	High	Medium
Safety	Sealed + Waterproof	Possible Leakage	Safety advantage
Temperature uniformity	Low	High	High
Control	Low	High	High

Table 2: Cooling systems comparison

2 BLIZZ PRIMATIST

2.1 Problem statement

The first case study discussed concerns the BLIZZ PRIMATIST vehicle. The vehicle was designed entirely by Podium Advanced Technologies commissioned by the eclectic Gianmaria Aghem. Aghem, as an eternal lover of Bertone's Z.E.R. car, wants to create a vehicle capable of breaking down the records held by the Z.E.R. and overcoming new ones.

To break the records Gianmaria plans to go to the Nardò Technical Center where, in two consecutive days of testing, he will try to beat the previous Z.E.R. records.

The BLIZZ PRIMATIST vehicle is equipped with an electric motor powered by a 700 V and 185 kg battery pack positioned in the centre of the car. Due to the large number of cells and their high packing coefficient, the battery pack has a particularly high thermal inertia.

For this reason, after having warmed up following intense use of the vehicle, the battery pack takes many hours to return to the optimal operating temperature.

The strong gradient and the high temperature value of the cells at the end of the first day of testing, combined with the heat generated during overnight charging, prevent the vehicle from performing adequately during the second day of testing.

For this reason, it is necessary to develop a cooling system for the battery pack to be used during the charging phase between the first and second day of testing.

The paper describes the design and development process of the cooling system.

Project target

- Maximum cell temperature after 15 hours of charging $< 30\text{ }^{\circ}\text{C}$

2.2 BLIZZ PRIMATIST overview

Starting point (Bertone Z.E.R.)

The starting point for the construction of the BLIZZ PRIMATIST vehicle was the Bertone Z.E.R. built in 1994.



Figure 7: Bertone Z.E.R.

From the Z.E.R., Podium designers took inspiration for the creation of BLIZZ PRIMATIST, keeping the track value unchanged and increasing the wheelbase by 70 mm. As for the power supply, both cars are electric; the Z.E.R. is powered by lead acid battery while the BLIZZ battery is made of Li-ion cells.

Thanks to the different technologies used and technological advances, the weight of BLIZZ PRIMATIST is 400 kg lower than the Z.E.R.'s weight.

Table 1 shows the main technical data of the Z.E.R.

Wheelbase [mm]	2200
Track [mm]	700
Weight without driver [kg]	890
Battery pack weight [kg]	600
Battery technology	Lead acid

Table 3: Z.E.R. technical data

Goal of the project

The goal of the project is to overcome two different types of records:

- Land speed records
- Duration records



Figure 8: BLIZZ PRIMATIST

The categories of the FIA in which the vehicle competes are:

Category A group VIII-1 (electric vehicles, electrically propelled) – class 1 (0 to 500 kg).

Test	Actual Record	Objective
100 km Starting from a standstill	99.092 km/h	245.00 km/h
100 mi Starting from a standstill	76.504 km/h	215.00 km/h
1 h Starting from a standstill	113.644 km/h	200.00 km/h
1 km moving start	171.791 km/h	320.00 km/h
1 mi moving start	158.849 km/h	320.00 km/h

Table 4: Category A group VIII-1 record goals

The performance objectives to be achieved in the two categories are the same as the weight of the vehicle between class 1 and 2 varies by only 3 kg. The weight variation is obtained by adding ballast.

Category A group VIII-2 from 500 to 1000 kg.

Test	Actual Record	Objective
100 km starting from a standstill	197.586 km/h	245.00 km/h
100 mi starting from a standstill	-----	215.00 km/h
1 h starting from a standstill	199.881 km/h	200.00 km/h
1 km moving start	333.271 km/h	320.00 km/h
1 mi moving start	330.139 km/h	320.00 km/h

Table 5: Category A group VIII-2 record goals

2.2.1 Technical data

Vehicle data

Wheelbase: 2270 mm

Track: 700 mm

Weight: 490 kg without driver

Battery Pack weight: < 200 kg

Battery technology: Li-ion

Aerodynamics data

Frontal area: 0.607 m²

Cd: 0.13

Cl: -0.3

Chassis properties

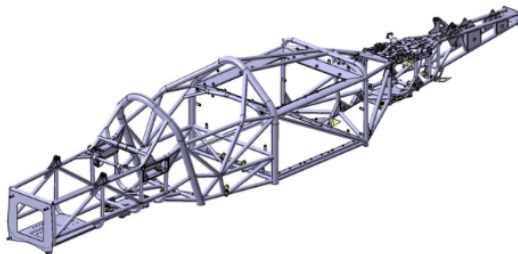


Figure 9: Tubular frame

Tubular Frame

Material: 25CrMo4 (E4130)

Weight: 77 kg

Battery pack

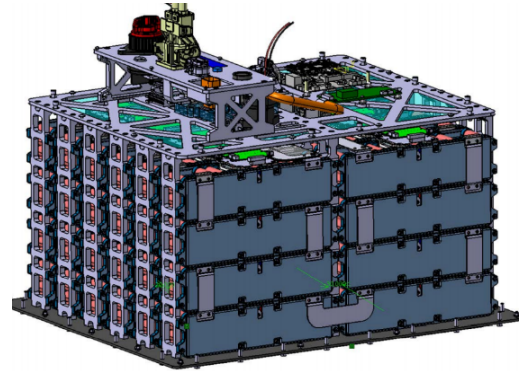


Figure 10: Battery Pack

Cells number: 2688 (Samsung 18650)

Pack structure: 192s-14p

Nominal Voltage: 700V

Max Voltage: 800 V

Capacity: 34 kWh

Max discharge current: 230 A

Max discharge current: 66 A

Cells weight: 131 kg

Final weight: 185 kg

Front suspension



Figure 11: Front suspension

Double A arm architecture.
Push rod system.
Bump travel: +20-35 mm
Weight: 50 kg
Steer Angle: $\pm 7.5^\circ$
Turning circle diameter: 35m kerb to kerb
Breaking system: AP Racing
Shock Absorber: Bilstein MDS 860

Rear suspension



Figure 12: Rear suspension

Double A arm architecture
Push rod system
Bump travel: +25 -35 mm
Weight: 50 kg
Steer Travel: ± 15 mm
Breaking system: AP Racing

Transmission and cooling



Figure 13: Transmission and cooling

Differential: QUIFE QDF7ZR
Transmission Ratio: 18/29
Chain transmission.
Custom half shafts.
Water Pump: EWP 80

Phi Power PHI 271 motor

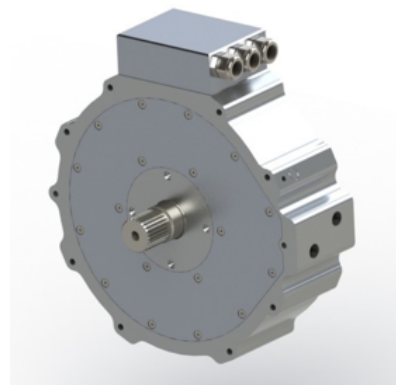


Figure 14: Electric motor

Lightweight design.
Tunability.
High nominal continuative power.
Voltage: 760V
Max Power: 120 kW
Max Torque: 216 Nm
Max rpm: 8000
Max Current: 350A

Battery pack

2.3 Battery pack

2.3.1 Overview

The battery pack of the BLIZZ PRIMATIST vehicle consists of 6 vertical stacks each formed by 8 modules fixed on aluminium supports. The aluminium supports are bolted to the carbon fiber base of the battery pack and to the upper aluminium plate.

The function of the upper plate is separating the modules' environment from the derivation box, which contains high speed fuses contactors, main DC lines, BMS master, IMD (insulation monitoring device), all the connectors (HV and LV) and venting valve.

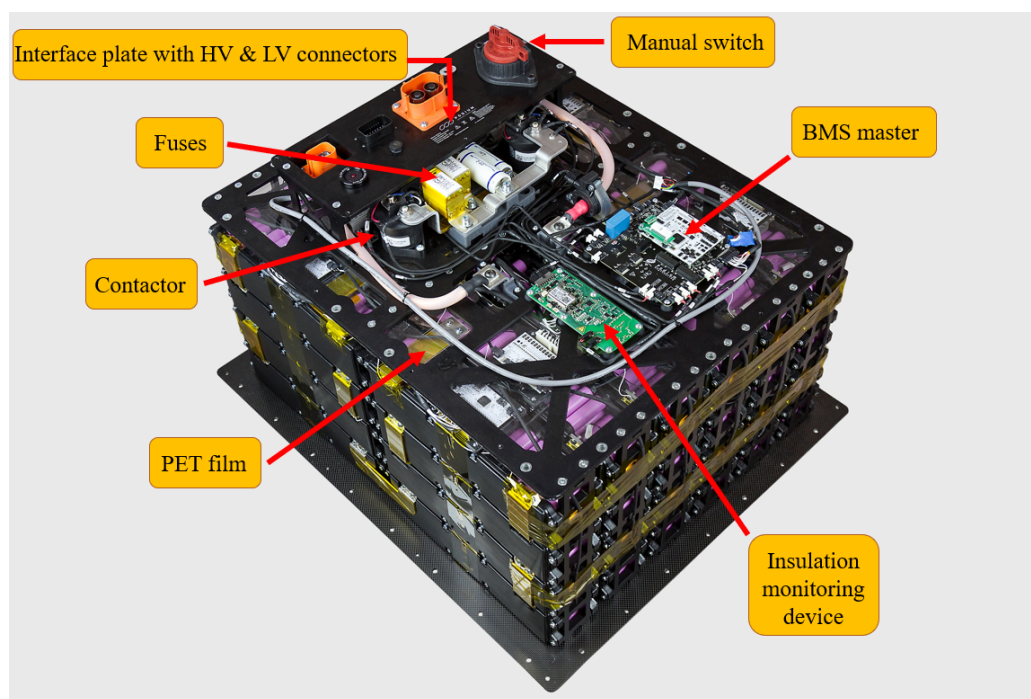


Figure 15: Battery pack (top)

The 48 modules are connected in series and have a nominal voltage of 14.6V each. Each module consists of 56 cylindrical cells "Samsung 18650 INR18650-35E" with a nominal voltage of 3.65 V. The cells within a module are organized in 4 series made of 14 parallels each.

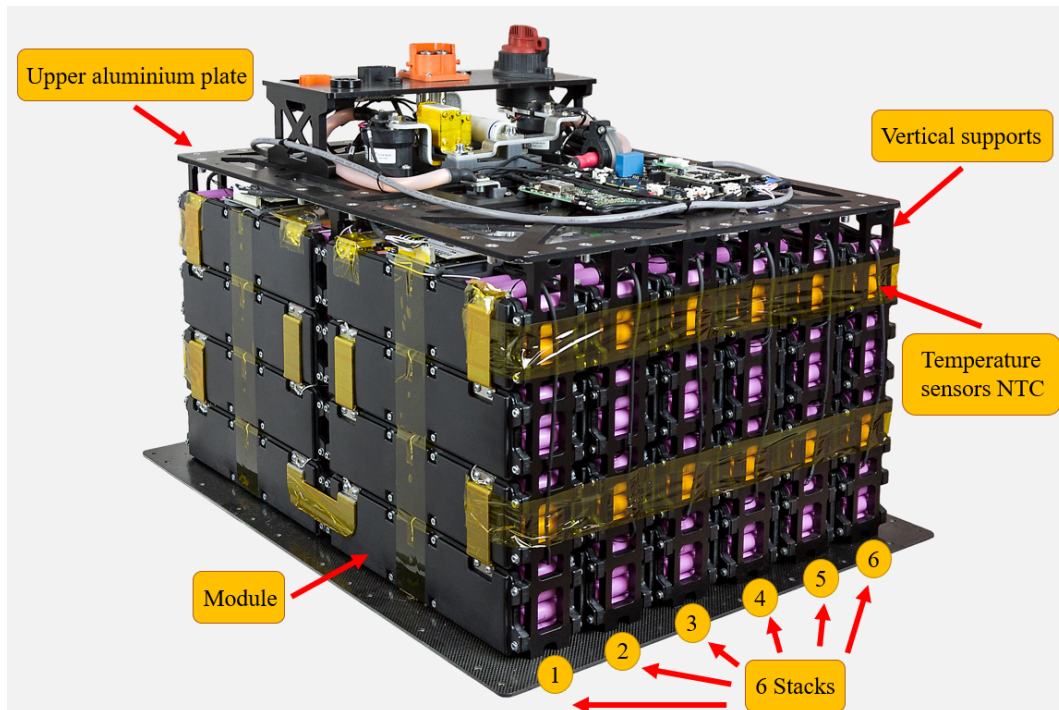


Figure 16: Battery pack (side)

Inside each module, the cells are plugged and glued on both sides into plastic supports. The electrical connection between the cell's terminal and the bus bars is accomplished by aluminium wires, welded using the wire bonder machine in Podium Advanced Technologies. Both cell terminals and bus bars are protected by means of special closure plates, which close the module.

2.3.2 Cell configuration

The best configuration for cells packaging was to group cells in modules of 56 cells. This configuration has advantages in terms of:

- Mechanical point of view
- Electrical point of view

This configuration allows the best possible use of the space with a kWh/l ratio equal to 0.22 also including the volume for the junction box, the BMS devices and battery pack enclosure.

The chosen layout facilitates assembling operations, and the dimensions of the modules was judged to be the best compromise between volume packaging and manufacturing.

2.3.3 Module components

The main components that form the modules of the battery pack are the following:

- **Cell holder:** to keep cells mechanically secured to the structure. Cells are inserted on the inner side and pushed until they reach the bottom wall. The distance from cell to cell is equal to 1.2 mm.
- **Bus bars:** used to connect cell parallels and series, screwed to cell holder.

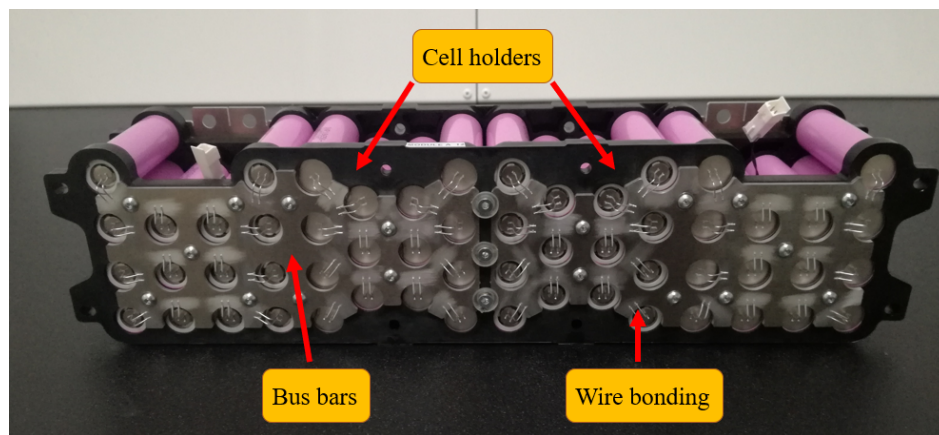


Figure 17: Bus bars and wire bonding

- **Module covers:** used to enclose cells in each module, they protect cell terminals from electrical shorts and provide mechanical strength.

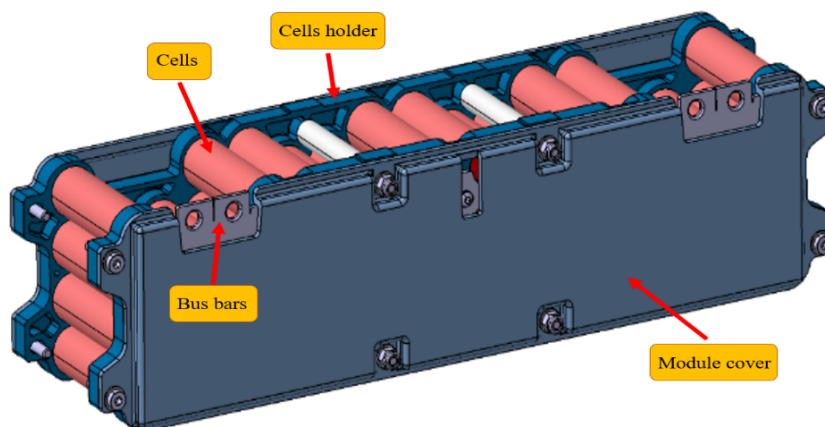


Figure 18: Battery module (side view)

2.3.4 Battery pack natural convection cooling test

For the correct design of the cooling system, it is necessary to experimentally evaluate the effect of natural convection on the thermal behaviour of the battery. This section analyses the test conducted to evaluate the effect of natural convection on the cooling of the battery pack in configuration with and without box cover.

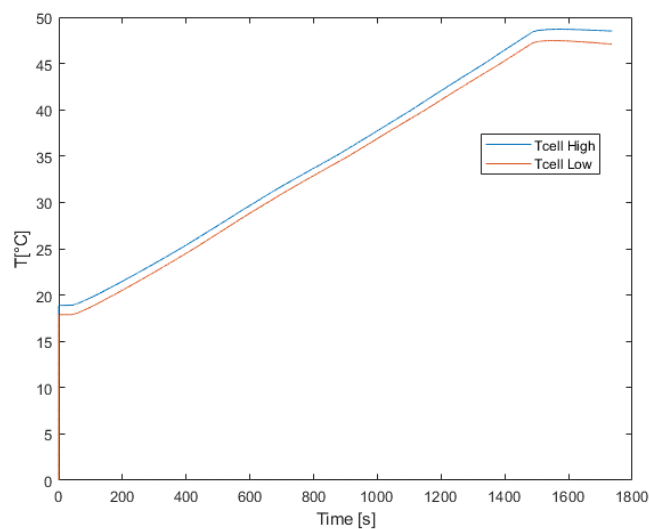
The test conducted is the one for 100 km at equivalent speed of 245 km/h, in two different conditions.

Test objectives

- Evaluating the effect of natural convection on the temperature behaviour of the pack during the test.
- Checking overall status of pack and mechanical/electrical failure.
- Final performance check.

Test results

The test initial temperature was 17.3 °C evaluated as the averaged between highest and lowest readings. As shown in graph 2 during the discharge phase the temperature of the cells presents a linear trend. After 1500 s the maximum cell temperature reaches 48 °C while the minimum one reaches 45.5 °C.



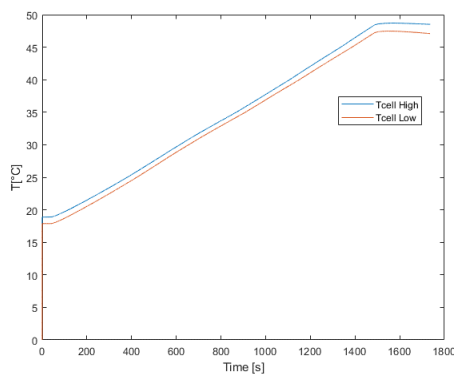
Graph 2: Maximum and minimum cell temperature

Battery pack

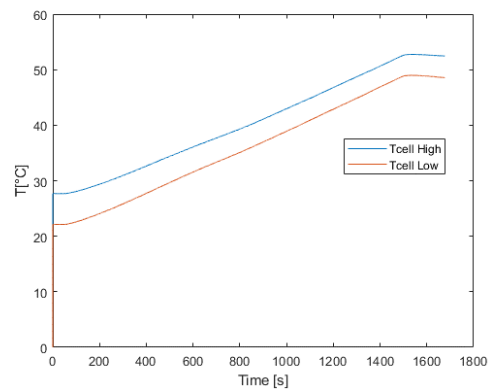
Graphs 3 and 4 represent the maximum and minimum temperature of the battery pack cells in the configuration with and without box cover. It is important to note that the two graphs have different scales along the ordinate axis.

Unfortunately, it was not possible to make a straight correlation between “box” and “no-box” configuration, as the conditioning system for the test room is linked to the conditioning system of all Podium facilities, and therefore initial temperatures were pretty much different.

As temperature increase showed almost linear behaviour, it was possible to make some predictions on what the effect of natural convection around the battery pack might be.



Graph 3: Maximum and minimum cell temperature (with box)



Graph 4: Maximum and minimum cell temperature (without box)

Conclusions

The analysis of graphs 3 and 4 shows how both configurations (with box and without box) lead to the achievement of the maximum cell temperature of about 50 °C. Although the maximum temperature reached is the same, the maximum test start temperature is 10 °C higher in the “without box” configuration. This means that the heat transferred in the “no box” test is lower than the test with the box cover. Despite this, the maximum temperature reached at the end is identical for the two configurations. For this reason, it is evident that natural convection in the configuration without the box cover is more effective in cooling.

Since the box cover cannot be removed in conditions of use, it is necessary to develop a cooling system that allows a change of air inside the battery pack.

2.4 Battery cooling design 1

This section analyses the first hypothesis relating to the design of the cooling system of the battery pack, detailing the physics underlying the creation of the lumped parameter model used to predict the temperature trend.

2.4.1 Overview

Not having the time and the necessary equipment during the record attempt to disassemble the battery pack case and to cool the cells, it was necessary to identify a cooling mode that did not involve the disassembly of the external casing.

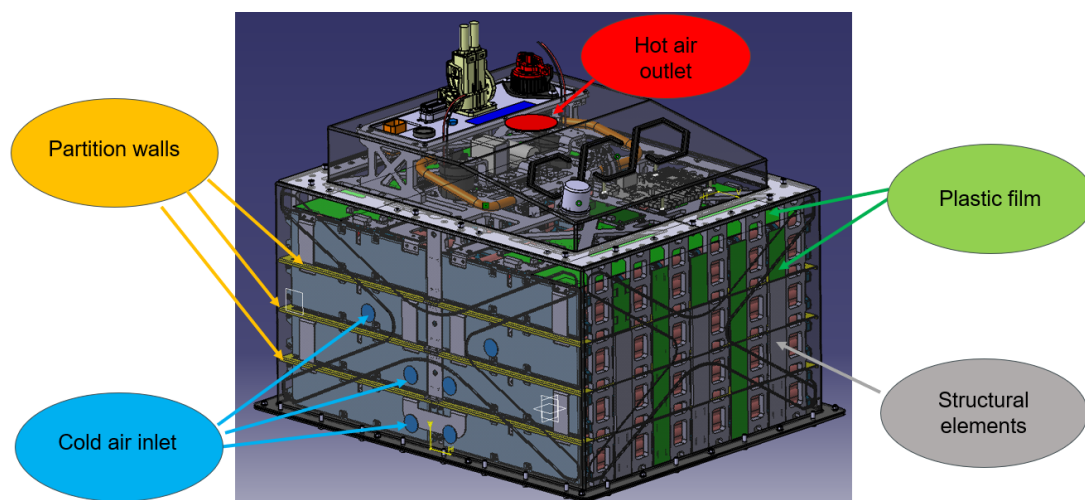


Figure 19: Cooling system structure (first version)

The initial solution involves the use of a system of ducts made through partition walls to constrain the passage of air in a homogeneous way through all the cells that form the battery pack.

As shown in the figure 19, the cold air enters the pack through six holes on the side face, two for each level, to ensure the maximum possible homogeneity of the flow inside.

The partition walls are supported through structural elements and the passage of air inside the cells is also ensured by the presence of a plastic film used as a sealant.

Finally, the hot air comes out through a hole on the top of the package.

2.4.2 Simscape model with lumped parameters

To verify the effectiveness of the proposed solution, a Simscape model was created to represent the phenomenon.

To correctly model the physics of the problem it is necessary to introduce the following numbers to formulate the correlations used in the model.

Grashof number: Measure of the ratio of buoyancy forces to viscous forces.

$$Gr_L = \frac{g\beta(T_s - T_\infty)L^3}{\nu^2} \quad (2.1)$$

Nusselt number: Ratio of convection to pure conduction heat transfer.

$$Nu_L = \frac{hL}{K_f} \quad (2.2)$$

Peclet number: Ratio of advection to conduction heat transfer rates.

$$Pe_L = Re_L Pr \quad (2.3)$$

Prandtl number: Ratio of the momentum and thermal diffusivities.

$$Pr = \frac{\nu}{\alpha} \quad (2.4)$$

Reynolds number: Ratio of the inertia and viscous forces.

$$Re_L = \frac{VL}{\nu} \quad (2.5)$$

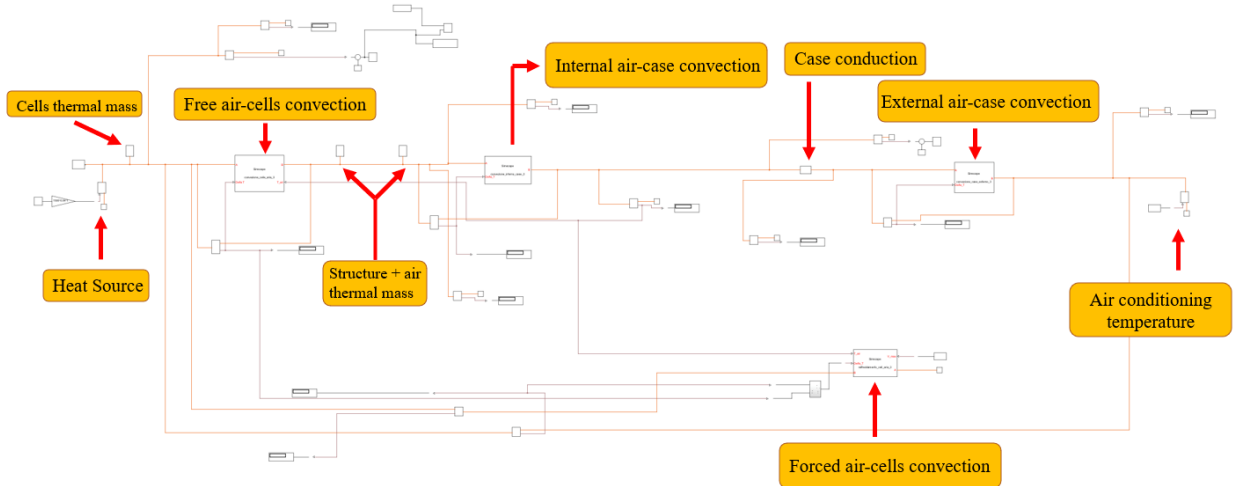


Figure 20: Lumped parameter thermal model of cooling system

Figure 20 shows the layout of Simscape thermal model. The figure shows the names of the main functional blocks that form the model. The lumped parameter model

considers the thermal masses of the cells, the air, and the metal and plastic components inside the battery pack. The convection heat exchanges considered are those between the cells and the air, considering both natural and forced convection, between the internal air and the case and between the case and the external air. The model also considers conduction in the case.

Table 6 shows the data used within the model.

Cell mass	0.048	kg
Cells dissipated power	600	W
Cell specific heat	960	J/kg/K
Air mass	0.1130	kg
Air specific heat	1006	J/kg/K
Case + metal mass	45	kg
Case + metal specific heat	1000	J/kg/K
Case surface	1.5	m ²
Case thickness	0.002	m
Case thermal conductivity	12	W/(m*K)
Cell diameter	0.01842	m

Table 6: Thermal model data

The physics used to build the functional blocks of the thermal model are analysed below.

Forced cell-air convection

The lumped parameter model considers the battery cells as a single heat source having a thermal power generated during recharging equal to the total thermal power generated by the 2688 cells that make up the car's battery pack. Being a lumped parameter model, it is not possible to calculate the temperature gradient inside the battery pack. To design, it is sufficient to evaluate the maximum temperature that is obtained inside the package.

Since the battery pack is air-cooled, the heat transfer between the cells and the cooling medium occurs by convection.

The total heat transfer rate q is obtained through the formula 2.6:

$$q = \bar{h}A_s(T_s - T_\infty) \quad (2.6)$$

Battery cooling design 1

\bar{h} is the average convection coefficient for the considered surface.

T_s is the surface temperature.

T_∞ is the fluid temperature.

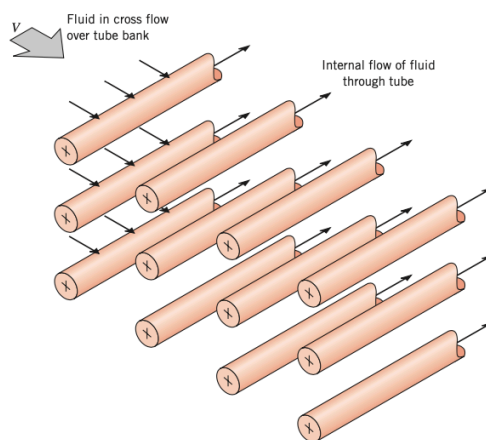
The model is concerned with simulating the heat transfer between the surface of the cells and the external flow. In this type of flows, boundary layers develop freely without constraints due to the presence of nearby surfaces. The discussion focuses on low speed forced convection without phase changes, neglecting effects on the nano and micro scale within the fluid.

In our case we are in a forced convection regime, in which the relative motion between the air and the cells is generated by a vacuum pump.

The average convection coefficient is a function of the Reynolds number and the Prandtl number as shown by equation 2.7.

$$\overline{Nu} = f(Re, Pr) \quad (2.7)$$

For the calculation of the heat exchange coefficient by convection between the cells and the air, the experimental correlations obtained through the study of a flow across banks of tubes are used (fig.21).



[6]

Figure 21: Schematic of a tube bank in cross flow

The arrangement of the cells inside the battery is in a staggered configuration. The correlations are determined according to 3 fundamental parameters: the diameter of the cells D , the transverse pitch S_T and the longitudinal pitch S_L (fig. 22).

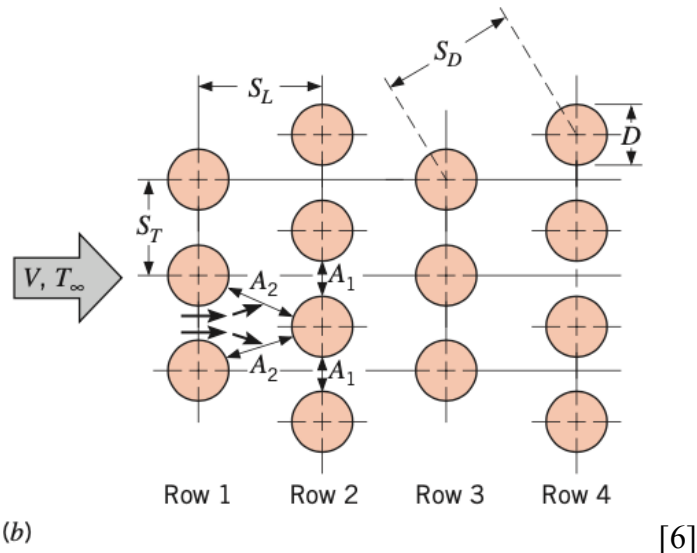


Figure 22: Tube arrangements in a staggered bank

The behaviour of air flow between the cells is dominated by the boundary layer separation effects and by wake interactions that influence the heat exchanged. The heat transfer between the air and the first row of cells is like that which occurs between the air and a single cell. As for the subsequent rows, the phenomenon is strongly influenced by the arrangement of the cells.

Experimentally, it is verified that the convection coefficient of a row increases with the increase in the number of rows up to row number 5. From this point on, the flow does not change, and the coefficient remains constant.

The staggered configuration (fig. 23) is characterized by a more tortuous air path than the in-line configuration which causes an increase in the heat transfer capacity.

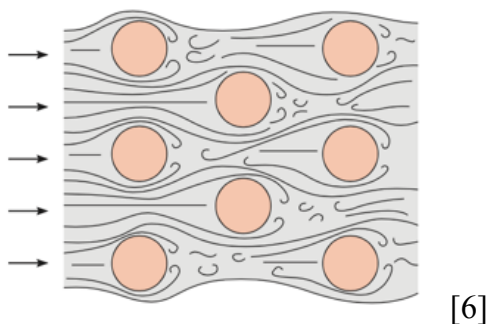


Figure 23: Flow conditions for staggered tubes

To determine the average heat transfer coefficient for the entire bank of cells, the correlation of Zukauskas (2.8) is used.

Battery cooling design 1

$$\overline{Nu}_D = C_1 Re_{D,max}^m Pr^{0.36} \left(\frac{Pr}{Pr_s} \right)^{\frac{1}{4}} \quad (2.8)$$

This correlation holds true for $N_L \geq 20$, $0.7 \leq Pr \leq 500$, $10 \leq Re_{D,max} \leq 2 \times 10^6$.

N_L is the number of rows of cells. All properties except Pr are evaluated at the temperature given by the arithmetic mean between the inlet air temperature T_i and the outlet air temperature T_o .

C_1 and m are constant values equal to:

$$C_1 = 0.35 \left(\frac{S_L}{S_L} \right)^{\frac{1}{5}}$$

$$m = 0.6$$

Since the N_L of the analysed configuration is less than 20, it is possible to apply the following correlation:

$$\overline{Nu}_D|_{(N_L \leq 20)} = C_2 \overline{Nu}_D|_{(N_L \geq 20)} \quad (2.9)$$

Where $C_2 = 0.99$.

The calculation of $Re_{D,max}$ is a function of the maximum velocity of the fluid between the cells.

For the aligned configuration, the maximum speed is reached in section A_1 (fig. 22) and is equal to

$$V_{max} = \frac{S_T}{S_T - D} V$$

Where V is the flow velocity upstream of the cells.

For the staggered configuration, the maximum speed can develop both in section A_1 and in section A_2 (fig. 22). The maximum speed is reached in section A_2 if the rows are spaced in such a way as to satisfy the following relationship.

$$2(S_D - D) < (S_T - D) \quad (2.10)$$

In this case, the maximum velocity is equal to:

$$V_{max} = \frac{S_T}{2(S_D - D)} V \quad (2.11)$$

In the case under consideration, the inequality 2.10 is not satisfied. For this reason the maximum speed will develop in section A_1 .

Since the air temperature changes considerably as it passes through the cells, the calculation of the $\Delta T = T_s - T_\infty$ leads to an overprediction of the heat transfer.

For this reason, we use the log-mean temperature difference:

$$\Delta T_{lm} = \frac{(T_s - T_i) - (T_s - T_o)}{\ln \left(\frac{T_s - T_i}{T_s - T_o} \right)} \quad (2.12)$$

The air temperature at the outlet is determined through (eq. 2.13).

$$\frac{T_s - T_o}{T_s - T_i} = \exp \left(- \frac{\pi D N \bar{h}}{\rho V N_T S_T c_p} \right) \quad (2.13)$$

Where N is the total number of cells in the battery and N_T is the number of cells in each row. After determining ΔT_{lm} , it is possible to evaluate the heat transfer rate per unit length of the cell through the equation 2.14:

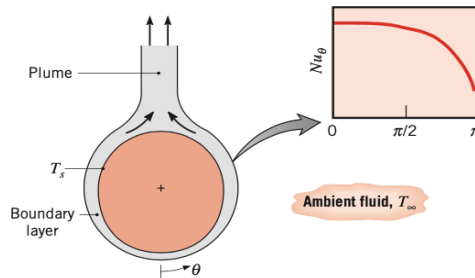
$$q' = N(\bar{h}\pi D \Delta T_{lm}) \quad (2.14)$$

Free air cell convection

In free convection, the motion of the air is determined by the buoyancy forces within the fluid. Buoyancy is determined by the double action of the fluid density gradient and by the body force (proportional to the density). In this case, the body force is gravitational. To determine the free convection between the cells and the air inside the case, the correlation formulated by Churchill and Chu is considered valid for $Ra_D \lesssim 10^{12}$.

$$\overline{Nu}_D = \left\{ 0.60 + \frac{0.387 Ra_D^{\frac{1}{6}}}{[1 + (0.559/Pr)^{9/16}]^{8/27}} \right\}^2 \quad (2.15)$$

The correlation provides an average Nusselt number over the entire circumference of the cylinder.



[6]

Figure 24: Boundary layer development and Nusselt number distribution on a heated horizontal cylinder

Battery cooling design 1

As shown in figure 24 for a heated cylinder, local Nusselt numbers are influenced by boundary layer development, which begins at $\theta = 0$ and concludes at $\theta < \pi$ with formation of a plume ascending from the cylinder. If the flow remains laminar along the surface of the cell, the distribution of the Nusselt number is maximum at $\theta = 0$ with a decreasing monotone behaviour. If the cylinder is cooled relative to the ambient fluid, boundary layer development begins at $\theta = \pi$, the local Nusselt number is maximum at this location, and the plume descends from the cylinder.

Air-case convection

At this juncture, the discussion focuses on the analysis of free convection in which the density gradient is due to a temperature gradient and the body force is gravitational.

The empirical correlations developed for geometries subject to external flows are of the form:

$$\overline{Nu}_L = \frac{\bar{h}L}{k} = C Ra_L^n \quad (2.16)$$

Where Ra_L is the Rayleigh number and is a function of the characteristic length of the geometry. The values of the exponent n are $1/4$ in the case of laminar flow and $1/3$ in the case of turbulent flow.

$$Ra_L = Gr_L Pr = \frac{g\beta(T_s - T_\infty)L^3}{\nu\alpha} \quad (2.17)$$

Vertical Plates

To determine the heat transfer between the air inside the battery pack and the vertical walls of the case, the following equations were used:

$$\overline{Nu}_L = \left\{ 0.825 + \frac{0.387 Ra_L^{\frac{1}{6}}}{[1 + (0.492/Pr)^{9/16}]^{8/27}} \right\}^2 \quad (2.18)$$

The equation 2.18 was identified by Churchill and Chu and is applicable in the entire interval of Ra_L . To obtain better accuracy in the case of laminar flow $Ra_L \lesssim 109$, the equation 2.19 was used.

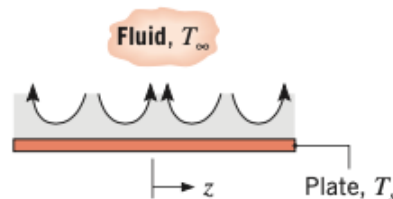
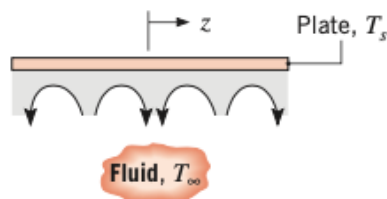
$$\overline{Nu}_L = 0.68 + \frac{0.670 Ra_L^{\frac{1}{4}}}{[1 + (0.492/Pr)^{9/16}]^{4/9}} \quad (2.19)$$

It is interesting to note that for high values of the Rayleigh number, the second term on the right side of the equations 2.19 becomes dominant bringing the two correlations to be identical to the equation 2.16 except for the constant C replaced by a function of Pr .

If the Rayleigh number is small, the first term of the right side of the equation is dominant. In this case it is necessary to consider the conduction parallel to the plate. The correlations used refer to a condition in which the surfaces considered are isothermal plate (constant T_s). In this case, therefore, $(T_s - T_\infty)$ does not vary with the longitudinal coordinate.

Horizontal Plates

As for the study of the heat exchange between the air and the horizontal walls of the case, in this condition the plate is aligned with the gravitational vector and the buoyancy force acts exclusively to induce the motion of the fluid in the vertical direction.



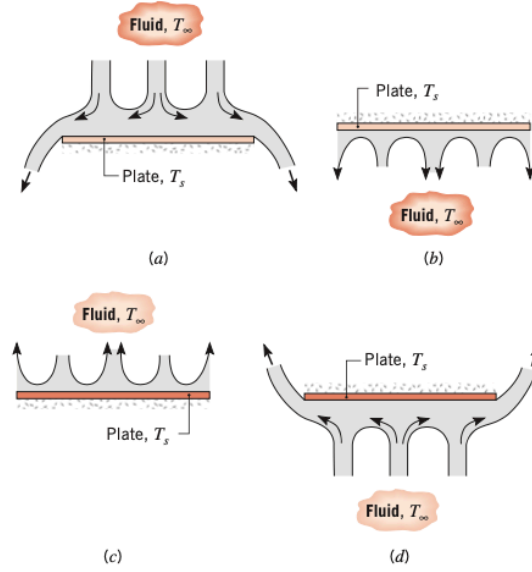
[6]

Figure 25: End view of flow at bottom surface of cold plate Figure 26: End view of flow at top surface of hot plate

Figure 25 represents a flow at bottom surface of cold plate ($T_s < T_\infty$) while figure 26 represents a flow at top surface of hot plate ($T_s > T_\infty$).

In the case in question, since the battery case is a parallelepiped, the lower and upper faces are horizontal planes. In this case the buoyancy force is exclusively normal to the surface. The flow pattern and heat transfer depend on the difference between surface and air temperature and on the position (upward or downward).

Battery cooling design 1



[6]

Figure 27: Buoyancy-driven flows on horizontal cold ($T_s < T_\infty$) and hot ($T_s > T_\infty$) plates: (a) Top surface of cold plate. (b) Bottom surface of cold plate. (c) Top surface of hot plate. (d) Bottom surface of hot plate

In the case of a cold surface facing upward and an hot surface facing downward, the tendency of the fluid to rise and fall is prevented by the presence of the plane which forces the flow to make a horizontal motion. This behaviour makes convection heat transfer ineffective.

Contrariwise, for a cold surface facing downward and an hot surface facing upward, the flow is driven by descending and ascending parcels of fluid respectively. In this case, the cold fluid that descends from the surface is replaced by the fluid that rises warmer from the environment and vice versa. In this configuration the heat transfer is more effective.

The correlations that were used to model the heat exchange inside the battery pack are as follows:

Upper surface of Hot plate or Lower surface of cold Plate

$$\overline{Nu}_L = 0.54 Ra_L^{\frac{1}{4}} (10^4 \lesssim Ra_L \lesssim 10^7, Pr \gtrsim 0.7) \quad (2.20)$$

$$\overline{Nu}_L = 0.15 Ra_L^{\frac{1}{3}} (10^7 \lesssim Ra_L \lesssim 10^{11}, \text{all } Pr) \quad (2.21)$$

Lower surface of Hot Plate or Upper Surface of Cold Plate

$$\overline{Nu}_L = 0.52 Ra_L^{\frac{1}{5}} (10^4 \lesssim Ra_L \lesssim 10^9, Pr \gtrsim 0.7) \quad (2.22)$$

2.5 Battery cooling design 2

Unfortunately, due to the lack of time for the construction of the ducts, the patron of BLIZZ PRIMATIST decided to modify the structure of the cooling system by providing specific indications for its realization.

2.5.1 Overview

The new layout, figure 28, includes only 4 holes on the battery pack case, two for the cold air inlet and 2 for the hot air outlet. The inlet holes are arranged on the lower part of the right side of the battery pack case while the outlet holes are located on the upper part of the left side. Inside the holes there are 4 screwed flanges used as supports for hose nozzles.

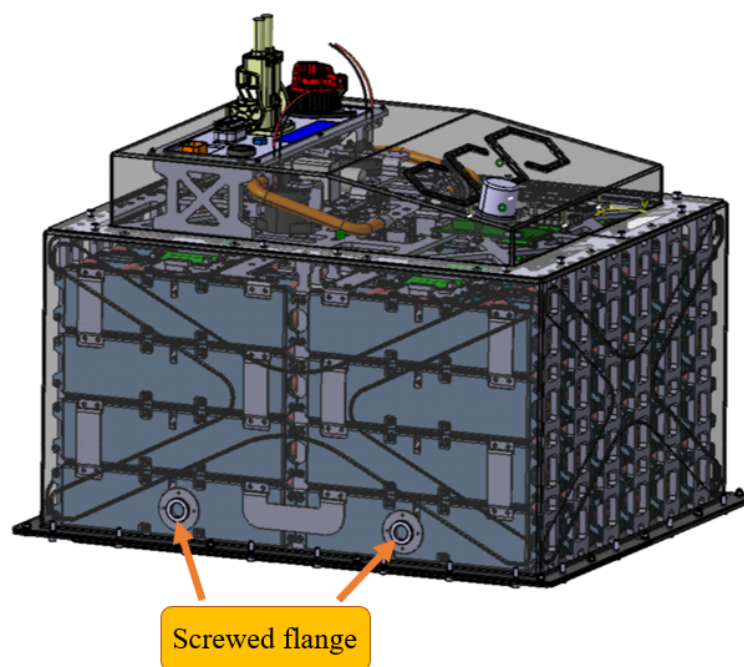


Figure 28: Cooling system structure (ultimate version)

The cooling system involves the use of a vacuum pump and a portable air conditioner both supplied by the customer. The vacuum pump is connected via two pipes to the hose connectors of the outlet holes. The vacuum created by the pump sucks cold air from the compartment containing the battery, cooled by an air conditioner, inside the box through the two inlet holes.

Figure 29 represents the layout of the cooling system.

Battery cooling design 2

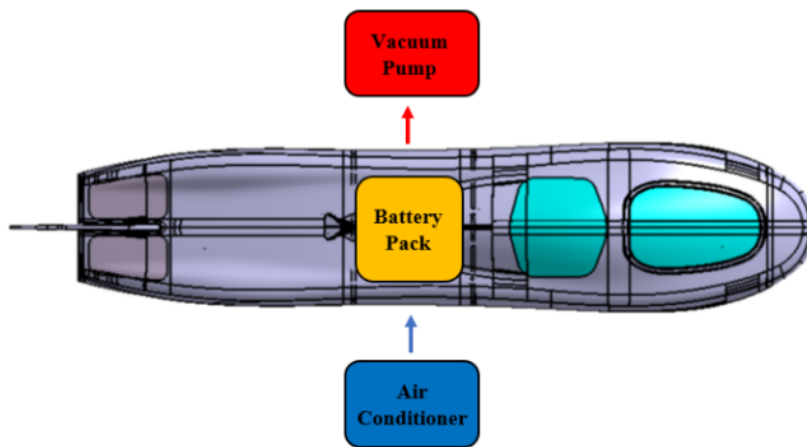


Figure 29: Cooling system layout

Table 7 shows the data of the vacuum pump supplied by the customer.

Voltage [V]	220
Frequency [Hz]	50
Free air displacement [CFM]	2.5
Ultimate Vacuum [Pa]	5
Rotating speed [rpm]	1440
Power [HP]	1/4
Oil capacity [ml]	220
Dimension [mm]	260x110x240
Weight [kg]	7

Table 7: Vacuum pump technical characteristics

Since the cooling system created no longer has internal channels, the air is not able to cool all the cells of the battery pack homogeneously. In order to predict the maximum temperature reached by the cells at the end of the 15 hours of charging, it is necessary to modify the lumped parameter model used for the previous simulation. The new model is analysed in the next subparagraph.

2.5.2 Simscape model with lumped parameters

This subparagraph describes the lumped parameter thermal model used to simulate the maximum cell temperature reached at the end of overnight charging. The model input parameters are the same as described in Table 6.

In this case, it is not possible to use the same correlations of the previous model as the physics of the heat exchange is different. Since there are no ducts, the air flow follows the path of least resistance, making it impossible for the homogeneous passage through all the cells. For this reason, the heat transfer between the cells and the air inside the battery pack is simulated considering the heat exchange by natural convection. To take into account the cooling effect caused by the intake of cold air, the air temperature inside the pack is considered equal to the average value between the cell temperature and the inlet air temperature ($17\text{ }^{\circ}\text{C}$).

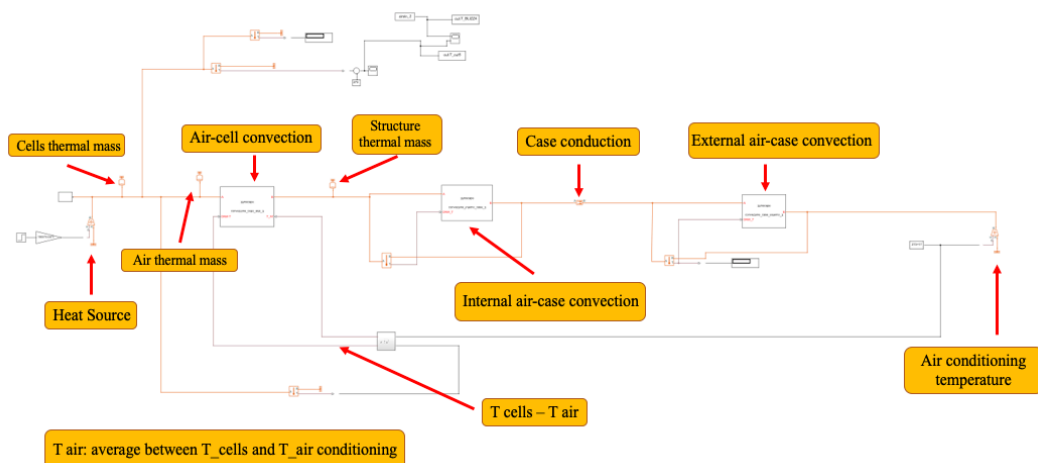
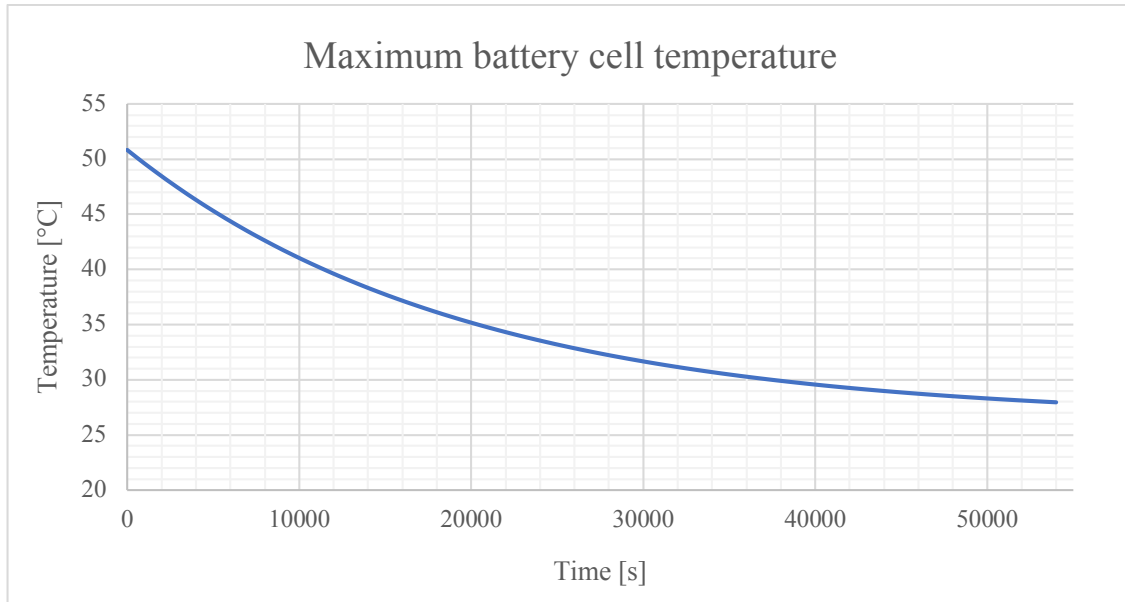


Figure 30: Lumped parameter thermal model of cooling system (ultimate version)

Figure 30 represents the main functional blocks of the Simscape model used to simulate cooling. Unlike the model shown in figure 20, in this case, the block relating to the heat exchange between cells and air by forced convection is not present.

Experimental test



Graph 5: Maximum cell temperature simulated as a function of cooling time

Graph 5 represents the trend of the maximum cell temperature simulated through the lumped parameter model. The simulation is carried out over the entire cooling period equal to 15 hours (54000 s) starting from a maximum cell temperature of 51 °C. The maximum cell temperature reached at the end of the simulation is 28 °C. To validate the results obtained from the simulation, an experimental test lasting three hours was carried out. The description of the test is given in the following paragraph.

2.6 Experimental test

To validate the results of the lumped parameter model, an experimental test lasting 3 hours was carried out. The choice of reducing the cooling time to 1/5 depends on finding the correct balance between time savings and the actual representation of the phenomenon.

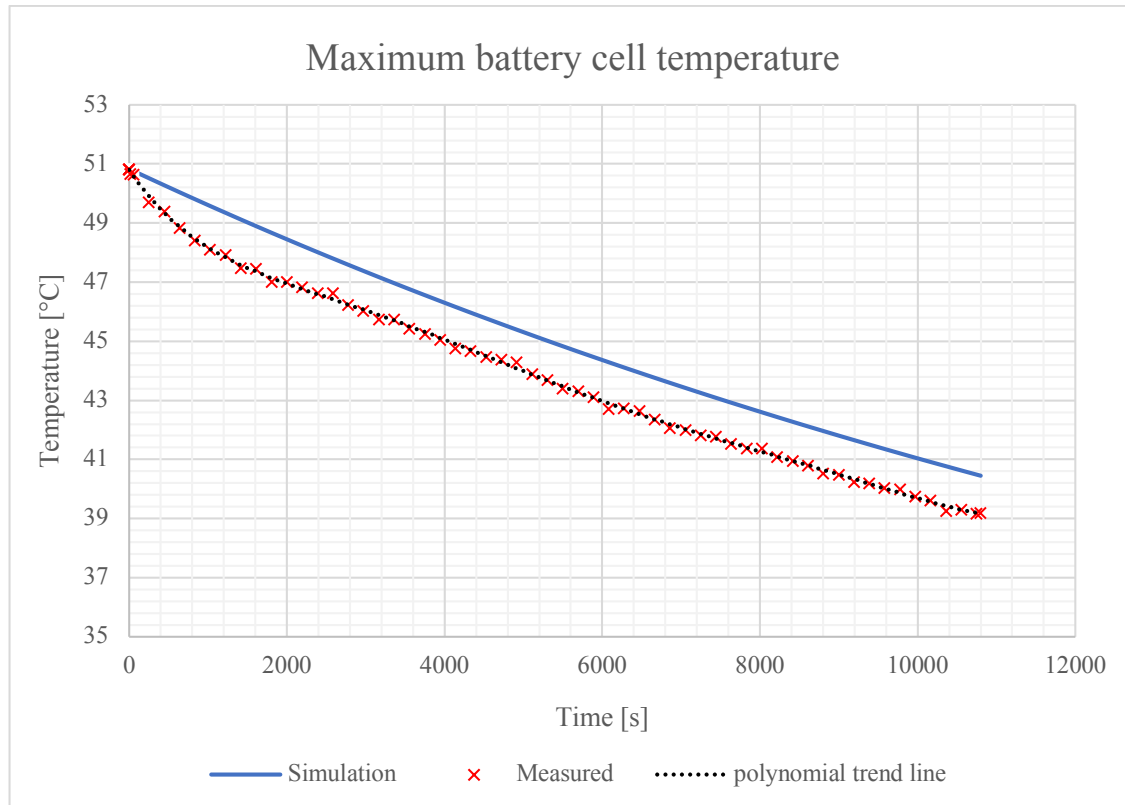
The experimental test was carried out by recharging the vehicle battery at 0.2 C for about 3 hours following the complete discharge carried out at 1.5 C. The layout of the test respects the scheme represented in figure 29.

The next subparagraph represents and analyses the results of the experimental test by comparing them with those obtained through simulation.

2.6.1 Test results

The results of the experimental test are shown in Graphs 6 and 7.

The graph 6 compares the trend of the maximum cell temperature reached during the experimental test with the trend simulated through the Simscape model with lumped parameters described in subparagraph 2.5.2.

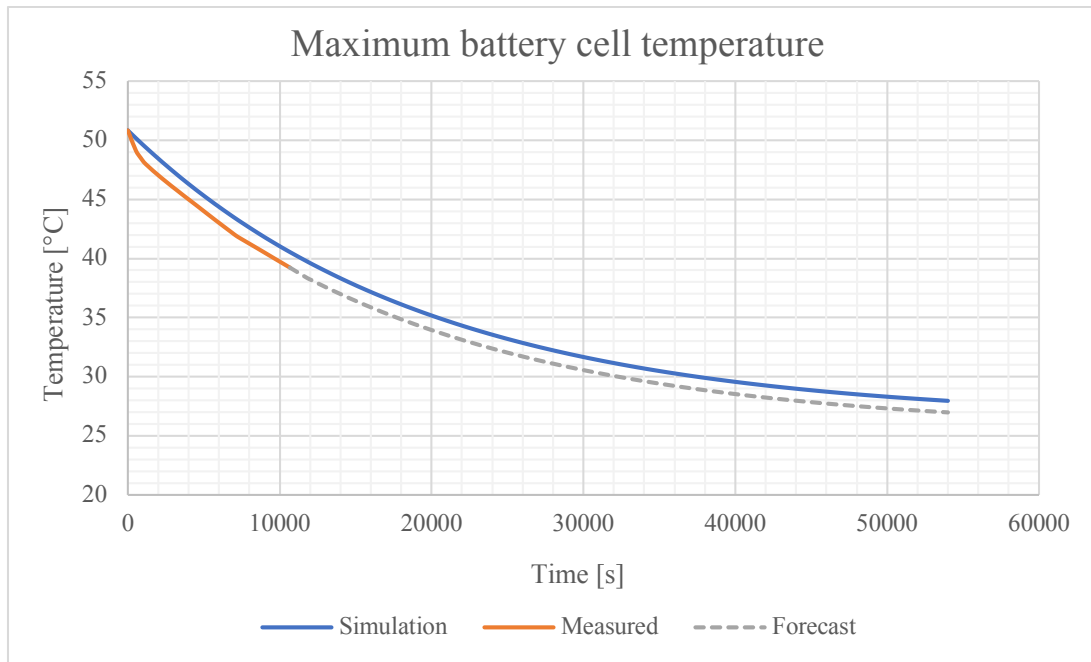


Graph 6: Comparison between the trend over time of the maximum cell temperature simulated and measured

It is interesting to note that the lumped parameter model is in line with the experimental results. The difference between the simulated and measured final temperature is only 1.2 °C.

Unfortunately, due to lack of time, it was not possible to carry out the test for all 15 hours of the recharge scheduled during the test on the track. For this reason, the maximum temperature inside the battery pack at the end of 15 hours was simulated with the Simscape model.

Experimental test



Graph 7: Expected trend of the maximum cell temperature

The graph 7 represents the trend of the maximum cell temperature of the battery pack during the 15 hours of charging. Unfortunately, the duration of the bench test only covers the first 3 hours of charging represented in the graph by the orange curve.

Since in the interval ranging from 0 to 3 hours, the Measured and Simulated graphs show the same trend, it is likely that the real behaviour of the battery pack is like that simulated also in the next 12 hours.

For this reason, the graph 7 represents with a dashed grey line the hypothesized trend of the maximum cell temperature inside the battery pack in the time interval that covers the last 12 hours.

The result of the simulation predicts that, at the end of the 15 hours of recharging, the maximum temperature reached by the cells is equal to 27 °C.

2.7 Conclusions

The comparison between the results obtained from the experimental test and those simulated through the lumped parameter model suggests that the designed cooling system is able to reach the expected target.

The effectiveness of the cooling system was proven during the test in Nardò. On the morning of the second day of testing, after 15 hours of charging, the maximum cell temperature of the battery pack was 26.5 °C.

The pilot Gianmaria Aghem, after the tests carried out, obtained the following category records:

Category VIII Class 1 up to 500 kg (actual 499 kg)

Test	Time [min]	Speed [km/h]
10 miles	04:34.913	210.741
100 km	26:07.160	229.715
100 miles	41:45.806	231.188
1 hour	60	225.184

Table 8: Records achieved in Category VIII Class 1

Category VIII Class 2 from 500 kg to 1,000 kg (actual 507 kg)

Test	Time [min]	Speed [km/h]
10 miles	04:14.671	227.492
100 km	24:40.672	243.133
100 miles	39:45.395	242.859

Table 9: Records achieved in Category VIII Class 2

3 P084 PROJECT

3.1 Problem statement

The second case study concerns the cooling system of an high-performance battery pack for motorsport use. The project plans to develop a cooling system that uses a fluid that flows inside a system of ducts.

The ducts, hereinafter mentioned as “coolers”, because of industrial secrecy, cannot be described in detail. They consist of a mix of materials that give excellent characteristics of flexibility and deformability while ensuring sufficient strength and structural integrity.

The coolant flow rate inside the battery pack is included in the range from 50 to 70 liters per minute.

The hydraulic system includes the coolers of the 4 modules of the battery pack with the addition of the inlet and outlet pipes.

Project objectives

- Maximum pressure drop in the system: 500 mbar at 70 lpm.
- Stacks coolant flow rate ratio equal to 2.5 at 70 lpm and 50 lpm.

3.2 Fluid dynamics analysis of cooling components

3.2.1 Introduction

This paragraph describes the fluid dynamics analysis carried out on the coolers of the battery pack. The study includes the implementation of simulations:

- **Stationary:** to evaluate the pressure drop and the flow velocity along the coolers.
- **Transient:** to analyse the behaviour of the coolant during the filling of the cooler.

The paragraph is divided into 8 subparagraphs; following the introduction, in subparagraph 2, the geometry of the problem and the relative values of the constant parameters involved are defined. Subparagraph 3 presents the setup used for the simulations and in particular the boundary conditions and the chosen physics. Subparagraph 4 deals with the definition of the mesh.

Subparagraph 5 describes the grid independence study carried out for the stationary simulation. Subparagraphs 6 and 7 show the results of the stationary and transient simulations, respectively. Finally, in subparagraph 8, the validation of the pressure drop results obtained through the stationary simulations is reported.

3.2.2 Geometry and parameters

Physical domain

The simulated coolers are:

- Short cooler with 1.9 mm diameter calibrated holes.
- Short cooler with 1.8 mm diameter calibrated holes.
- Long cooler with 2.0 mm diameter calibrated holes.
- Long cooler with 2.5 mm diameter calibrated holes.

As the geometry is not symmetrical due to the presence of the inlet and outlet ducts both located on the same side, it is necessary to simulate the coolers in their entirety. Figures 31 and 32 represent the coolers simulated by extracting the internal volume.

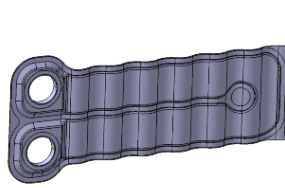


Figure 31: Short cooler CAD model

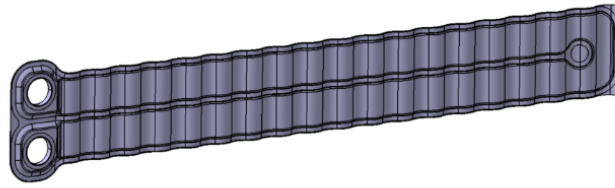


Figure 32: Long cooler CAD model

Table 10 shows the geometric parameters of the coolers.

Long cooler length [m]	0.824
Short cooler length [m]	0.206
Section area [m ²]	2.29e-5

Table 10: Coolers geometric parameters

Fluid properties

The fluid used for cooling is a mix consisting of 90% water and 10% ethylene glycol. The values of the properties of the fluid at the test temperature equal to 25 °C are shown in table 11.

Properties	Value
Density [kg/m ³]	1013
Dynamic viscosity [Pa*s]	0.001183
Kinematic viscosity [m ² /s]	1.1662E-06
Specific heat [J/kg/K]	4087
Thermal conductivity [W/m/K]	0.52

Table 11: Fluid properties

3.2.3 Simulation setup

Computational domain

Since the simulation domain has no periodicity, periodic boundary conditions cannot be applied to allow the complete development of the flow. For this reason, to allow the flow to develop completely, ducts with a length equal to eight times the inlet and outlet diameter have been added upstream and downstream of the cooler.

Boundary conditions

The study domain is divided into 4 different boundaries defined as follows:

- **Inlet:** It is set as mass flow inlet. Mass flow rate must be specified. The mass flow rate is set equal to 0.01264 kg/s.
- **Outlet:** It is set as pressure outlet.
- **Cylinders:** This boundary represents the calibrated holes of the coolers. The choice of assigning a separate boundary for this portion of geometry depends on the need to give a custom refinement to the mesh to correctly understanding the phenomena that develop in this delicate area.
- **Wall:** This boundary includes all the rest of the geometry. From the physical point of view it is considered as an adiabatic surface.

Physics

The choice of the most appropriate turbulent model is based on the indications in literature [21]. The most suitable model for the geometry of the problem is the Menter SST $k-\omega$. Since, although the flow inside the coolers is laminar, there is a separation downstream of the calibrated holes. The turbulence model best suited to cope with favourable and adverse pressure gradients within a boundary layer is the $k-\omega$ [21]. The $k-\omega$ models allow to properly analyse the flow near walls. For the Wilcox original $k-\omega$ model, the boundary condition of ω in a free stream, where turbulence kinetic energy $k \rightarrow 0$ and turbulence frequency $\omega \rightarrow 0$, is the most problematic one. To overcome this problem, the Menter SST (Hybrid Shear Stress Transport) model allows the transformation of the $k-\epsilon$ model into a $k-\omega$ model in the near wall region and, the standard $k-\epsilon$ model is used in the fully turbulent region far from the wall [13,21].

Models used for the definition of physics:

- **Tri dimensional:** since the simulation performed has a three-dimensional domain.
- **Steady:** used for stationary simulations.
- **Unsteady:** used for transient simulation.
- **Liquid:** the working fluid taken into consideration is a mixture of water and Ethylene glycol. The properties associated with the fluid are shown in table 11.
- **Segregated Flow:** the segregated approach is the most appropriate for an incompressible fluid.
- **Constant density:** a constant density is assumed.
- **Turbulent:** due to the physical nature of the problem, the turbulent model is an obliged setting.
- **RAS Models:** the Reynolds Averaged Simulation. OpenFOAM includes Reynolds Averaged Simulation turbulence closures based on linear and non-linear eddy viscosity models, and Reynolds stress transport models.
- **SST (Menter) $k-\omega$:** it is an improved variant of the standard $k-\omega$ models, which incorporates the best features of $k-\omega$ and $k-\epsilon$ models.

3.2.4 Mesh generation

Automated 2D mesh

The mesh in the domain is built considering the expected flow behaviour. To ensure the convergence of the turbulent model near the edges of the domain, the mesh is made up of prismatic layers near the perimeter of the duct. The rest of the domain is discretized using hexahedral cells. Due to the nature of the problem, the mesh requirements are less stringent in the regions downstream of the calibrated holes. The choice of the number of prism layers equal to 5 comes from the attempt to obtain a correct representation of the flow near the walls while keeping the computational cost low. The prism layer near wall thickness has been set in such a way as to obtain a y^+ on all the boundaries less than unity.

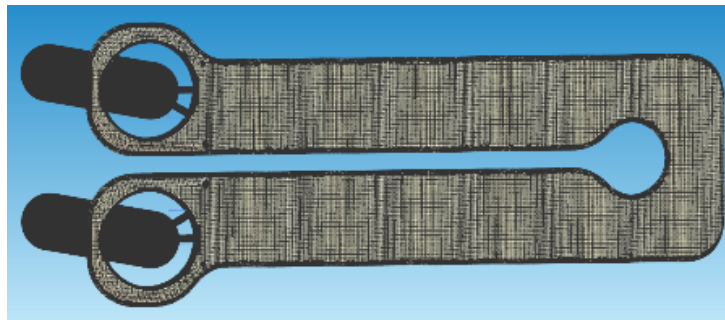


Figure 33: Short cooler mesh representation

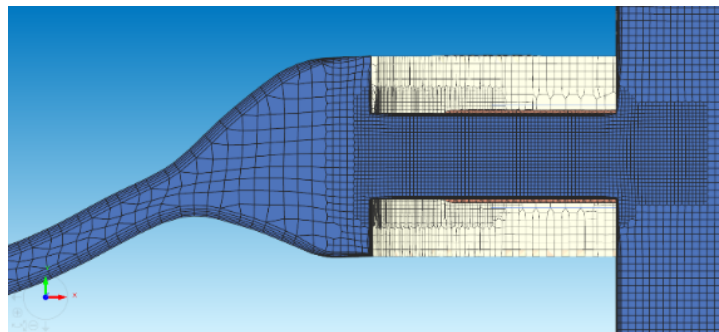


Figure 34: Sectional view of short cooler mesh

To optimize the mesh and facilitate the convergence of residuals, the following **custom controls** have been implemented:

- **Surface control:** the surface controls are implemented by setting the refinement level with respect to the base size value of the simulation. Each level is characterized by a cell size value equal to half the value of the previous level. Table 12 shows the maximum and minimum levels for each boundary used to create the mesh.

Boundary	Minimum	Maximum
Wall	Level 2	Level 1
Inlet	Level 2	Level 0
Outlet	Level 2	Level 0
calibrated holes	Level 3	Level 3

Table 12: Surface control levels

The **volumetric controls** are made near the calibrated holes to accurately capture the flow behaviour.

- 2 **volumetric controls** around the calibrated holes. The refinement level within the volumetric controls is set at level 4.

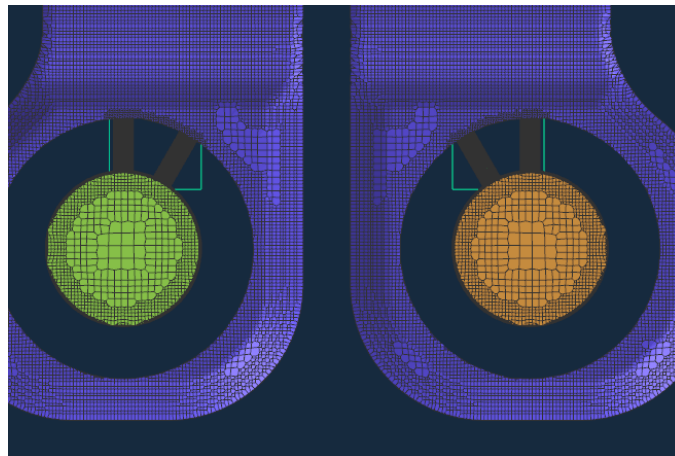


Figure 35: Detail of volumetric controls on the holes

- 2 **cylindrical volumetric controls** in the area adjacent to the calibrated holes with a refinement degree set at level 3 to be able to capture turbulent phenomena and pressure drops due to the passage of fluid through the calibrated holes.

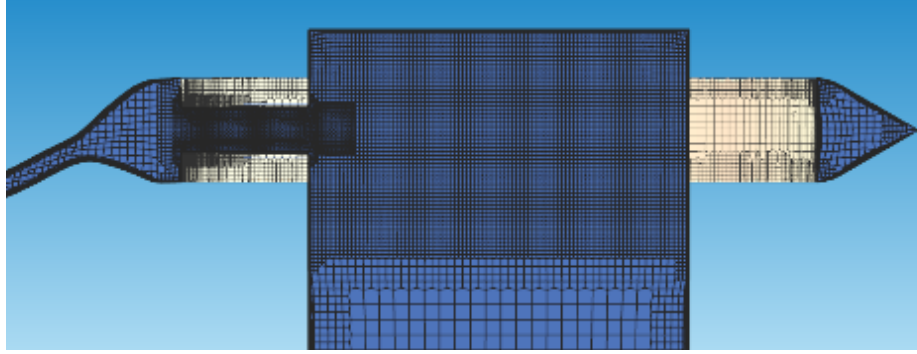


Figure 36: Detail of the cylindrical volumetric control

3.2.5 Grid Independence Study

For the realization of the grid independence study, 3 different meshes are evaluated, progressively refined. The different configurations analysed are shown in table 13. Since all the values used for the definition of the mesh are defined referred to the base size, modifying only this last parameter performs the grid independence study. All three different base size measures ensure a $y^+ < 1$.

N° Prism layers	Base Size [mm]	Number of cells	First cell height [% cell dimension]	Expansion ratio
5	0.6	785037	0.1	1.2
5	1	335005	0.1	1.2
5	1.3	126117	0.1	1.2

Table 13: Characteristics of the mesh used for the grid independence study

As mentioned in the book written by Roache [15], the grid independence study is performed relative to the parameters of greatest interest for the simulation.

As reported in Table 14, the following parameter is monitored:

- Pressure drop across the domain, $\Delta P / \rho$ (surface quantity).

For the calculation of the above parameter, a simultaneous asymptotic tolerance up to 1×10^{-4} together with residual values lower than 1×10^{-5} is set as the stopping criterion.

The analysis of the Grid independence study is carried out for a fixed value of mass flow inlet equal to 0.01264 kg/s.

The results obtained are reported in table 14.

The grid independence study is carried out through 7 steps as reported in [19].

1. Completing at least 3 simulations (fine, intermediate, coarse) with a constant refinement ratio, $r > 1.3$ between them
2. Choosing a parameter indicative of grid convergence
3. Calculating the order of convergence p

$$p = \frac{\ln \left(\frac{\phi_3 - \phi_2}{\phi_2 - \phi_1} \right)}{\ln r} \quad (1)$$

4. Performing a Richardson extrapolation to predict the value at $h=0$

$$f(h = 0) = \phi_1 + \frac{\phi_1 - \phi_2}{r^p - 1} \quad (2)$$

5. Calculating the Grid Convergence Index (GCI) for medium and fine refinement levels

$$GCI_{12} = \frac{1,25 * |\varepsilon_{12}|}{r^p - 1} \quad (3)$$

6. Calculating the Grid Convergence Index (GCI) for medium and coarse refinement levels

$$GCI_{23} = \frac{1,25 * |\varepsilon_{23}|}{r^p - 1} \quad (4)$$

7. Ensuring that grids are in the asymptotic range of convergence by checking

$$\frac{GCI_{23}}{r^p * GCI_{12}} \approx 1 \quad (5)$$

For the calculation of r , the *effective grid refinement ratio* $r = (N1 / N2)^{1/3}$ is used since this r can also be used for *unstructured grids*. N is the number of cells for each configuration [16].

Fluid dynamics analysis of cooling components

Base size [mm]	N_o of prism layer	$\Delta P/\rho$ short 1.9	$\Delta P/\rho$ short 1.8	$\Delta P/\rho$ long 2.5	$\Delta P/\rho$ long 2.0
0.6	5	12.532	13.61957	11.62714	15.73686
1	5	12.6159	13.71137	11.70604	15.84438
1.3	5	12.9315	14.06317	12.0143	16.2729
Relative error % 1		0.669486	0.673998	0.678572	0.683208
Relative error % 2		2.501605	2.565791	2.633358	2.704579
Extrapolated error %		0.243014	0.238521	0.233968	0.229352
Richardson extrapolation		12.50162	13.58716	11.6	15.70085
GCI ₁₂		0.303031	0.297442	0.291777	0.286034
GCI ₂₃		1.132308	1.132308	1.132308	1.132308
p		5.040919	5.111925	5.185266	5.261074
Solution convergence		0.99335	0.993305	0.99326	0.993214
Maximum error		3.324291	3.384791	3.448396	3.51535
Pressure drop [mbar]		126.6414	138	117.508	159.0496

Table 14: Grid Independence Study results

The CFD software returns the pressure value divided by the density of the fluid as an output variable. The 4 columns of the table refer to the 4 different simulated coolers. As expected, for all four simulated coolers, the Grid Convergence Index values decrease from the coarse configuration to the fine configuration. The solution convergence value tends to 1 in all analysed coolers ensuring that all grids are in an asymptotic range of convergence. The last row of table 14 shows the real pressure drop in each cooler predicted by the simulation.

3.2.6 Steady state simulations results

In this section the results of the simulations of all four coolers are shown and described. For each cooler, the contours relating to pressure and flow velocity are shown.

Short 1.9 mm cooler pressure distribution

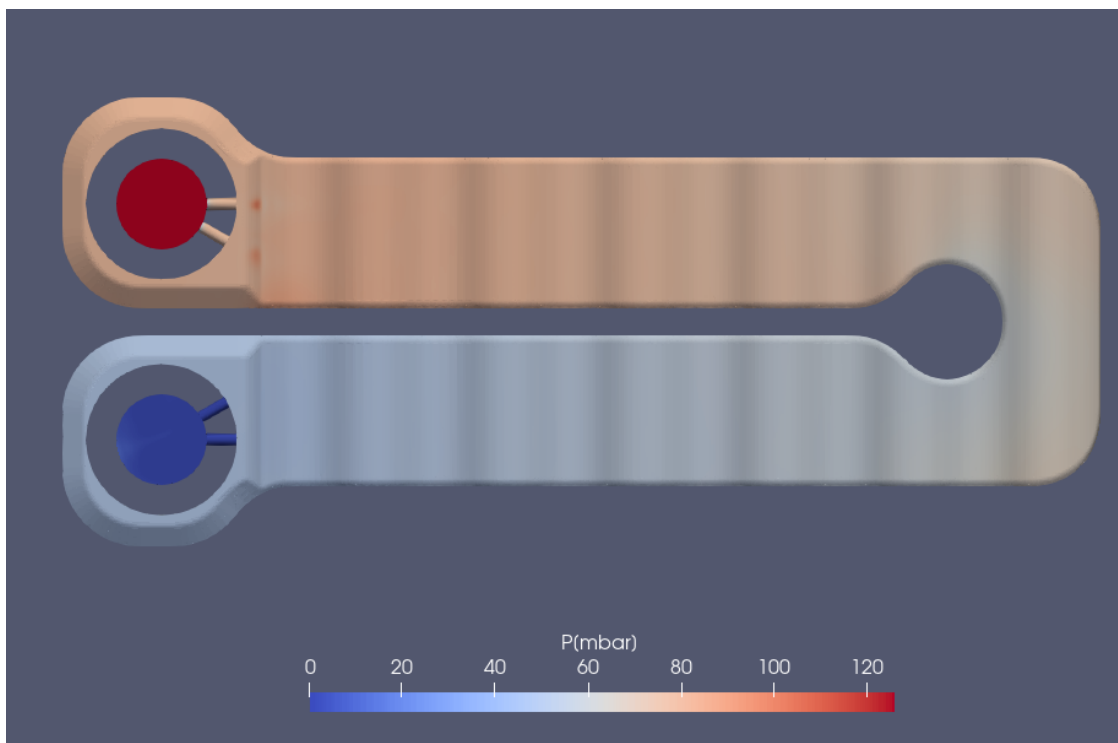
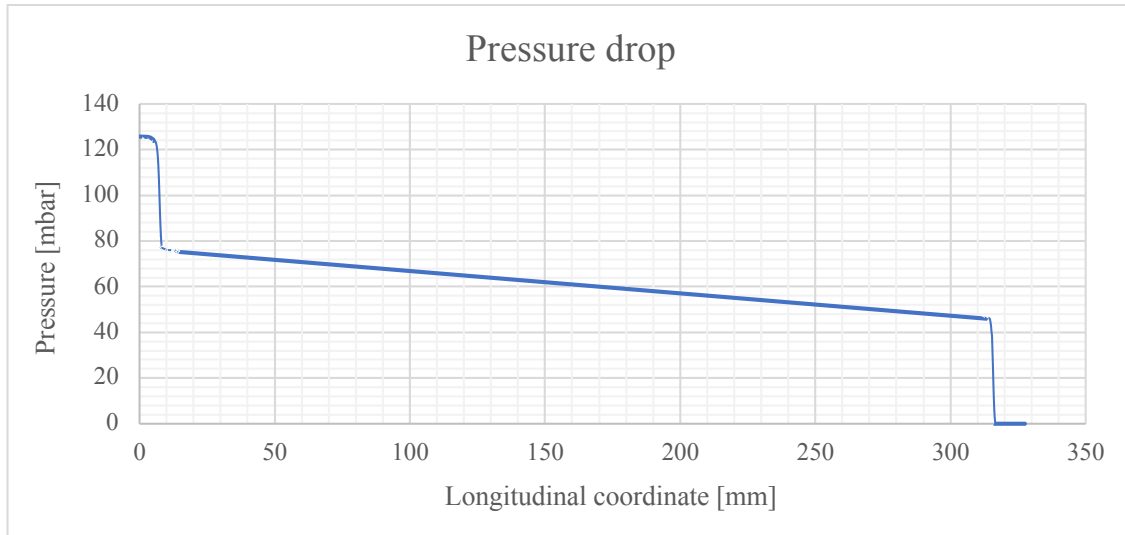


Figure 37: Short 1.9 mm cooler pressure contour

Figure 37 shows the pressure distribution on the short cooler having the calibrated holes with a diameter of 1.9 mm. The analysis of the figure shows how the calibrated holes are the major cause of the pressure drop. It is interesting to note that at the outlet of the two calibrated inlet holes there are two high pressure points where the flow collides with the side walls of the cooler. This behaviour depends on the geometry of the cooler which does not convey the flow but hinders it.



Graph 8: Short 1.9 mm cooler pressure trend

The analysis of graph 8 shows how the pressure drop has a linear trend along the cooler and has two jumps in correspondence with the calibrated holes equal to 44 mbar each. The total pressure drop is 125 mbar of which about 1/3 occurs along the duct and 2/3 through the calibrated holes.

Short 1.9 mm cooler velocity contour

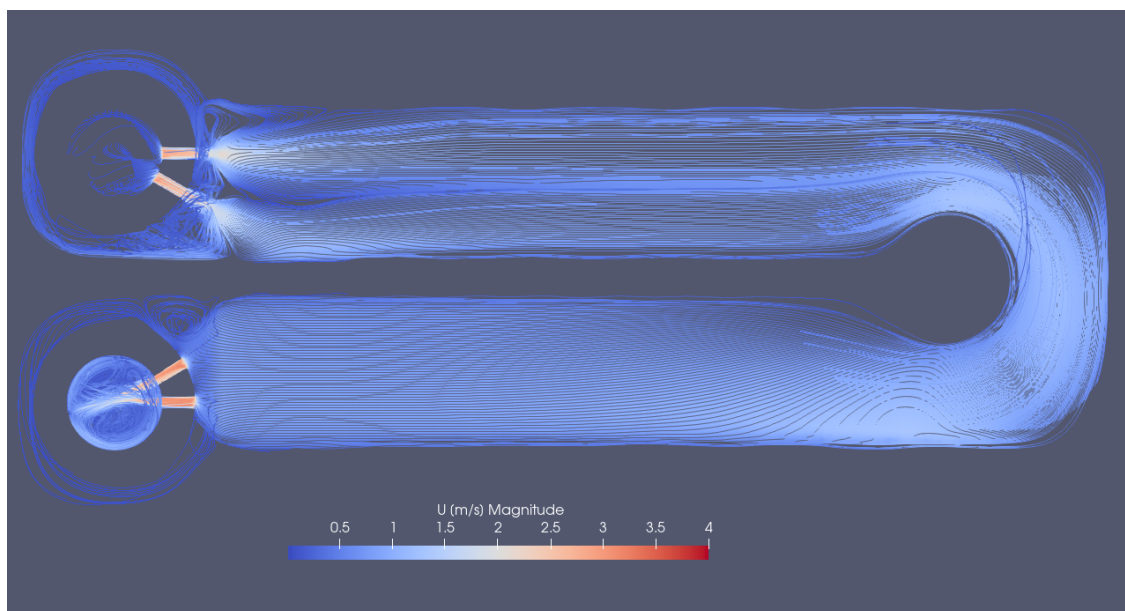


Figure 38: Short 1.9 mm cooler velocity contour (streamlines representation)

Figure 38 shows the speed of the fluid flowing inside the cooler represented through the streamlines. It is interesting to note that the flow behaviour inside the cooler is

almost always laminar; the absence of swirling structures along the cooler guarantees the homogeneous cooling of all the cells in contact with the surface. The only swirling structures that are formed are located downstream the calibrated holes. Downstream of the calibrated holes, due to the slowdown and expansion of the flow, the separation takes place. As the flow expands, an adverse pressure gradient forms which causes separation. Flow separation produces turbulent recirculating flow zones with mechanical energy losses. Vortexes form only in the area adjacent to the calibrated holes and do not have a negative effect on cooling.

$Q_{in_0^\circ}$ [%]	$Q_{in_30^\circ}$ [%]	$Q_{out_30^\circ}$ [%]	$Q_{out_0^\circ}$ [%]
55	45	45	55

Table 15: Coolant flow distribution in the short 1.9 mm cooler

Table 15 represents the flow rate of coolant in percentage that passes inside the calibrated holes. From the table the distribution of the flow rate between the horizontal holes and the 30° inclined holes is the same both at the inlet and outlet. 55% of the flow passes inside the horizontal holes while 45% in the inclined ones. The geometric orientation of the holes is the reason why the flow at the exit of the cooler has a turbulent behaviour as shown in figure 38.

Short 1.8 mm cooler pressure distribution

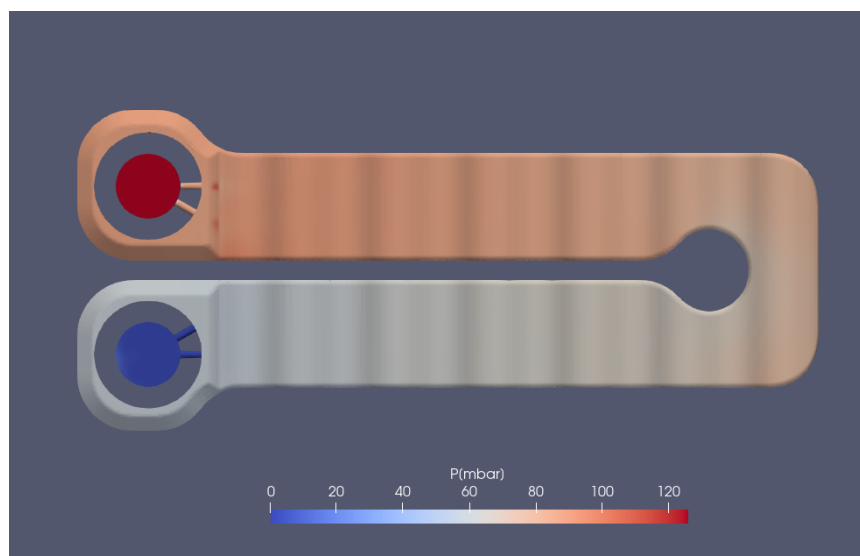
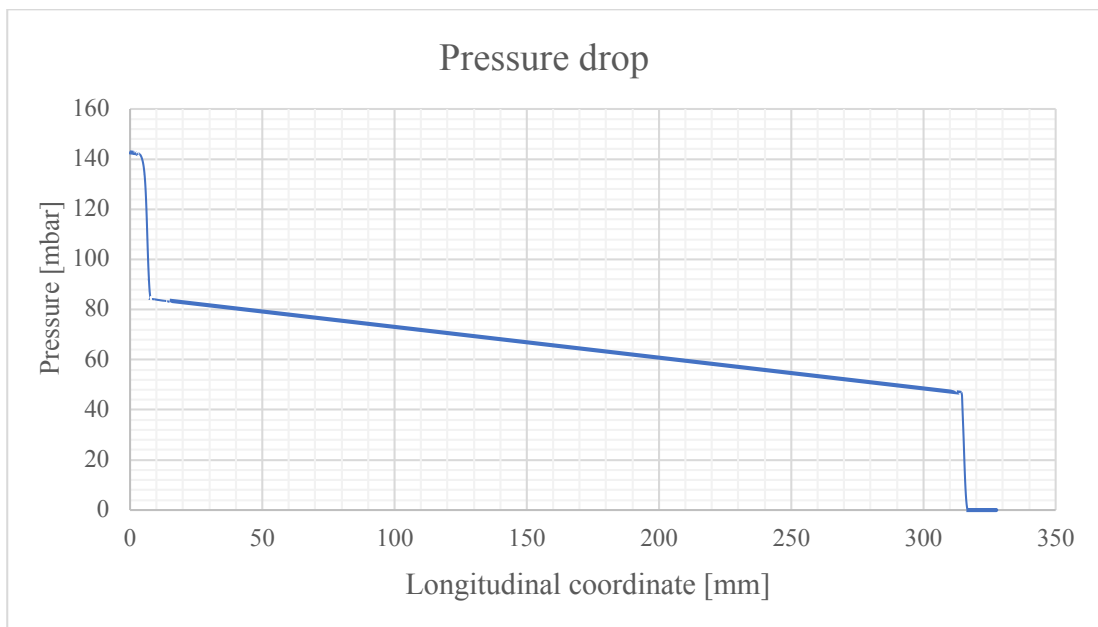


Figure 39: Short 1.8 mm cooler pressure contour

Fluid dynamics analysis of cooling components

Figure 39 shows the pressure distribution on the short cooler having the calibrated holes with a diameter of 1.8 mm. The analysis of the figure shows how the calibrated holes are the major cause of the pressure drop. It is interesting to note that at the outlet of the two calibrated inlet holes there are two high pressure points where the flow collides with the side walls of the cooler. This behaviour depends on the geometry of the cooler which does not convey the flow but hinders it.



Graph 9: Short 1.8 mm cooler pressure trend

The analysis of graph 9 shows how the pressure drop has a linear trend along the cooler and has two jumps in correspondence with the calibrated holes equal to 57 and 43 mbar. The total pressure drop is 141 mbar, 11% more than the version with 1.9 mm calibrated holes. In this configuration the pressure drop along the inlet holes is about 40% of the total drop while that along the outlet holes is 30%. The remaining pressure drop occurs along the cooler.

Short 1.8 mm cooler velocity contour

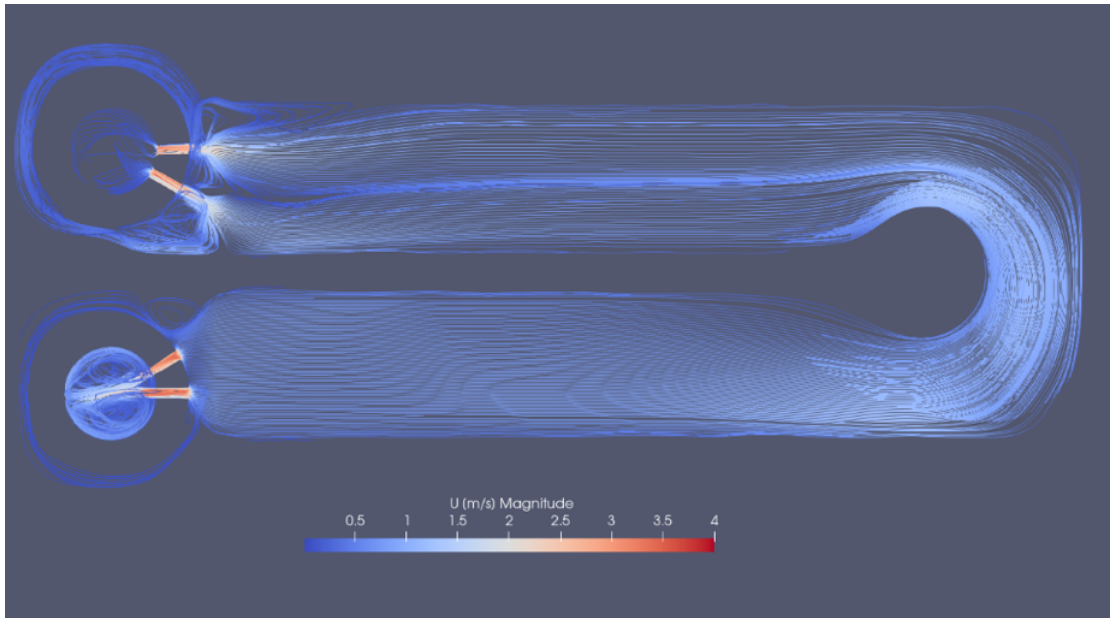


Figure 40: Short 1.8 mm cooler velocity contour (streamlines representation)

Figure 40 shows the speed of the fluid flowing inside the cooler represented through the streamlines. It is interesting to note how the flow behaviour inside the cooler is laminar as in the previous case. The absence of swirling structures along the cooler ensures homogeneous cooling of all the cells in contact with the external surface. Also in this case, downstream of the calibrated holes there are small, isolated vortices. Swirls are formed as a result of flow separation at the outlet of the calibrated holes. Their size and location do not affect cooling.

$Q_{in_0^\circ}$ [%]	$Q_{in_30^\circ}$ [%]	$Q_{out_30^\circ}$ [%]	$Q_{out_0^\circ}$ [%]
55	45	45	55

Table 16: Coolant flow distribution in the short 1.8 mm cooler

Table 16 represents the flow rate of coolant in percentage that passes inside the calibrated holes. The results are the same as those obtained from the previous simulation. The flow is sufficiently balanced between the calibrated holes. Also in this case, at the exit of the cooler there is a turbulent region due to the geometry of the holes that concentrate the two outgoing flows generating swirling structures.

Long 2.0 mm cooler pressure distribution

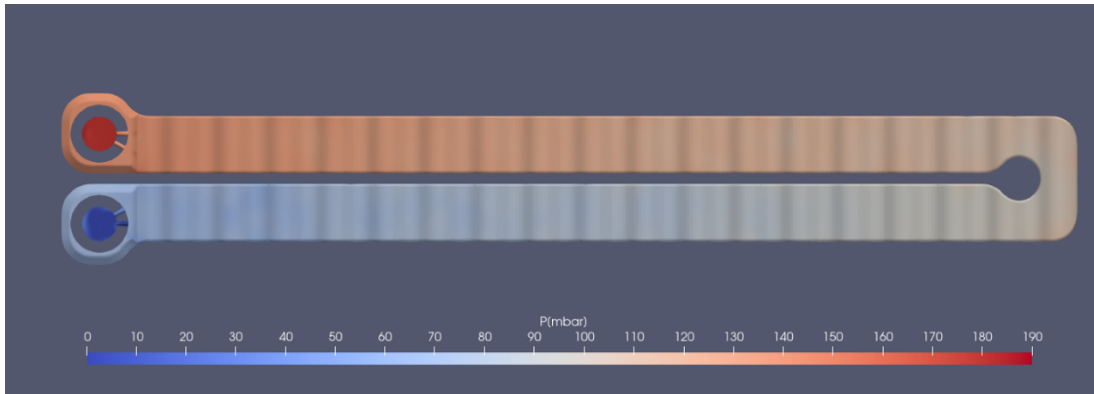
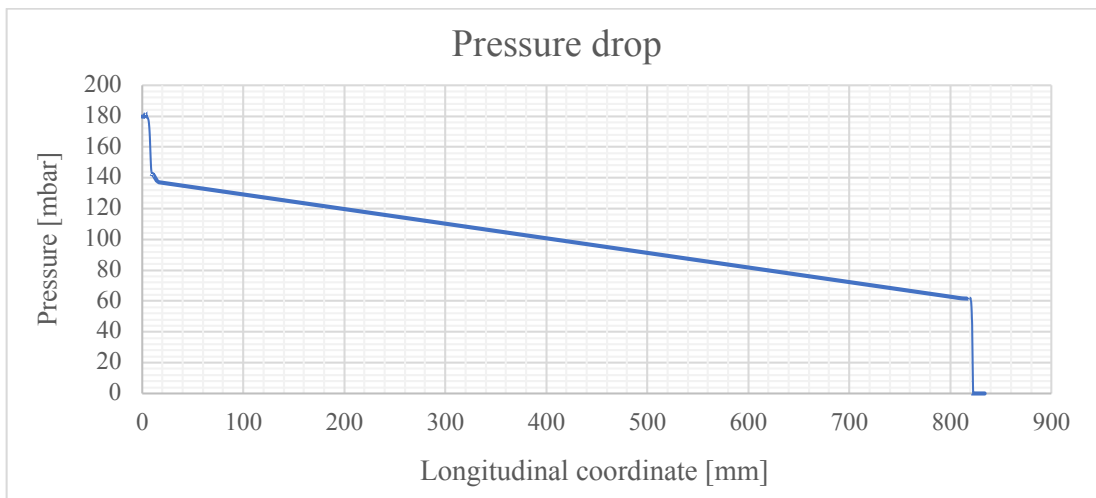


Figure 41: Long 2.0 mm cooler pressure contour

Figure 41 shows the pressure distribution on the surface of the long cooler having the calibrated holes with a diameter of 2 mm. The analysis of the figure shows that the calibrated holes are no longer the major cause of the pressure drop. It is interesting to note that at the outlet of the two calibrated inlet holes there are two high pressure points where the flow collides with the side walls of the cooler.



Graph 10: Long 2.0 mm cooler pressure trend

The analysis of graph 10 shows how the pressure drop has a linear trend along the cooler and has two jumps in correspondence with the calibrated holes equal to 36 and 58 mbar. The total pressure drop is approximately 178 mbar. Pressure drop along the inlet holes is about 20% of the total drop while that along the outlet holes is about 33%. The remaining pressure drop occurs along the cooler. Pressure drop along the cooler becomes equal to that along the calibrated holes due to an increase in the length of the duct equal to 4 times the previous one.

Long 2.0 mm cooler velocity contour

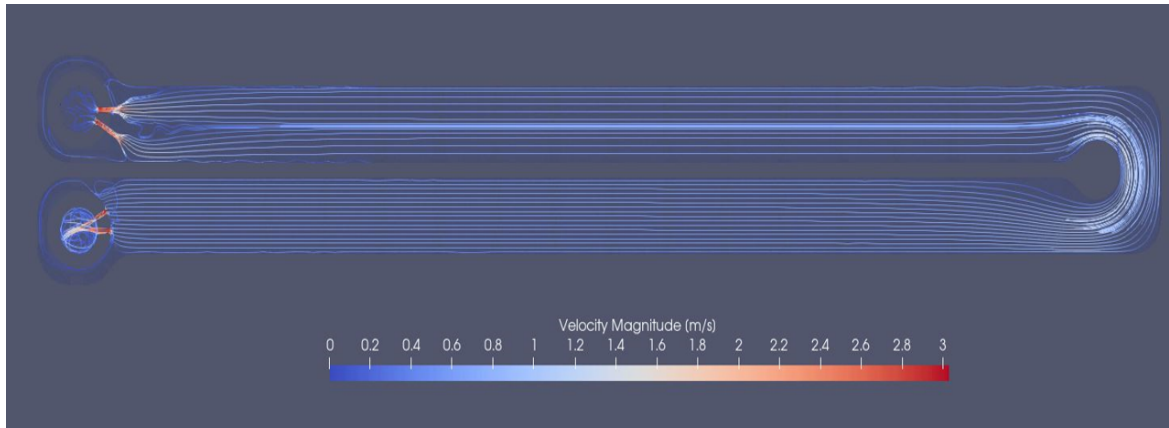


Figure 42: Long 2.0 mm cooler velocity contour (streamlines representation)

Figure 42 shows the contour of the flow velocity inside the cooler through the streamlines. As can be seen from the figure, the flow inside the cooler is laminar. This behavior ensures homogeneous heat exchange between the coolant and the cells in contact with the cooler surface. Downstream of the inlet calibrated holes there is a small area where the flow is turbulent. This behavior, which ends after a few centimeters, is due to the expansion of the flow at the outlet. Swirls are formed as a result of flow separation at the outlet of the calibrated holes. Their size and position do not affect cooling. Downstream of the calibrated outlet holes, the flow is turbulent due to the geometry of the holes that lead to mixing of the outgoing flows.

$Q_{in_0^\circ}$ [%]	$Q_{in_30^\circ}$ [%]	$Q_{out_30^\circ}$ [%]	$Q_{out_0^\circ}$ [%]
52	48	49	51

Table 17: Coolant flow distribution in the long 2.0 mm cooler

Table 17 shows the percentage of flow that passes inside the calibrated inlet and outlet holes. From the values shown in the table it can be seen that the flow rate of fluid that passes inside the horizontal hole and inside the 30° inclined hole is almost identical both at the inlet and at the outlet.

Long 2.5 mm cooler pressure distribution

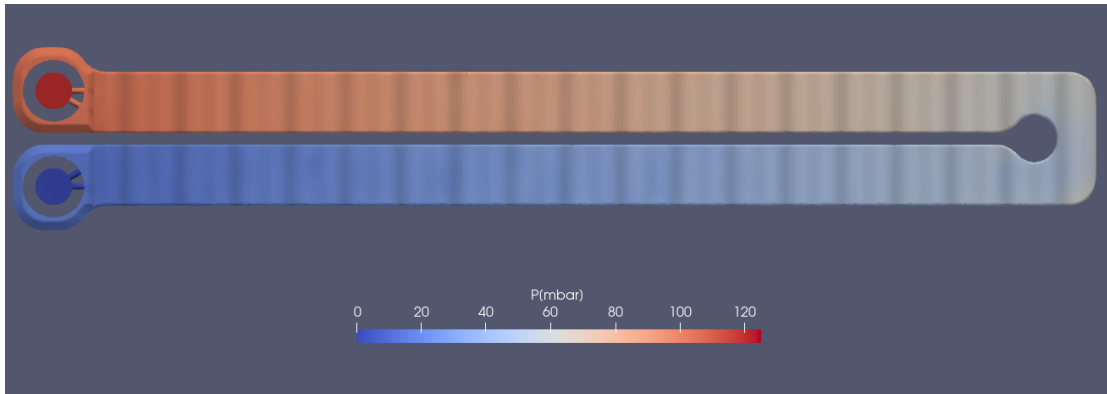
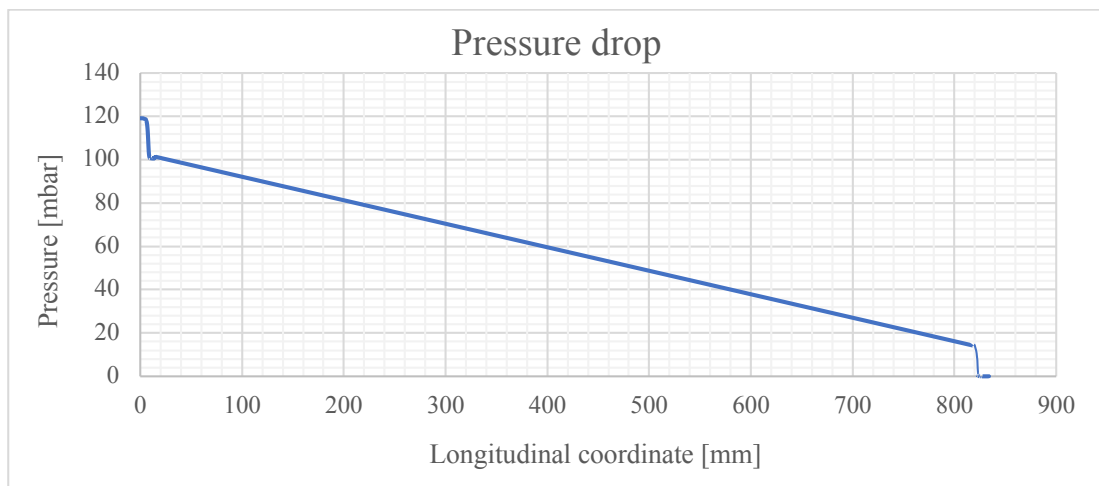


Figure 43: Long 2.5 mm cooler pressure contour

Figure 43 shows the pressure distribution on the long cooler having the calibrated holes with a diameter of 2.5 mm. The analysis of the figure shows that the calibrated holes are no longer the major cause of the pressure drop. It is interesting to note that at the outlet of the two calibrated inlet holes there are two high pressure points where the flow collides with the side walls of the cooler.



Graph 11: Long 2.5 mm cooler pressure trend

The analysis of graph 11 shows how the pressure drop has a linear trend along the cooler and has two jumps in correspondence with the calibrated holes equal to 16 and 11 mbar. The total pressure drop is 119 mbar. In this configuration, the pressure drop along the inlet holes is about 13% of the total drop while that along the outlet holes is about 9%. The remaining pressure drop occurs along the cooler. Contrary to the configurations already described, the pressure drop along the cooler becomes the dominant contribution due to an increase in the diameters of the calibrated holes.

Long 2.5 mm cooler velocity contour

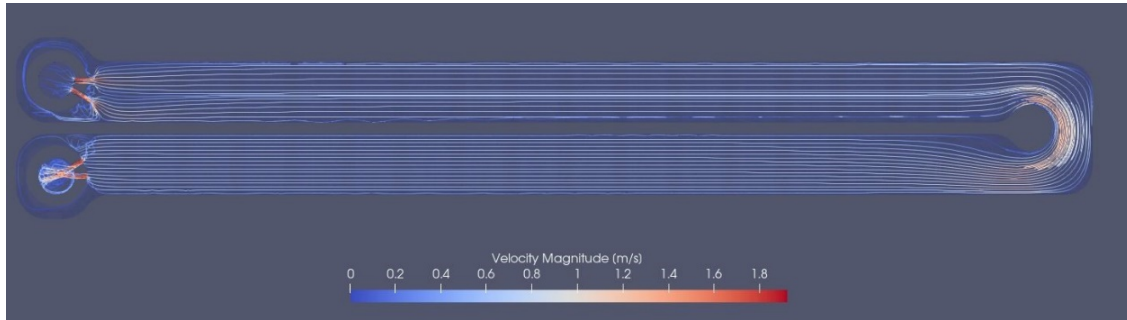


Figure 44: Long 2.5 mm cooler velocity contour (streamlines representation)

Figure 44 shows the contour of the flow velocity inside the cooler through the streamlines. Also in this case, the flow inside the cooler is laminar. This behavior allows a homogeneous heat exchange between the cells and the coolant. Unlike the previously analyzed configuration, due to the larger diameter of the calibrated holes, the turbulence zone downstream of the inlet calibrated holes is reduced. As in the previous configuration, downstream of the calibrated outlet holes the flow is turbulent due to the mixing of the two flows.

$Q_{in_0^\circ}$ [%]	$Q_{in_30^\circ}$ [%]	$Q_{out_30^\circ}$ [%]	$Q_{out_0^\circ}$ [%]
49	51	50	50

Table 18: Coolant flow distribution in the long 2.5 mm cooler

Table 18 shows the percentage of coolant that flows inside the calibrated inlet and outlet holes. In this configuration, an almost perfect balance of the flow of coolant flowing inside the calibrated holes is achieved due to the increase in the diameter of the latter.

3.2.7 Transient simulation results

This subsection shows the results of the transient fluid dynamics simulation carried out on the long cooler with 2.0 mm diameter calibrated holes. The choice to carry out the transient simulation only on the 2.0 mm long cooler is based on the need to verify the behaviour of the coolant during the filling phase in the most critical configuration (longest type of cooler having the smallest calibrated holes).

The simulation time step has been chosen equal to 0.08 s. This value is equivalent to 1/20 of the time it takes for a fluid particle to cross the entire cooler.

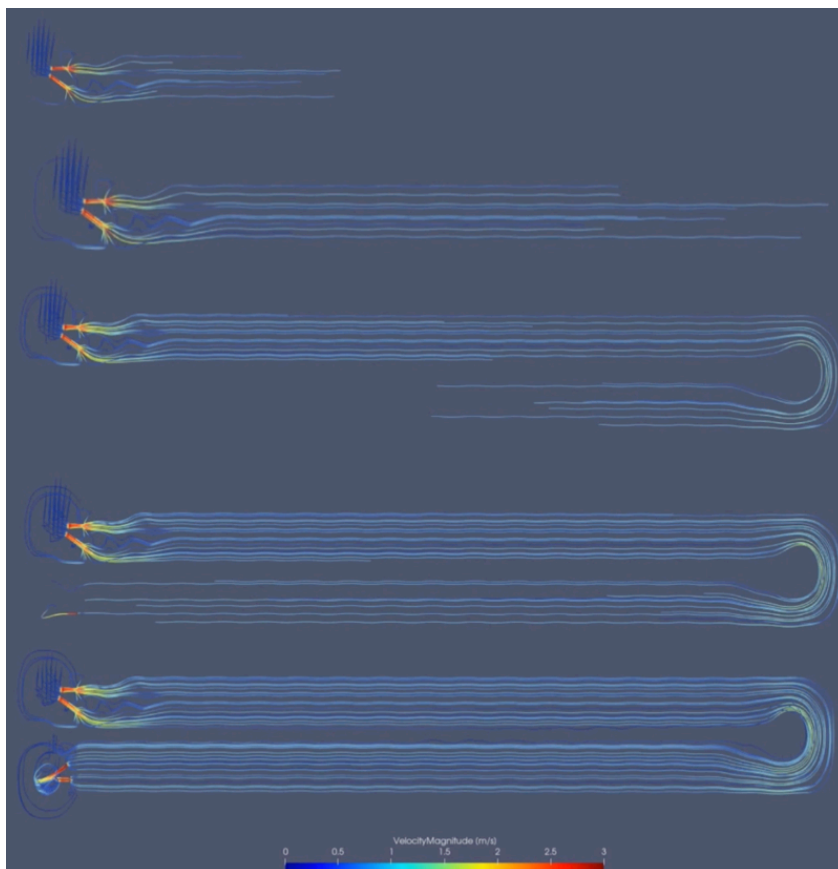


Figure 45: Cooler filling stages. Transient CFD simulation

Figure 45 shows, through the streamlines, the behaviour of the fluid during the filling phase of the cooler. The quantity represented is the velocity of the fluid in m/s. The flow behaviour inside the cooler is laminar and the filling is homogeneous. In a small region, immediately downstream of the calibrated inlet holes, there are small eddies due to flow separation as a result of expansion. Immediately afterwards, the flow stabilises and remains laminar along the entire length of the cooler. Downstream of the outlet holes, the flow is turbulent due to mixing.

3.2.8 Validation

For the validation of the CFD steady state simulations, the pressure drop values provided by the cooler manufacturers were used.

Cooler	Pressure drop experimental [mbar]	Pressure drop CFD [mbar]
Short 1.8	238	141
Short 1.9	215	125
Long 2.0	290	178
Long 2.5	186	119

Table 19: Comparison between simulated and experimental pressure drop values for the different types of coolers

From the analysis of table 19 it is evident that the pressure drop along the coolers obtained through the experimental tests of the suppliers is greater than that obtained through fluid dynamics simulations. To verify the accuracy of the results entered in table 19 and evaluate the real pressure drop within each cooler, a simplified battery pack was created to carry out experimental tests. The characteristics of the simplified battery pack and the experimental tests carried out are described in paragraph 3.3.

3.3 Minimodules

3.3.1 Problem statement

The discussion of this chapter analyses the structure of a simplified battery pack equivalent to the real one both from an electrical and hydraulic point of view. The choice to create a simplified model is based on the need to validate the results obtained from the models through:

- Experimental hydraulic tests
- Experimental thermal tests

Objectives

1. Validating the pressure drop along the coolers.
2. Evaluating the coolant flow distribution in each simplified battery pack cooler with 7.5 lpm inlet flow.
3. Maximum cell temperature reached following a cycle of 10s of charge and 10s of discharge at $1C < 35\text{ }^{\circ}\text{C}$.

3.3.2 Introduction

The simplified battery pack consists of two minimodules hydraulically connected in parallel. The first minimodule consists of 5 short coolers which cool 4 rows of cells made up of 6 elements each; the second minimodule consists of 5 long parallel coolers which also cool 4 rows of cells each consisting of 18 elements.

Since the external coolers only cool half of a row of cells, unlike the internal ones which cool 1 row of cells each, the calibrated holes have been made trying to ensure an unbalance of flow rate such as to allow the homogeneous cooling of all the cells at the inside the modules. For this reason, the external coolers of the small minimodule have a diameter of the calibrated holes equal to 1.8 mm while those relating to the internal coolers 1.9 mm.

In the same way, the calibrated holes of the external coolers of the long minimodule have a diameter of 2 mm, 0.5 mm lower than the holes of the central coolers.

Figure 46 represents the simplified battery pack CAD model.

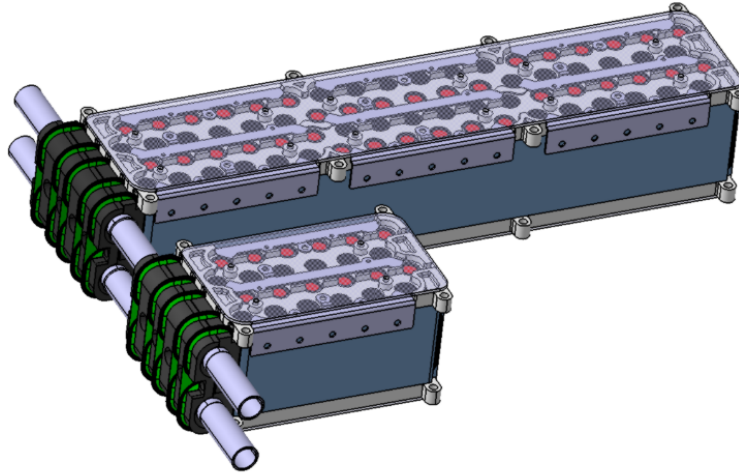


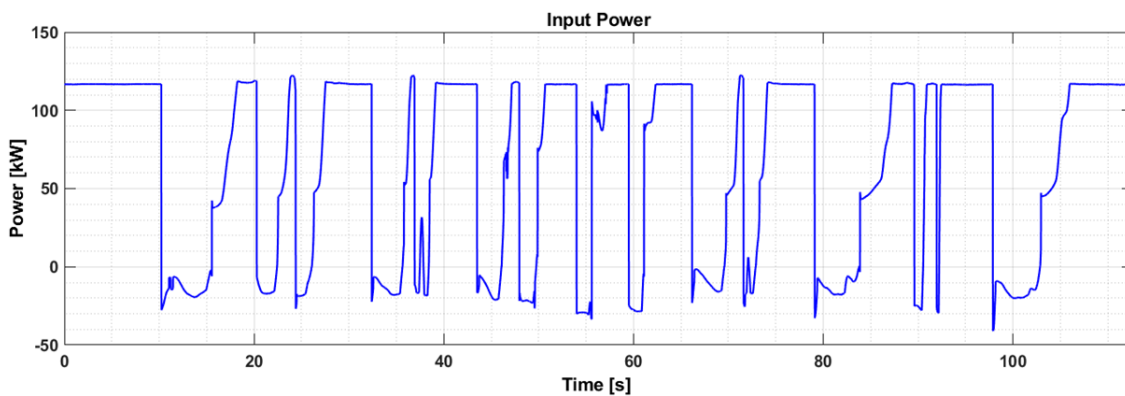
Figure 46: Simplified battery pack CAD model

The electrical equivalence between the two battery packs is guaranteed using the same type of cells assembled with the same technology. The number of parallels is the same for the two battery packs so that the same current can be discharged.

The hydraulic equivalence is guaranteed using the same coolers assembled in the same configuration (all in parallel).

The cycle used to test the simplified battery pack belongs to the mission profile defined with the customer scaled for the 16s 6p configuration.

The mission profile defined for the simulation and validation of the project is shown in graph 12. The profile will from now on be defined as MP110kW.



Graph 12: Mission profile used for simulation and validation

Minimodules

The MP110kW mission profile is used following a usage map (table 20) necessary for the characterization of the battery in relation to:

- Instant early life performance (BOL)
- Instant performance at the end of life (EOL)
- Full cycling to simulate useful life

Performance target	Reference mission profile	BCs	Repetitions (laps)	Output
Race (BOL)	MP110kW (1 lap)	- Ambient temp: 20°C - Coolant init. Temp: 20°C - Coolant flow rate: 70lpm	7-8	- To be completed with 1 charge - Temperatures not to exceed safety values - Voltages/currents to be within safety range
Race (BOL)		- Ambient temp: 40°C - Coolant init. Temp: 40°C - Coolant flow rate: 70lpm		
Battery life	Race		> 60	- Overall number of laps at EOL in each race event not < 7
Race (EOL)	MP110kW (1 lap)	Same as Race (BOL)	7-8	Same as Race (BOL) Number of laps not < 7

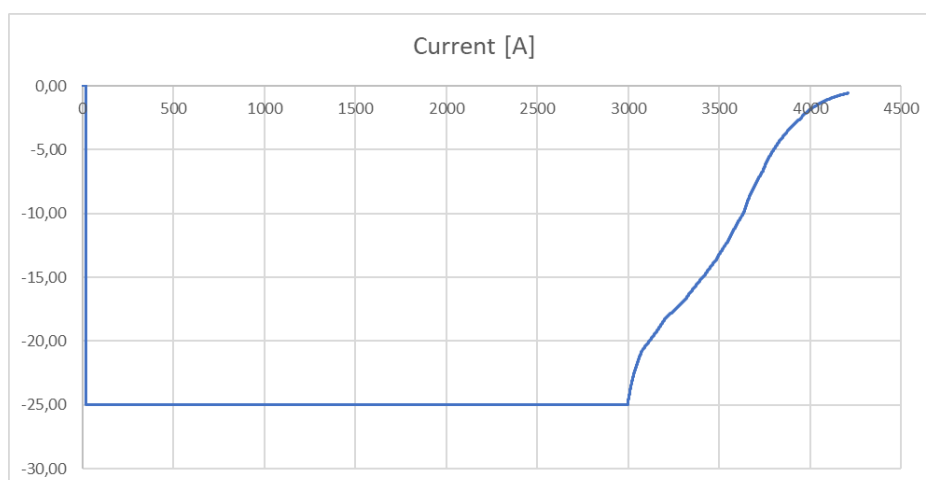
Table 20: Usage map to characterize the battery pack

Table 21 schematically represents the parameters relating to the electrical and hydraulic equivalence of the two battery packs.

	Battery Pack	Simplify Battery Pack
Cells	MOLICEL INR-21700-P42B	MOLICEL INR-21700-P42B
Electric configuration	192s 6p	16s 6p
Welding materials	Aluminium 99.99%	Aluminium 99.99%
Welding technologies	Heavy Wire bonding	Heavy Wire bonding
Cooling system	Flexible coolers	Flexible coolers
Mission profile charge/discharge	Charge: profile CCCV 25A max Discharge: Table 15	Charge: profile CCCV 25A max Discharge (with regenerative): 1 single MP110kW cycle scaled for 16s6p

Table 21: Comparison between real and simplified battery pack

Graph 13 shows a typical CCCV charge profile.



Graph 13: Charge profile CCCV

Tables 22 shows the physical and electrical characteristics of the cells that form the battery pack.

Shape	Cylindrical	
Can material	Steel	
Diameter	21.55 mm	
Height	70.15 mm	
Weight	70 g	
Capacity	Typical	4200 mAh
		15.1 Wh
	minimum	4000 mAh
		14.4 Wh
Cell Voltage	Nominal	3.6 V
	Charge	4.2 V
	Discharge	2.5 V
Charge Current	Standard	4.2 A
	Maximum	12.6 A
		(70 °C cut-off)
Charge Time	Standard	1.5 hr
Discharge Current	Continuous	45 A
		(80 °C cut-off)
Temperature	Charge	0 °C to 60 °C
	Discharge	-40 °C to 60 °C
Energy Density	Volumetric	601 Wh/l
	Gravimetric	226 Wh/kg
Typical Impedance	AC (30% SOC)	7 mΩ
	DC (50% SOC)	16 mΩ

Table 22: Cell characteristics

3.3.3 Validation of pressure drop along coolers.

To determine the real value of the pressure drop along the coolers, the ΔP along the simplified battery pack obtained experimentally from Podium was compared with the ΔP calculated through a lumped parameter hydraulic model.

Lumped parameter hydraulic model

The Lumped parameter hydraulic model represents the simplified battery pack through the use of hydraulic resistances (Figure 47). In the hydraulic model, each cooler of the battery pack is replaced by its own hydraulic resistance. As in the real configuration, all the resistances are connected in parallel ensuring the hydraulic equivalence between the model and the simplified battery pack.

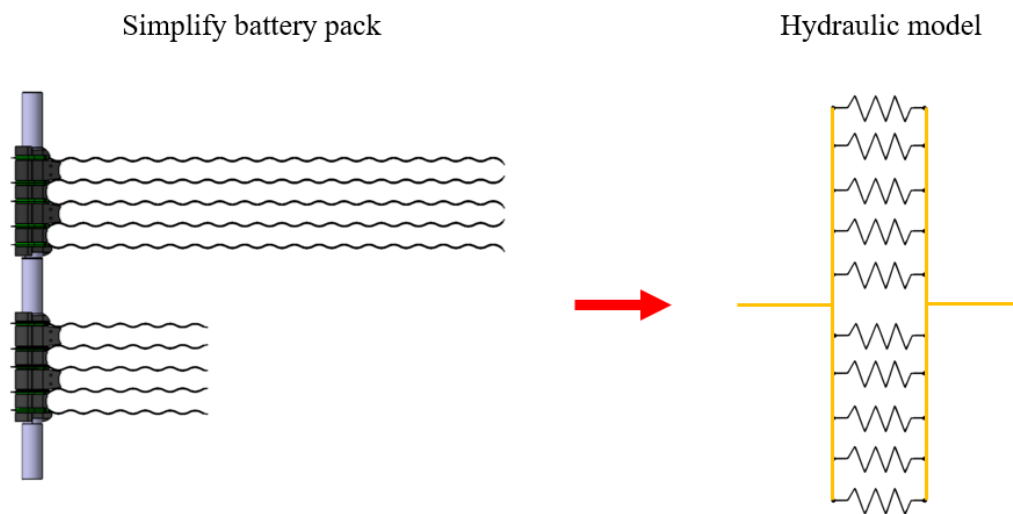


Figure 47: Equivalence between the simplified battery pack and the hydraulic model

The values of the hydraulic resistances of the coolers are evaluated using the equation 3.1.

$$\Delta P = RQ^2 \quad (3.1)$$

Table 23 represents the hydraulic resistance values of each cooler evaluated as a function of the pressure drops reported in table 19.

Cooler	Hydraulic resistance experimental [mbar]	Hydraulic resistance CFD [mbar]
Short 1.8	1.5328E+14	9.05616E+13
Short 1.9	1.3809E+14	8.02851E+13
Long 2.0	1.86261E+14	1.14326E+14
Long 2.5	1.19464E+14	7.64314E+13

Table 23: Comparison between the hydraulic resistances of the coolers

For the determination of the total pressure drop, it is necessary to calculate the equivalent hydraulic resistance of the lumped model.

The procedure is similar to the one used for the calculation of the equivalent resistances in electrical networks, however, since the relationship between the pressure drop and the fluid flow rate is approximately quadratic, the calculation of the equivalent resistances in the parallel configuration differs from the electrical case as shown by the equation 3.3.

The equations 3.2 and 3.3 show how to calculate the equivalent hydraulic resistances in the series and parallel configuration.

$$R_{eq} = R_1 + R_2 + \dots R_n \quad (3.2)$$

$$\frac{1}{\sqrt{R_{eq}}} = \frac{1}{\sqrt{R_1}} + \frac{1}{\sqrt{R_2}} + \dots \frac{1}{\sqrt{R_n}} \quad (3.3)$$

Table 24 shows the pressure drops calculated through the lumped parameter model considering as input values the ΔP of the coolers calculated through CFD (ΔP Hydraulic model 2) and supplied by the manufacturers (ΔP Hydraulic Model 1).

	Minimodule short	Minimodule long	Simplify battery pack
ΔP Hydraulic Model 1	224	219.6	221.8
ΔP Hydraulic model 2	131	138	134

Table 24: Comparison between the experimental and simulated pressure drops for the different configurations analysed

Minimodules

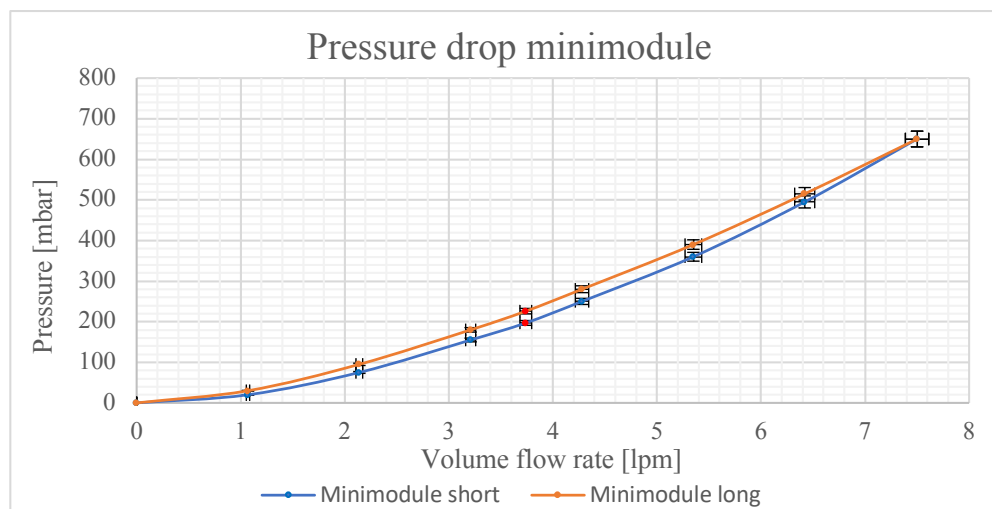
Validation tests

Validation of the pressure drop values obtained from the lumped parameter model was performed by measuring the ΔP along the simplified battery pack using the Podium test bench. The results of the experimental test for calculating the ΔP along the short and long minimodule are shown in table 25. The values in red indicate the pressure drop obtained at the flow rate used in the CFD simulations and in the experimental tests of the suppliers.

Mass flow [l/min]	Minimodule short ΔP [mbar]	Minimodule long ΔP [mbar]
0	0	0
1.07	20	30
2.14	75	95
3.21	155	180
3.74	195	224
4.28	250	280
5.35	360	390
6.42	495	515
7.5	650	650

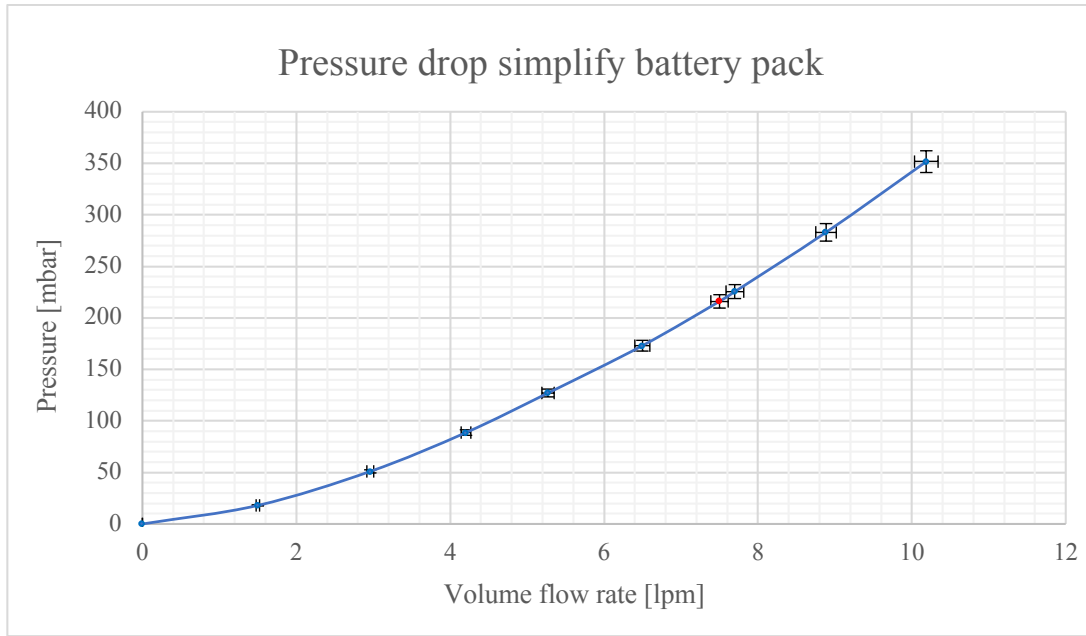
Table 25: pressure drop experimentally calculated along the long and short mini module as a function of the flow rate of the fluid

Graph 14 shows the pressure drop along the short minimodule (blue curve) and long minimodule (orange curve) as a function of the inlet flow rate. From the analysis of the graph it is possible to observe that the two experimental pressure drops are similar with a slightly greater pressure drop along the long minimodule.



Graph 14: Pressure drop along the long and short minimodules as a function of the coolant flow rate. The percent relative uncertainty of the pressure measurement is $\pm 3\%$. The percent relative uncertainty of the flow measurement is $\pm 1.5\%$

Graph 15 represents the pressure drop in mbar along the simplified battery pack as a function of the cooler flow rate. The graph shows that the pressure drop at the 7.5 lpm flow rate is equal to 216 mbar.



Graph 15: Pressure drop along the simplified battery pack as a function of the coolant flow rate. The percent relative uncertainty of the pressure measurement is $\pm 3\%$. The percent relative uncertainty of the flow measurement is $\pm 1.5\%$

Table 26 represents the pressure drop values for the different configurations analysed. ΔP Experimental refers to the ΔP values obtained experimentally through the Podium bench test. The ΔP calculated through the Hydraulic Model 1 uses ΔP values provided by the manufacturer of the coolers as model input. Finally, ΔP calculated with the Hydraulic Model 2 uses the values obtained from the fluid dynamics simulation as input of the lumped parameter model.

	Minimodule short	Minimodule long	Simplify battery pack
ΔP Experimental	195	224	216
ΔP Hydraulic Model 1	224	219.6	221.8
ΔP Hydraulic Model 2	131	138	134
Relative error 1	14.9	2	2.7
Relative error 2	32.8	38.4	38

Table 26: Comparison between experimental and simulated pressure drop values

Minimodules

The analysis of table 26 shows that the lumped parameter hydraulic model, which uses the ΔP values on each cooler provided by the manufacturer as input, provides results in line with those obtained from the experimental tests regarding the pressure drop along the long mini module and the simplify battery pack. The relative errors between the experimental results and the lumped model are 2% and 2.7%.

As for the pressure drop on the short mini module, both the ΔP s obtained from the CFD simulation and the experimental data provided by the manufacturers are not in line with the experimental results. In particular, the lumped parameter model overestimates the pressure drop on the short mini module by 14.9% if the ΔP s supplied by the manufacturers are used. Conversely, it underestimates the ΔP by 32.8% when using the values obtained through CFDs.

Since using the ΔP values provided by the manufacturers of the coolers, the error on the pressure drop of the simplified battery pack is 2.7%; and since in the final battery pack the number of long coolers exceeds that of short coolers by 3 times, it was decided to use the pressure drop values shown in table 27 as input for the protraction of the design activities.

Cooler	Pressure drop [mbar]
Short 1.8	238
Short 1.9	215
Long 2.0	290
Long 2.5	186

Table 27: Pressure drop values used for the subsequent design phases

3.3.4 Flow distribution

This subparagraph analyses the fluid dynamics simulations carried out to evaluate the coolant distribution inside the coolers of the simplified battery pack. Due to a lack of resources in terms of computational power, the simulations of the pack were carried out by replacing the coolers with interfaces to which the values of ΔP reported in table 27 have been assigned.

Short minimodule Grid Independence Study

For reasons of time, the Grid Independence Study was carried out only for the short module. The whole of the simplified battery pack was simulated in a “coarse mesh” configuration and the results were corrected considering the total error identified through the GIS.

The grid independent study relating to the short minimodule, shown in table 28, was conducted following the steps indicated by Roacher and described in subparagraph 3.2.5. The parameters under control are the $\Delta P/\rho$ value which is decisive for the evaluation of the pressure drop and the velocity values at the inlet of the coolers numbered from 1 to 5. These values are surface average and are used to determine the distribution of the flow rate in the coolers. The total inlet flow rate into the short mini module is 3.74 lpm.

Base size [mm]	Nº of prism layer	$\Delta P/\rho$ [Pa/kg/m ³]	V1 [m/s]	V2 [m/s]	V3 [m/s]	V4 [m/s]	V5 [m/s]
1	5	20.60217	0.189584	0.201491	0.201601	0.201531	0.189578
1.5	5	20.73725	0.190252	0.202203	0.202126	0.202137	0.190274
3	5	21.05184	0.191401	0.203146	0.203406	0.203267	0.191521
Relative error 1		0.6556591	0.35235	0.353366	0.260415	0.300698	0.367131
Relative error 2		1.5170285	0.603936	0.466363	0.633268	0.559027	0.655371
Extrapolated error		0.4958251	0.491741	1.101155	0.181412	0.348968	0.465905
Richardson extrapolation		20.500523	0.188656	0.199296	0.201236	0.20083	0.188699
GCI ₁₂		0.6167235	0.611669	1.361452	0.226354	0.434692	0.579681
GCI ₂₃		1.4269415	1.048413	1.79681	0.55044	0.808135	1.034796
p		2.7679086	1.775722	0.919976	2.917907	2.04005	1.909262
Solution convergence		0.9934861	0.996489	0.996479	0.997403	0.997002	0.996342
Maximum error		2.618853	1.434005	1.894973	1.066864	1.198833	1.47355
Pressure drop [mbar]		207.6703					

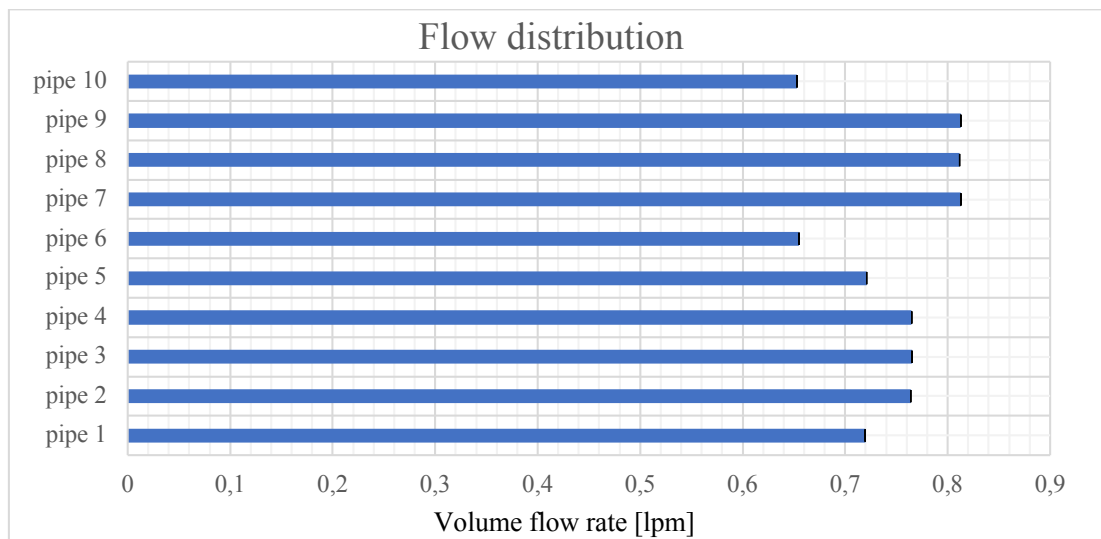
Table 28: Short minimodule Grid Independence Study

Minimodules

As it is not possible to directly validate the flow rate values within each cooler, only the ΔP value along the short minimodule equal to 207.7 mbar is used for the validation of the fluid dynamics simulation. This value is compared with the result of the experimental test shown in table 26. The relative error between the two pressure drops is equal to 6.1%.

Simplify Battery Pack simulation results

Graph 16 shows the coolant flow rate that passes inside each cooler of the simplified battery pack obtained through fluid dynamics simulation. Pipes from 1 to 5 are related to the short minimodule while those from 6 to 10 belong to the long minimodule.



Graph 16: Coolant flow rate in each simplified battery pack cooler

It is interesting to note how the coolant flow rate that flows inside the central and side coolers is balanced between the two mini modules. This guarantees homogeneous cooling to all cells of the simplified battery pack.

It should be noted that, in the short minimodule, the ratio between the flow rate in the central coolers and that in the side coolers is greater than the long minimodule one. This depends on the diameters of the calibrated holes. In the short mini module, the ratio between the diameters of the calibrated holes is 1.06 while in the long mini module it is 1.25.

3.3.5 Conclusions

This chapter analyses the reason why the pressure drop along the coolers obtained through fluid dynamics simulations is lower than that calculated experimentally.

Table 29 shows the values of the pressure drop, experimental and simulated by CFD, along the entire simplified battery pack. The fourth column of table 29 represents the gain between the two curves that is the ratio between the values of the pressure drop obtained experimentally and that calculated by CFD.

mass flow rate [lpm]	ΔP experimental [mbar]	ΔP CFD [mbar]	Gain
0	0	0	---
1.5	18	8	2.25
2.298124	36	16.4106	2.183215
2.9615	51	27.0471	2.077436
4.205331	88.7	54.702	1.621049
5.271471	127.1	85.092	1.493258
6.497532	173	128.651	1.344905
7.699901	225.5	180.6179	1.248453
8.884501	283	240.1823	1.206905
10.18756	351.6	315.5495	1.114125

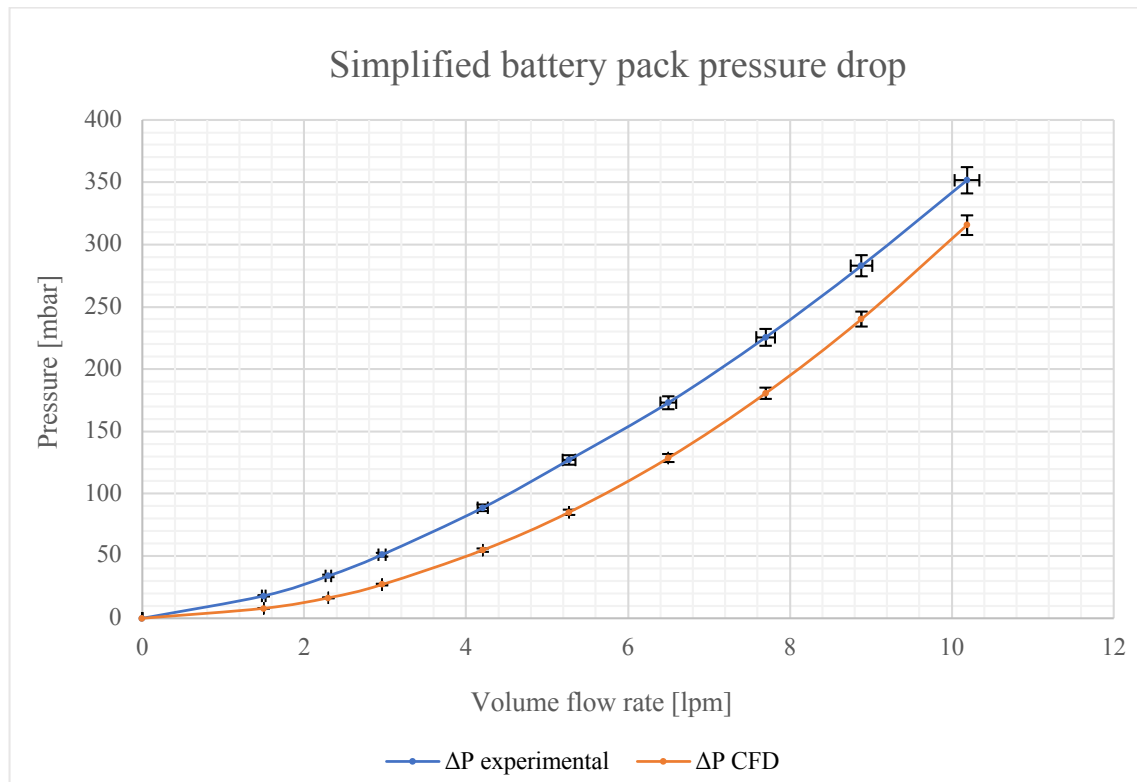
Table 29: Comparison between the pressure drop values along the simplified battery pack obtained experimentally and through CFD simulation

Graph 17 shows the experimental and simulated pressure drops along the simplified battery pack as a function of the coolant flow rate. The experimental value of the pressure drop is higher than that simulated by CFD simulation. This difference, however, is not constant but decreases as the coolant flow rate increases, passing the gain value from 2.25 to 1.11.

This behaviour depends on the nature of the coolers. Being flexible and deformable objects, the channels in which the coolant flows do not have fixed dimensions. They expand as the flow rate increases, leading to a decrease in the hydraulic resistance which results in a decrease in gain and, proportionally, in the pressure drop.

Minimodules

The expansion of the coolers with increasing flow makes the real geometry more similar to the ideal one used in CFD. Any negative effects produced by wrinkles in the coolers due to deformation following assembly are reduced as pressure increases. To reduce this unwanted effect even at lower flow rates, the coolers used to cool the complete battery pack are performed before assembly.



Graph 17: Pressure drop along simplified battery pack as a function of the coolant volume flow rate. The blue curve represents the values obtained experimentally. The red curve represents the values obtained by CFD simulation. The percent relative uncertainty of the pressure measurement is $\pm 3\%$. The percent relative uncertainty of the flow measurement is $\pm 1.5\%$. The percent relative uncertainty of the CFD pressure drop simulation is $\pm 2.5\%$

3.3.6 Simplify battery pack thermal analysis

The study of the simplified battery pack cooling was carried out through 3D thermo-fluid dynamics simulations and the creation of a 1D model with lumped parameters in order to ensure the achievement of the project target which consists of a maximum cell temperature not exceeding 35 °C during a charge-discharge cycle at constant average output power. The results obtained were validated through bench tests.

3.3.6.1 Computational Thermal Fluid Dynamics simulation

Physical domain

The purpose of the simulation is to evaluate the temperature of the cells during a charge-discharge cycle characterized by the generation of constant electrical power. The study domain is the same used for the simulation of the short cooler having 1.8 mm calibrated holes with the addition of 6 half cylinders that represent the volume of the cells affected by the cooling.

Thermophysical properties

The coolant is the same used in fluid dynamics simulations; its properties are therefore reported in table 11.

Table 30 shows the physical properties attributed to the cells and coolers.

Properties	Value
Cell density [kg/m ³]	2698.9
Cell specific heat [J/kg/K]	900
Cell thermal conductivity [W/m/K]	{2.5 2.5 22}
Cooler density [kg/m ³]	900
Cooler specific heat [J/kg/K]	1800
Cooler thermal conductivity [W/m/K]	0.22

Table 30: Physical properties of cells and coolers

Minimodules

Computational domain

The thermo-fluid dynamics simulation was carried out by adding to the short cooler with 1.8 mm calibrated holes 6 half cylinders representing the volume of the cells cooled by the cooler.

The analysed configuration is that of the first cooler of the short minimodule. This cooler only cools half of the cells that make up the first row.

Boundary conditions

The study domain has the same boundaries defined in subparagraph 3.2.3 with the addition of the six solid domains representing the cells. The software automatically generates 6 boundaries in the interface areas between the cells and the cooler.

It is not possible, in terms of computational resources, to simulate the entire thickness of the cooler; a contact resistance was set at the interface between the cells and the cooler to simulate the thermal resistance due to the cooler wall.

Volume conditions

Heat Source: each cell is considered as a constant heat source equal to 2.8 W. Since the simulation considers half of each cell the set value is 1.4 W as absolute power.

Physics

The models and physics used for the simulation are the same already discussed in subparagraph 3.2.3.

Automated 2D mesh

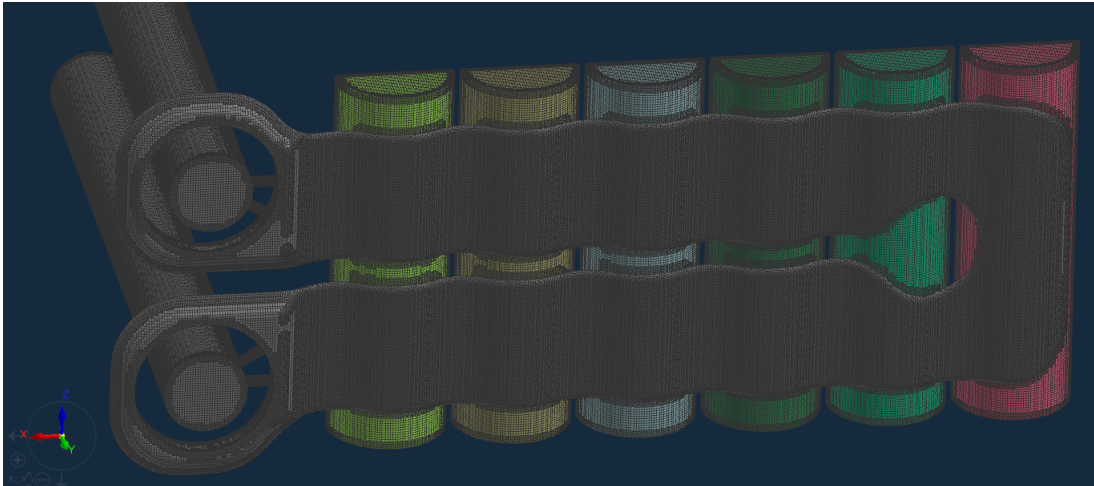


Figure 48: Representation of the study domain mesh

In order to optimize the mesh and facilitate the convergence of residuals, the following custom controls have been implemented in addition to the others already described in chapter 3.2.3:

- **Surface control:** The surface controls are implemented by setting the refinement level with respect to the base size value of the simulation. Each level has a base size value equal to half the value of the previous level. Table 31 shows the maximum and minimum levels of the boundary used to create the mesh.

Boundary	Minimum	Maximum
Cell	Level 2	Level 1

Table 31: Surface control refinement levels

Grid independence study

Due to the high computational cost, it was not possible to carry out a Grid Independence Study of the simulation.

Minimodules

Simulation results

The discussion in this section is divided into two parts; at the beginning the temperature distribution of the cells is analysed in more detail (Figure 50). Subsequently, the temperature trend of the coolant inside the cooler is analysed (figure 51 and graph 18).

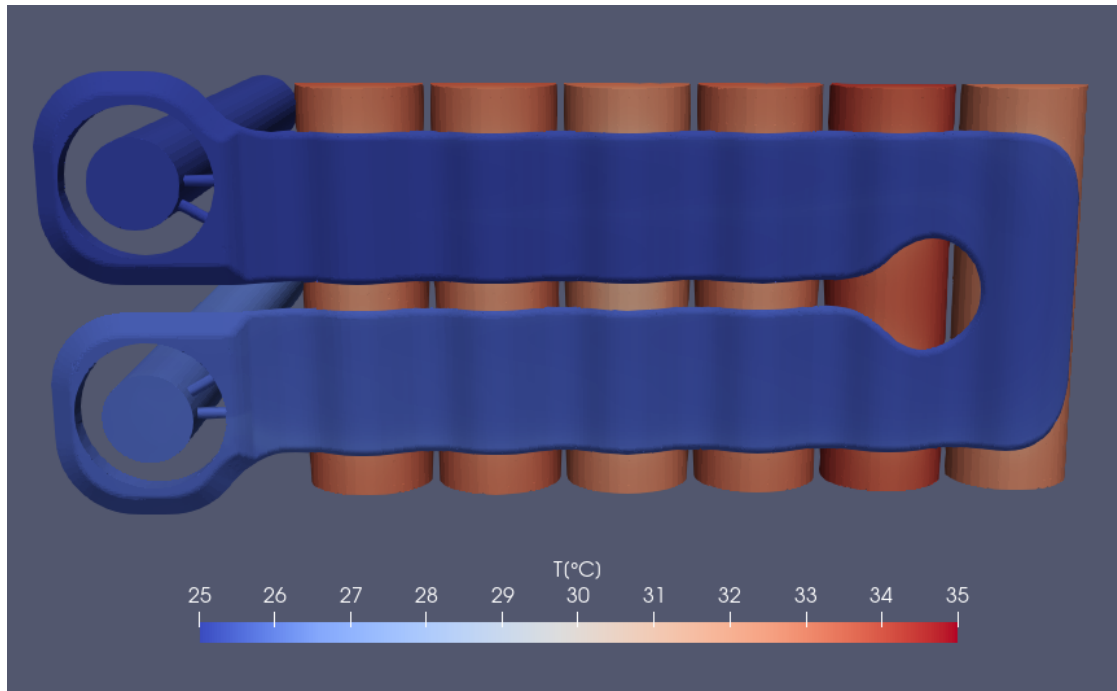


Figure 49: Representation of the temperature contour of the study domain

Figure 49 shows the result of the thermo-fluid dynamics simulation on the totality of the study domain. The quantity represented is the temperature in degrees Celsius.

Figure 50 shows the cell temperature in degrees Celsius obtained from the simulation. It is interesting to note that the temperature distribution is consistent with the physics of cooling; the first three cells starting from the left, show a decreasing temperature as the distance from the calibrated holes increases. This behaviour is attributable to the fact that the flow, just out of the holes, does not fill the channel homogeneously, reducing the heat exchange.

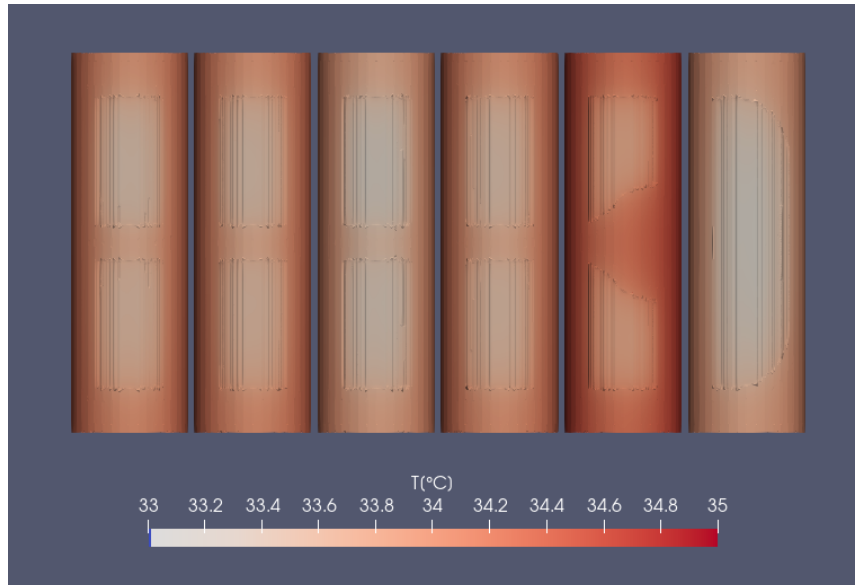


Figure 50: Temperature contour of the cells

Cell number 5 is the hottest one having a maximum temperature of about 35 °C. This is due to the smaller heat exchange surface with the cooler due to the latter's geometry. Cell 4 has a slightly higher average temperature than cell 3; this behaviour probably depends on the modification of the shape of the channel downstream of the cell which minimally affects its cooling. Cell 6 is the coldest one having the largest heat exchange surface with the cooler. By analysing the temperature distribution between the cells, it is evident that the cooler allows for a uniform cooling. The maximum temperature difference between the cells obtained from the simulation does not exceed 1.5 °C.

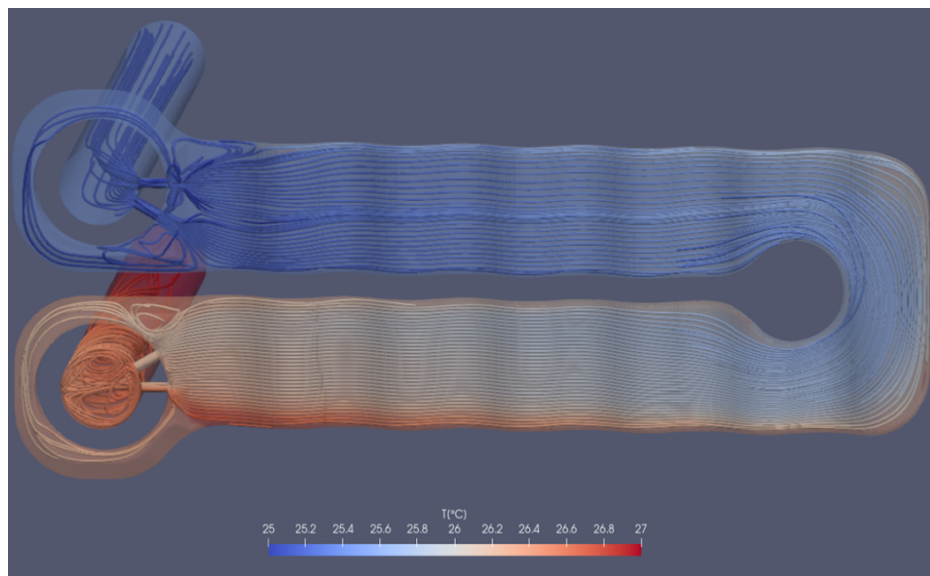
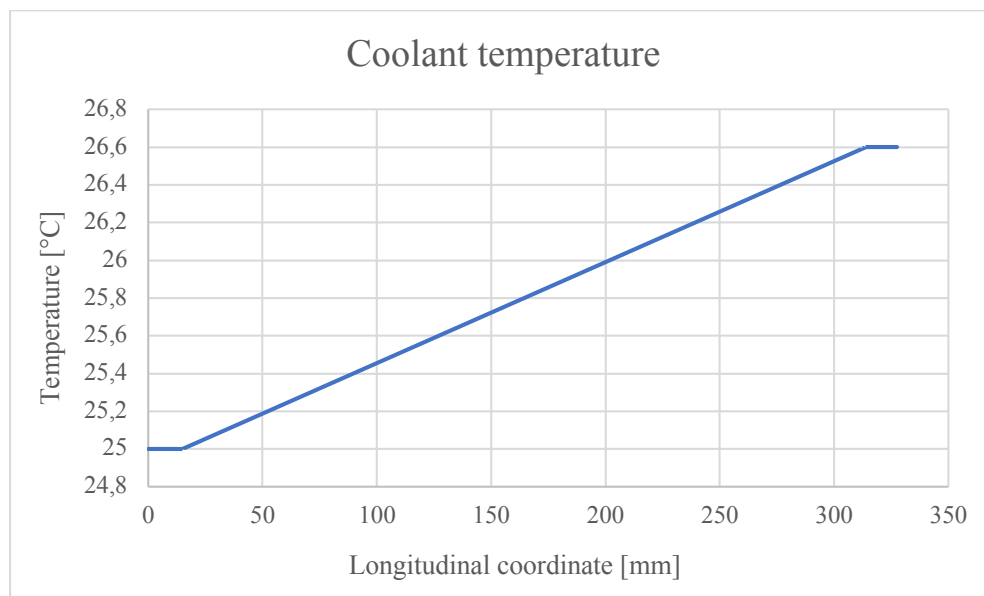


Figure 51: Temperature contour of the flow inside the cooler displayed by streamlines

Minimodules

Figure 51 shows the temperature of the flow that flows inside the cooler through the representation of the streamlines. This type of representation is interesting because it allows to capture any non-uniformity or turbulence of the flow that can compromise the cooling. It is evident that the flow is laminar throughout the domain; the only region to be considered is the one downstream of the inlet holes and upstream of the outlet holes where there are small eddies. This is the reason why the cell placed in that position is the second hottest in the lot. The figure shows that on the outside of the duct the temperature is on average higher. This phenomenon depends on the fact that in that area the geometry of the cooler hinders the passage of the fluid which causes an increase in temperature.



Graph 18: Coolant temperature trend as a function of the longitudinal coordinate

Graph 18 shows the trend of the average temperature of the coolant along the channel. The inlet temperature and the ambient temperature are simulation input parameters set at 25 °C. The graph shows a linear trend of the coolant temperature which increase of about 1.6 °C between inlet and outlet.

3.3.6.2 Simscape 1D thermal model

This section analyses the lumped-parameter 1D model created to predict the maximum cell temperature during a charge-discharge cycle at constant generated average power. The model is made with Simscape software; the results are compared with those obtained through thermo-fluid dynamics simulation and validated by means of bench tests.

Physical parameters

Thermal power generated [W]	16.8
Cell specific heat [J / kg / K]	1000
Cell mass [kg]	0.42816
Heat exchange surface [m ²]	6.055 e-3
Thickness [m]	10.655 e-3
Cell thermal conductivity [W / (m * K)]	2.5
Cooler thermal mass [kg]	7.63e-4
Cooler specific heat [J / kg / K]	1800
Cooler thickness [m]	7 e-5
Cooler thermal conductivity [W / (m * K)]	0.22
Inlet water temperature	25 °C
Room temperature	20 °C
Air density [kg/m ³]	1013
Air dynamic viscosity [Pa*s]	0.001183
Air kinematic viscosity [m ² /s]	1.1662E-06
Air specific heat [J/kg/K]	4087
Air thermal conductivity [W/m/K]	0.52

Table 32: Physical parameters of the lumped parameter model

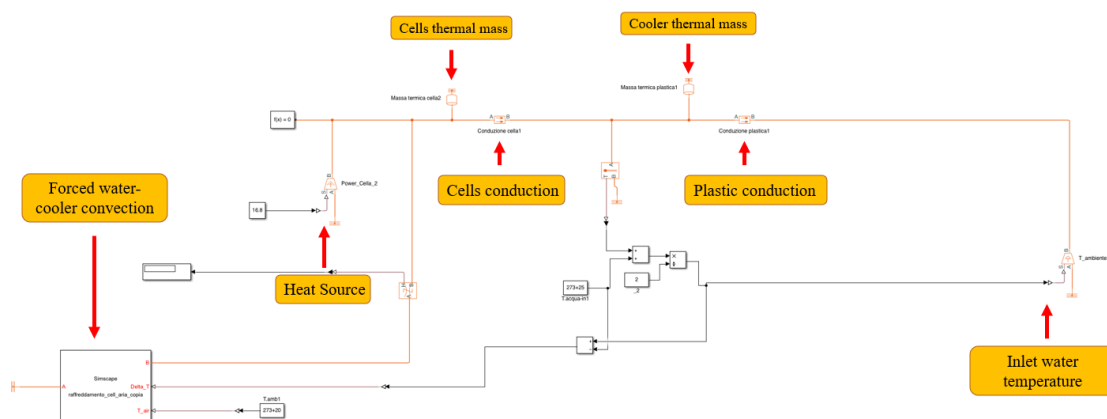
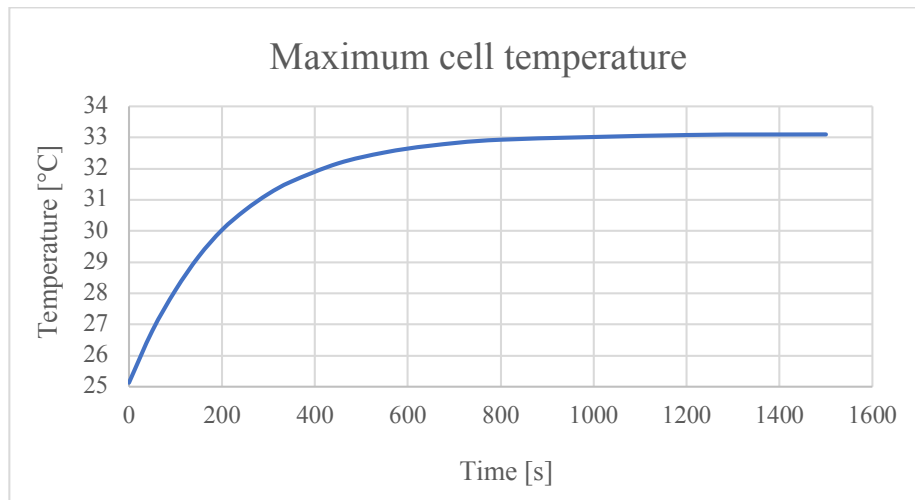


Figure 52: Lumped parameter model of the battery pack cooling system

Simulation Results



Graph 19: Maximum cell temperature simulated through the lumped parameter model

Graph 19 represents the simulation result. At steady state the maximum temperature reached by the cells is about 33 °C. The validation of the thermal model is analysed in the next subparagraph.

3.3.6.3 Validation of thermal simulations

Overview

The validation of the thermo-fluid dynamics simulation and of the lumped parameter 1D model is carried out through a bench test which involves a cycle of 10 s of charge followed by 10 s of discharge; both the charge and discharge cycles are performed at 1C.

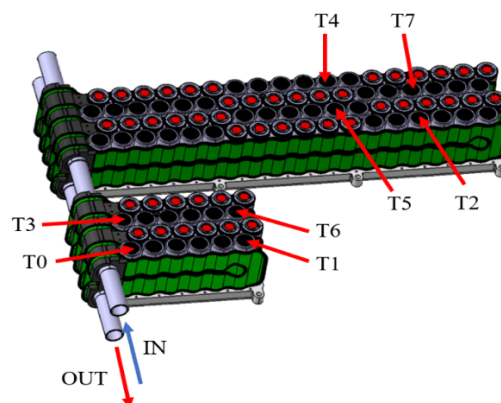
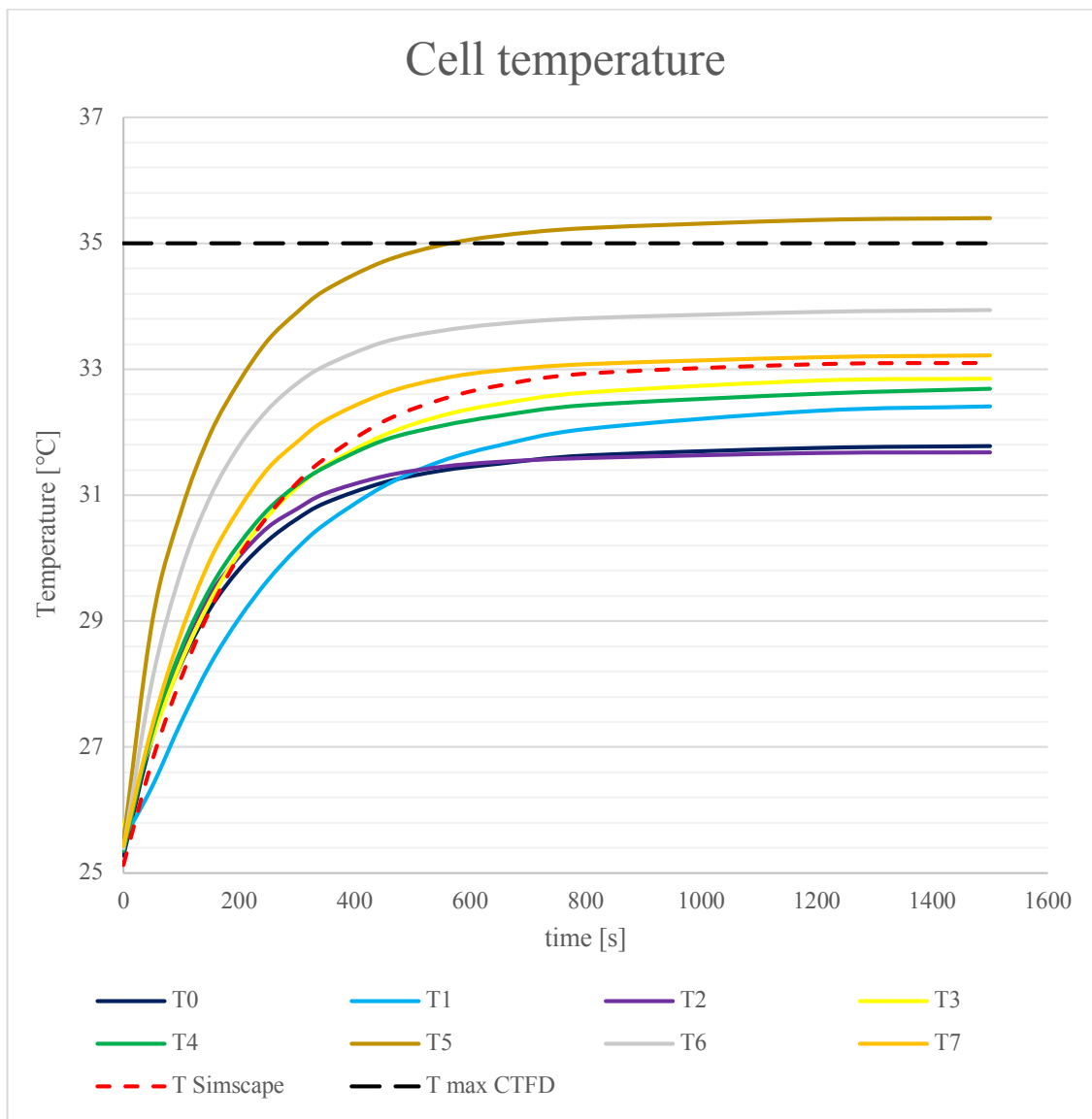


Figure 53: Position of the NTC sensors used for temperature measurement

Figure 53 represents the positions of the cells of the simplified battery pack which have been equipped with NTC thermistors for measuring the temperature. The thermistors are positioned on the negative poles of the cells (black poles in figure 53) since the positive pole is not representative of the cell temperature. The blue and red arrows indicate the inlet and outlet direction of the coolant.

Results



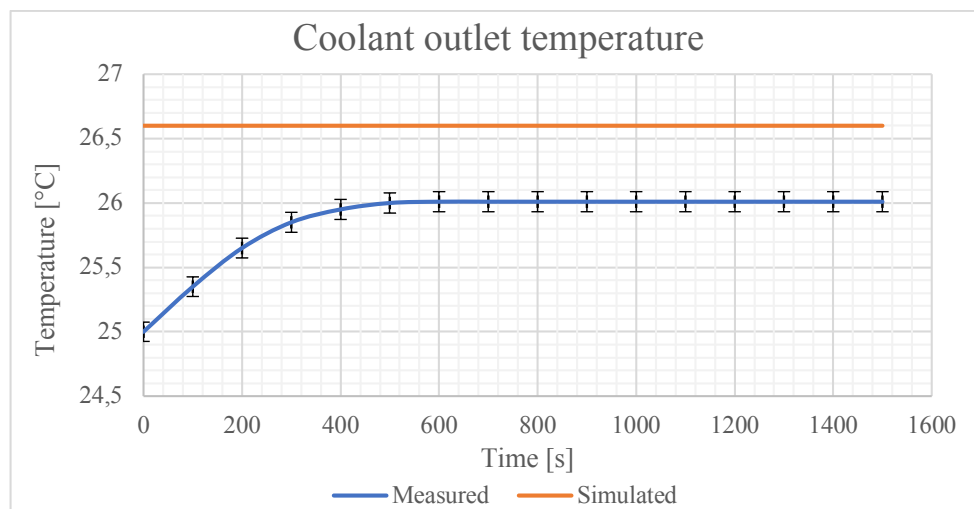
Graph 20: Comparison between maximum cell temperatures measured by NTC sensors and simulated

Graph 20 compares the results of the experimental test with those obtained from the thermo-fluid dynamics simulation and from the 1D lumped parameter model. The graph shows that the lumped parameter model provides a maximum cell temperature

Minimodules

of 33.1 °C which falls within the range [31.68, 33.94] of the temperature values obtained from the measurement. The T5 sensor detects a temperature of 35.4 °C; this value is an outcast since it refers to the busbar temperature. This phenomenon is due to an imperfect positioning of the NTC thermistor.

The black dashed line represents the maximum cell temperature obtained from the thermo-fluid dynamics simulation. The calculated value of 35 °C leaves the temperature range measured during the test; this happens because the simulation considers the system as adiabatic neglecting the heat exchange that occurs between the cells and the air. During the test phase, the cells of the battery pack also exchange heat with the surrounding air, leading to a maximum temperature lower than that obtained from the thermo-fluid dynamics simulation.



Graph 21: Comparison between the measured and simulated coolant outlet temperature. The percent relative uncertainty of the temperature measurement is $\pm 0.3\%$

Graph 21 represents the measured and simulated temperature values of the coolant at the outlet of the simplified battery pack. The orange line represents the temperature obtained through the thermo-fluid dynamics simulation while the blue curve represents the experimentally measured temperature. The relative error between the temperature values is 6%. Since the thermo-fluid dynamics simulation neglects the heat exchange between the cells and the air, on average, the simulated temperature of the cells is higher than that measured experimentally. For this reason, the amount of heat exchanged between the cells and the coolant will be greater in the case of the simulation. This results in an increase in the coolant temperature rather than the experimentally measured value.

3.4 Full battery pack

This paragraph describes the layout of the complete system consisting of the Battery Pack plus the inlet and outlet ducts. The discussion is developed starting from a general overview and then dealing in detail with the hydraulics of the ducts. Subsequently, the system is analysed to define the correct distribution of the flow rates and evaluate the global pressure drop.

3.4.1 Overview

Since the design of the complete battery pack and the cooling system is strictly confidential material, it is not possible to insert images of the real geometry. The scheme in figure 54 represents the complete battery pack layout.

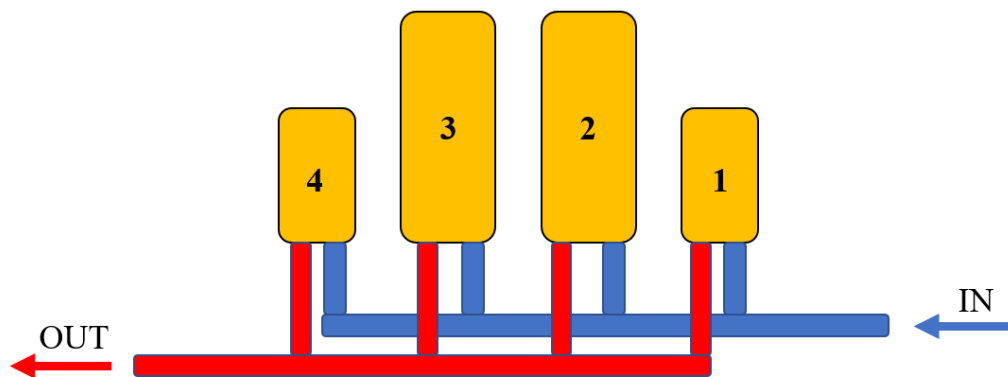


Figure 54: Complete battery pack scheme

The battery pack consists of 4 modules in parallel arranged as in figure 54. The battery pack has a symmetrical layout since modules 2-3 and 1- 4 are identical. The cooling system includes 2 duct systems, one at the inlet and one at the outlet (red and blue in figure 54) that couple with the coolers of each module.

Full battery pack

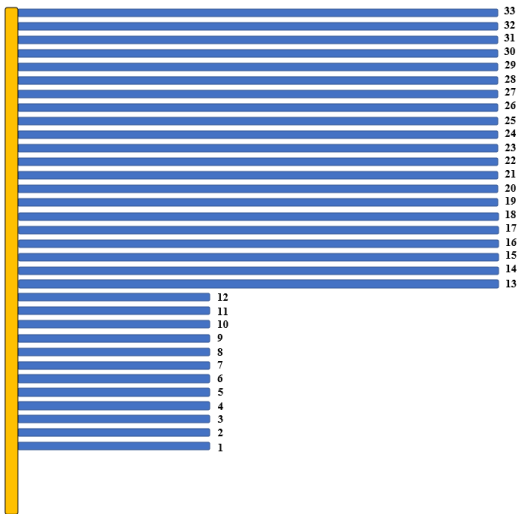


Figure 55: Scheme of a central module of the battery pack

Figure 55 schematically represents the layout of the coolers inside modules 2 and 3. In these, the 33 coolers have two different lengths. The first 12 are short coolers, while the last 21 are long coolers. Cooler number 1 and cooler number 33 have a diameter of the calibrated holes equal to 1.8 mm and 2.0 mm respectively. The remaining short coolers have a diameter of the calibrated holes equal to 1.9 mm while the long coolers have a diameter of calibrated holes equal to 2.5 mm.

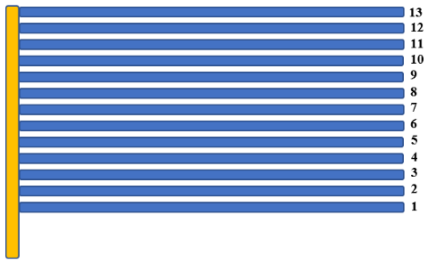


Figure 56: Scheme of a side module of the battery pack

Figure 56 schematically represents the layout of the coolers inside modules 1 and 4. These are the external modules of the battery pack and consist of 13 medium coolers. In this case the coolers 1 and 13 have a diameter of the calibrated holes equal to 2.3 mm while for the central coolers the diameter is 2.5 mm.

3.4.2 Inlet piping

Figure 57 represents the layout of the inlet ducts. Each branch of the ducts is represented by the hydraulic resistance value calculated through the equation 3.1. The ΔP values have been obtained through CFD simulations in which the inlet flow rate is equal to 70 lpm. Unfortunately, since the design of the ducts is an industrial secret, it is not possible to attach the contours of the simulations to the discussion.

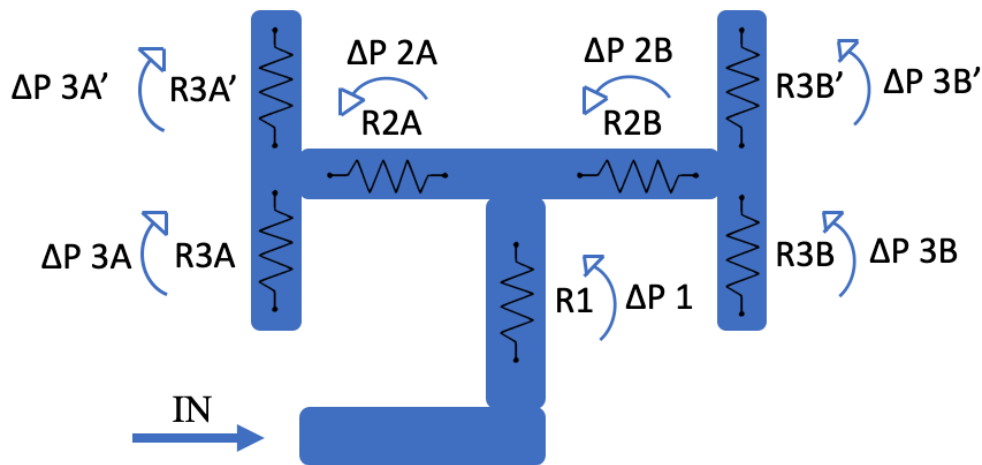


Figure 57: Scheme of the inlet ducts represented by hydraulic resistances

Table 33 shows the values of the hydraulic resistances obtained from the fluid dynamics simulation.

	Resistance	ΔP [mbar]
R1	1.9836e+07	27
R2A	2.1577e+06	13
R2B	2.1083e+06	12
R3A	3.1823e+10	26
R3A'	2.9522e+10	23.7
R3B	3.3715e+10	32.4
R3B'	3.5217e+10	30.3

Table 33: Pressure drop and hydraulic resistance in each branch of the inlet ducts

3.4.3 Outlet piping

Figure 58 shows the layout of the outlet ducts represented through hydraulic resistances. As in the case of the inlet ducts, the values of the hydraulic resistances are calculated through a CFD simulation with a global flow rate of 70 lpm. The inlet flow values on each branch are equal to the outlet flow values from the corresponding branch of the inlet ducts.

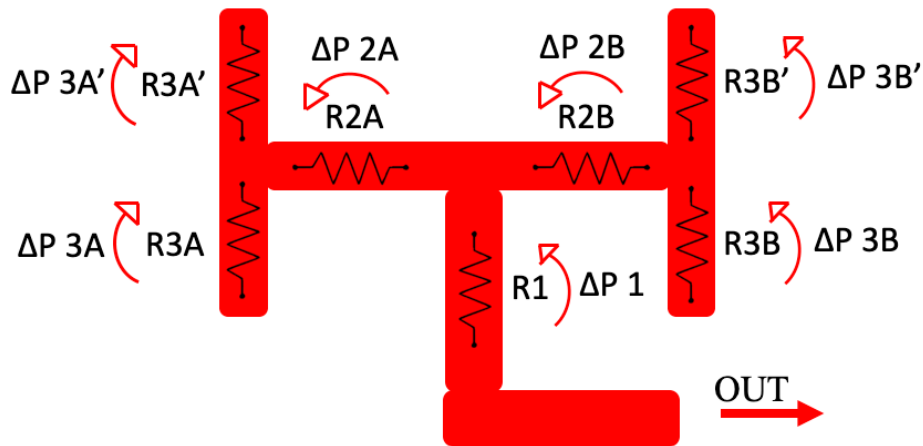


Figure 58: Scheme of the outlet ducts represented by hydraulic resistances

Table 34 represents the values of the hydraulic resistances obtained from the simulation. As can be seen by comparing table 33 with table 34, the values of the hydraulic resistances of the outlet ducts are greater than those of the inlet ducts. This behaviour depends on the fact that the hydraulic losses concentrated in the points where two different flows meet are greater than those in the points where the flow divides.

	Resistance	ΔP [mbar]
R4A'	9.0062e+10	72.3
R4A	8.0783e+10	66
R4B	6.1498e+10	59.1
R4B'	7.7025e+10	65.9
R5A	3.3382e+06	19
R5B	3.7510e+06	22.6
R6	1.9836e+07	27

Table 34: Pressure drop and hydraulic resistance in each branch of the outlet ducts

3.4.4 Full system hydraulic balance

Although the battery pack modules have a symmetrical configuration, the external stacks are different from the central ones. For this reason, it is necessary that the flow of the cooling fluid inside the modules is properly balanced. A lumped parameter model was used to balance the battery pack using the hydraulic resistances obtained through CFD simulation.

Figure 59 represents the hydraulic diagram of the battery pack in terms of hydraulic resistances. r_1 , r_2 , r_3 , r_4 are the equivalent hydraulic resistance values of the battery pack modules. Being symmetrical $r_2 = r_3$ and $r_1 = r_4$.

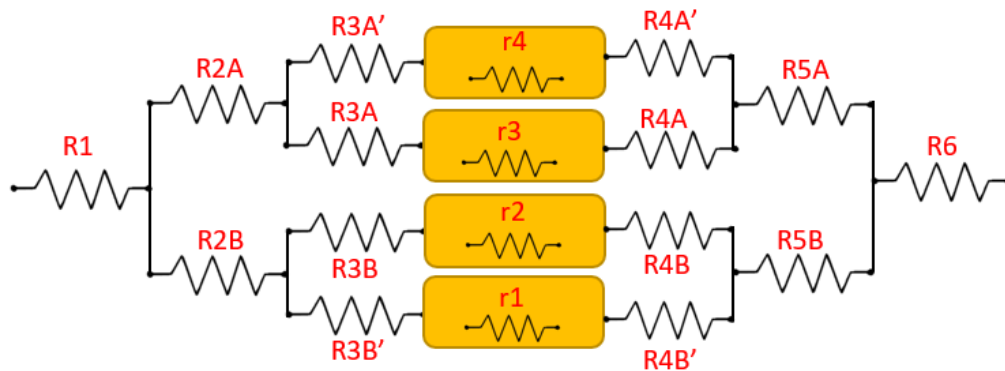


Figure 59: Representation of the complete battery pack through hydraulic resistances

To perform the hydraulic balancing of the battery pack, it is necessary to calculate the equivalent hydraulic resistances of the entire system. The procedure and the formulas used are the same as described in subparagraph 3.3.3.

Cooler	Pressure drop [mbar]	Resistance
Short 1.8	238	1.5328E+14
Short 1.9	215	1.3809E+14
Medium 2.3	250	1.6259e+14
Medium 2.5	200	1.3007e+14
Long 2.0	290	1.8861e+14
Long 2.5	186	1.2097e+14

Table 35: Pressure drop and hydraulic resistance values for each type of cooler

Full battery pack

Table 35 shows the values of the hydraulic resistances for each type of cooler used as input of the lumped parameter model.

Figure 60 shows the simplification process of the equivalent hydraulic model used for balancing the complete system.

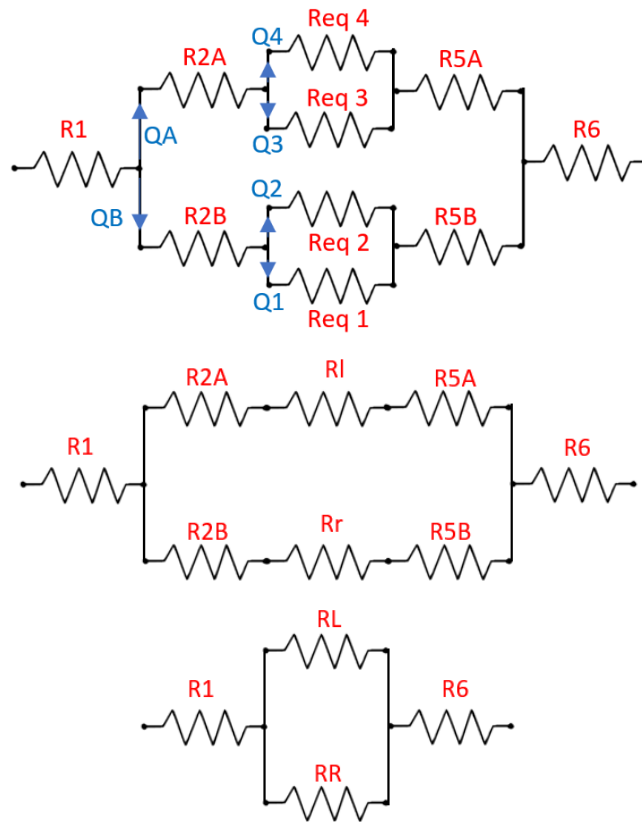


Figure 60: Simplification of the lumped parameter hydraulic model through the calculation of equivalent hydraulic resistances

Table 32 shows the values of the equivalent hydraulic resistances calculated with the formulas 3.2 and 3.3.

Resistance name	Value
$r1 = r4$	$1.2081e+11$
$r2 = r3$	$1.2325e+11$
Req 1	$9.0753e+11$
Req 2	$2.1846e+11$
Req 3	$2.3585e+11$
Req 4	$9.1487e+11$
Rl	$1.0375e+11$
Rr	$9.8318e+10$
RL	$1.0376e+11$
RR	$9.8324e+10$

Table 36: Values of equivalent hydraulic resistances

Since the value of the inlet and outlet flow is known in the hydraulic system but the distribution of the flow inside the ducts is not known a priori, it was decided to calculate the unknown flow using the Hardy Cross Method.

3.4.4.1 Hardy Cross Method

The method chosen, through successive iterations, allows to determine the flow rates in each branch of the duct knowing the relationship that links the flow to the pressure drop (eq. 3.1).

The method uses an initial condition that satisfies the continuity of the coolant flow in each junction of the network and, subsequently, balances the flow to achieve potential continuity within each system loop.

For each loop, it is necessary to determine the total head losses given by the sum of the head losses that make up the loop. Head losses are positive if counter clockwise, negative if clockwise.

The change in the flow is given by the ratio between total head loss in the loop $\sum rQ^n$ e $\sum nrQ^{n-1}$.

In this case, $n = 2$ is considered; r is the value of the hydraulic resistance obtained by CFD.

The initial condition is iteratively updated considering the flow modification value calculated at each previous iteration.

The process repeats iteratively until an error of zero is reached.

Volume flow rate	Value
QA [lpm]	34.53
QB [lpm]	35.47
Q4 [lpm]	11.63
Q3 [lpm]	22.9
Q2 [lpm]	23.53
Q1 [lpm]	11.94
Q3/Q4	1.969
Q2/Q1	1.969

Table 37: Volume flow rate of coolant in each branch of the system

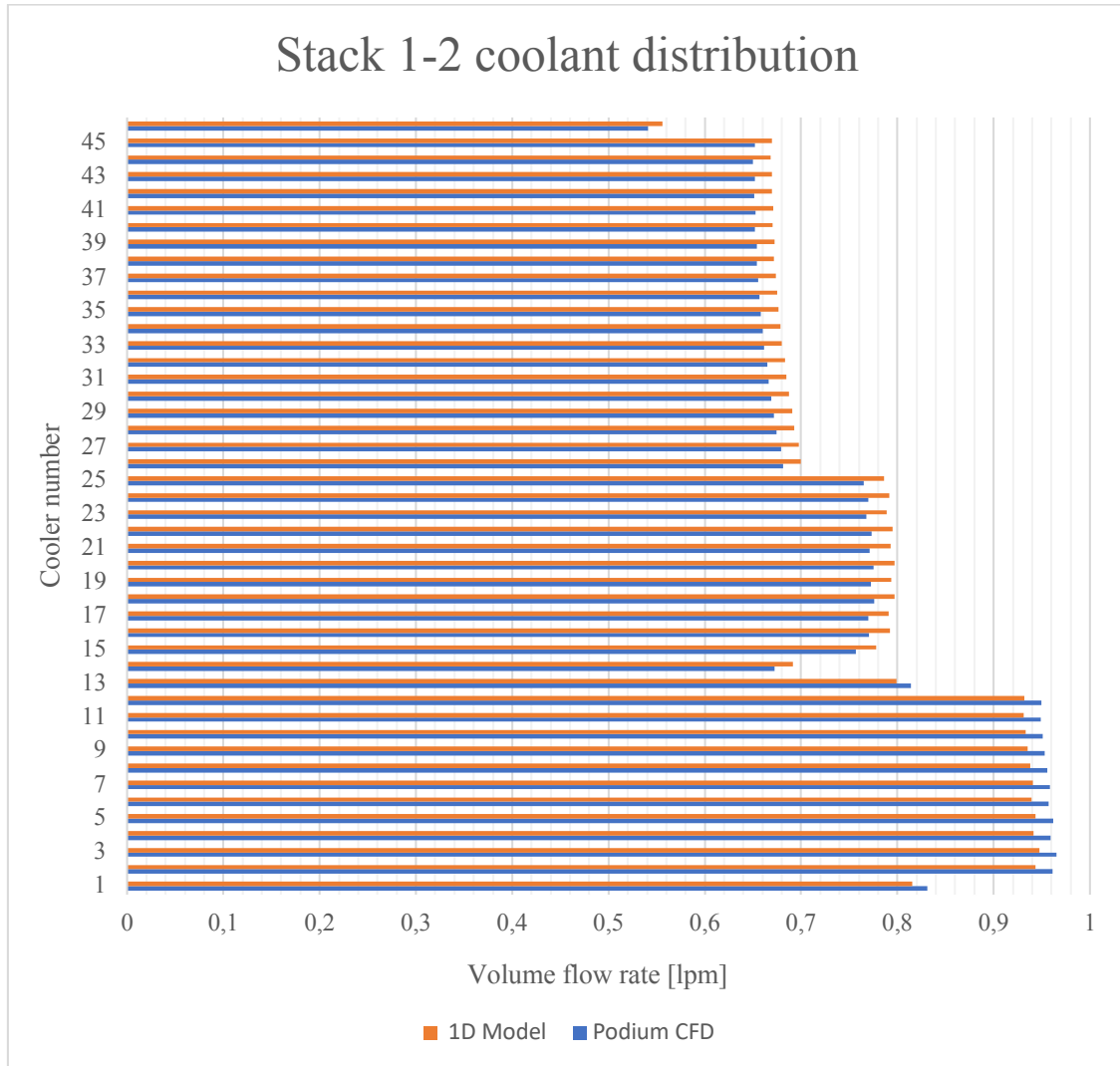
Full battery pack

Table 37 shows the values of the flow rates evaluated in each branch of the ducts through the Hardy Cross Method. It is interesting to note how, due to a small asymmetry in the first part of the inlet ducts, the coolant flow rate in the right part of the battery pack is slightly lower than that in the left part; 34.53 lpm and 35.47 lpm. The values of the Q_3/Q_4 and Q_2/Q_1 ratios highlight an imbalance between the flow of coolant that enters the central modules compared to that of the side modules. A preliminary analysis shows that the optimal ratio between the values of the two flows is about 2.5.

For this reason, it is necessary to insert a necking inside the piping system to properly balance the system.

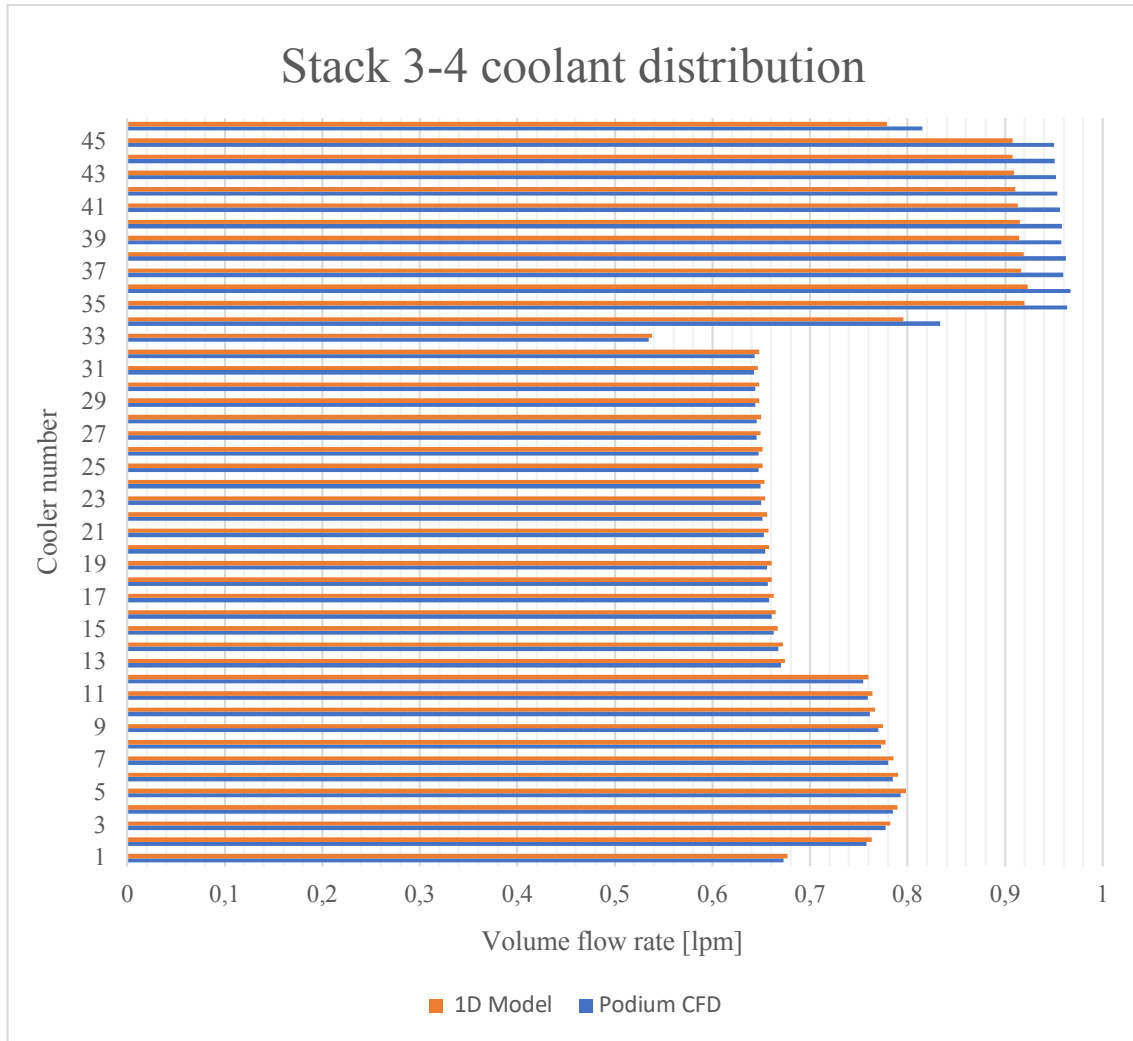
Since the operating range of the coolant flow rate inside the battery pack is between 50 lpm and 70 lpm, the balancing of the flow rate at the extremes of the range was carried out.

3.4.4.2 Coolant volume flow rate at 70 lpm



Graph 22: Volume flow rate distribution of coolant in each cooler of stacks 1 and 2. The orange bars represent the distribution obtained before hydraulic balancing by 1D model while the blue bars by CFD simulation

Graph 22 represents the coolant volume flow rate for each cooler of modules 1 and 2 of the battery pack. The blue bars represent the flow rates obtained through the CFD simulation while the orange bars represent the flow rates obtained through the lumped parameters model. The coolers ranging from number 1 to 13 relate to the side module 1 while the rest (14-46) relate to the central module 2.



Graph 23: Volume flow rate distribution of coolant in each cooler of stacks 3 and 4. The orange bars represent the distribution obtained, before hydraulic balancing, by 1D model while the blue bars by CFD simulation

Graph 23, like graph 22, represents the coolant flow rate for each cooler of modules 3 and 4 of the battery pack. In this case the coolers from 1 to 33 belong to the central module 3 while the coolers from 34 to 46 belong to the side module 4.

The coolant flow imbalance between the lateral and central stacks predicted in table 37 ($Q3/Q4$ and $Q2/Q1 \neq 2.5$) is also highlighted by graphs 22 and 23 which show a clear imbalance between the flow rate that passes inside the side stacks and the one that passes into the long coolers of the middle stacks. For this reason, it is necessary to carry out a balancing.

The analysis of graphs 22 and 23 shows how the 1D model, compared with the Podium CFD, is able to correctly predict the distribution of flow within the stacks. For this reason, the 1D lumped parameter model is used to realize the hydraulic balancing of the system.

To carry out the balancing, a necking was made to be inserted downstream of the side stacks to increase the hydraulic resistance of the circuit and reduce the flow inside them for the benefit of the central stacks.

To calculate the value of the concentrated loss and design the necking, equation 3.4 was used where V is the flow velocity upstream of the necking.

$$h_L = K \frac{V^2}{2g} \quad (3.4)$$

The value of K is calculated through equation 3.5.

$$K = K_1 * K_2 \quad (3.5)$$

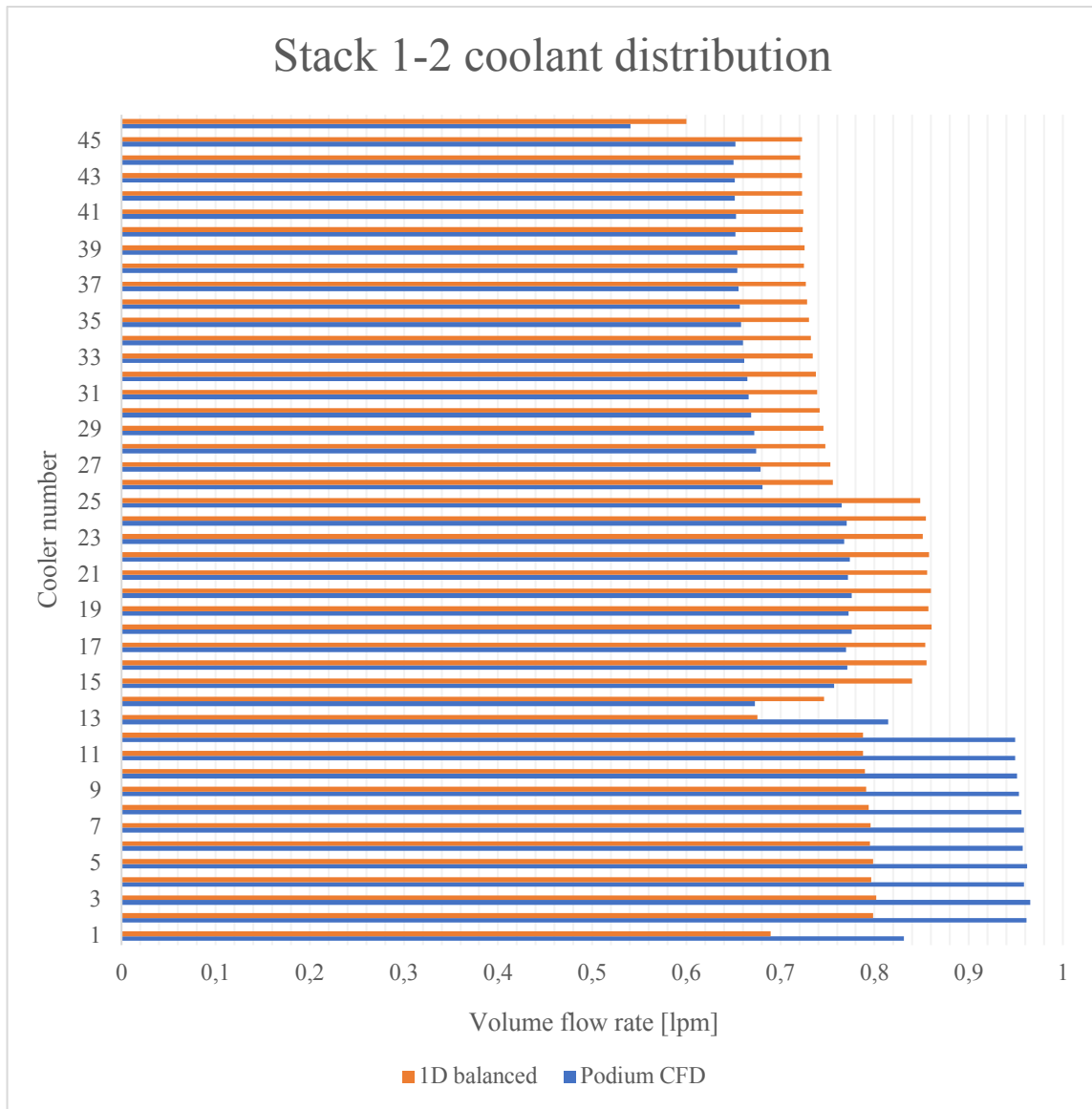
Where K_1 is equal to:

$$K_1 = \left[2.72 + \left(\frac{D_2}{D_1} \right)^2 \left(\frac{4000}{Re_1} \right) \right] \left[1 - \left(\frac{D_2}{D_1} \right)^2 \right] \left[\left(\frac{D_1}{D_2} \right)^4 - 1 \right]$$

And K_2 is equal to:

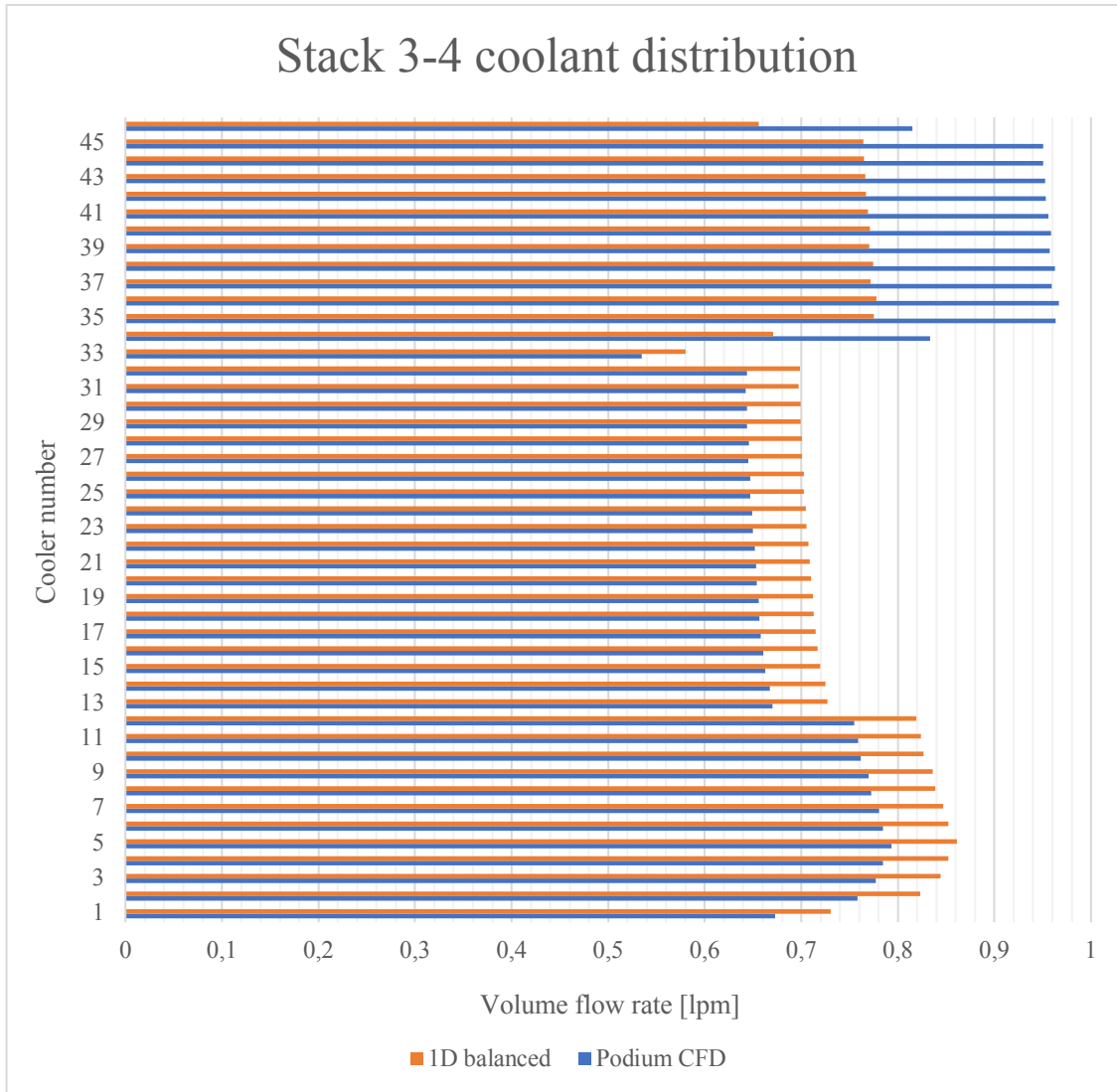
$$K_2 = 0.584 + \left(\frac{0.0936}{(L/D_2)^{1.5} + 0.225} \right)$$

Following the addition of the new hydraulic resistances downstream of the side stacks, the new flow distribution inside the coolers was evaluated through the lumped parameters model. The simulation results are shown in graphs 24 and 25.



Graph 24: Volume flow rate distribution of coolant in each cooler of stacks 1 and 2. The orange bars represent the distribution obtained by 1D model after hydraulic balancing while the blue bars by CFD simulation

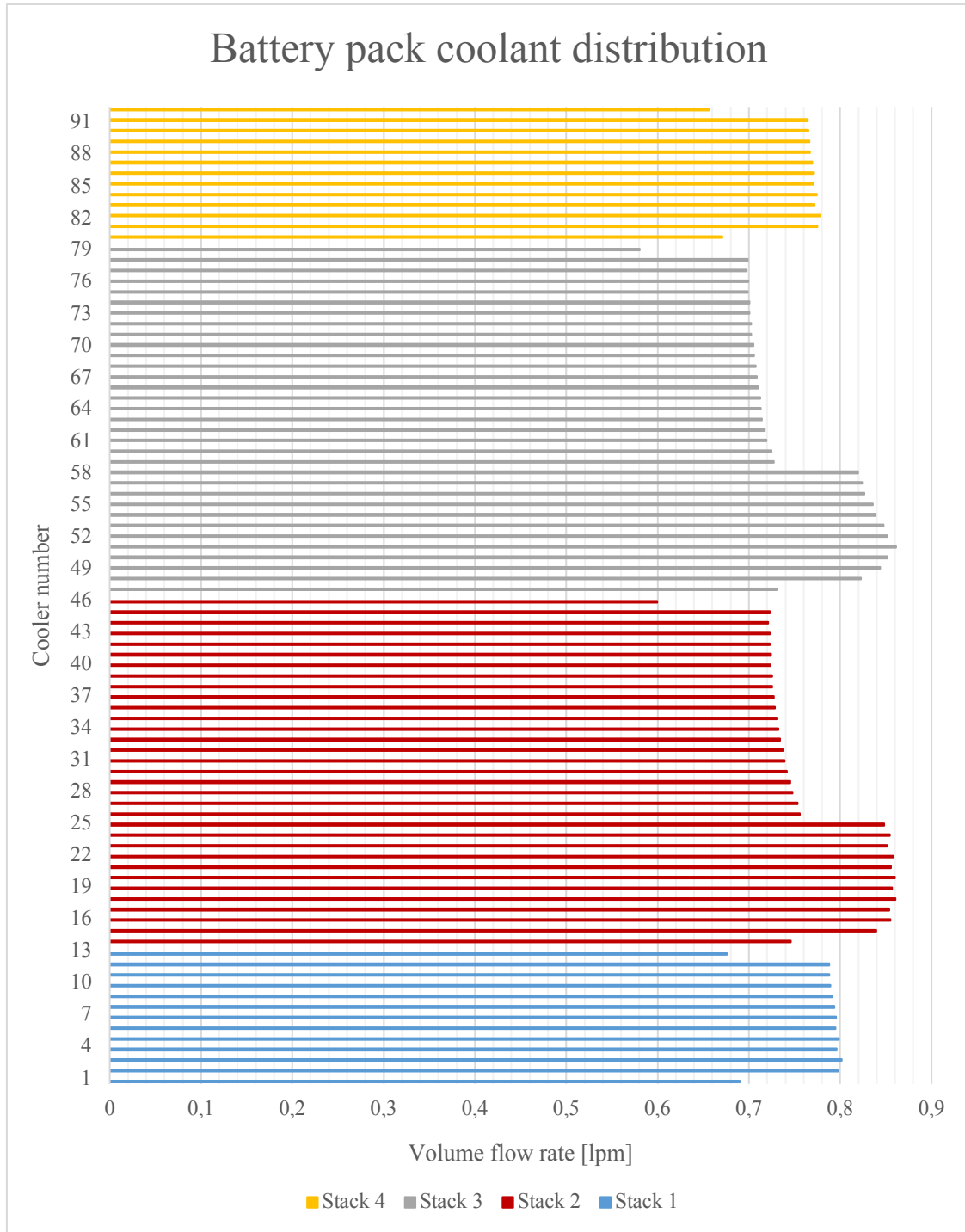
Graph 24 represents the distribution of the coolant flow inside the coolers of modules 1 and 2 in the pre-balancing (blue lines) and post-balancing (orange lines) configuration. It is easy to see how, following the balancing, the flow rate that flows inside the coolers is more homogeneous. In particular, the ratio between the flow rate inside the central coolers of the external module and the flow rate inside the central coolers of the internal module goes from 1.31 to 1.08.



Graph 25: Volume flow rate distribution of coolant in each cooler of stacks 3 and 4. The orange bars represent the distribution obtained by 1D model after hydraulic balancing while the blue bars by CFD simulation

Graph 25 represents the distribution of the coolant flow inside the coolers of modules 3 and 4 in the pre-balancing (blue lines) and post-balancing (orange lines) configuration. It is easy to see how, following the balancing, the flow rate that flows inside the coolers is more homogeneous. In particular, the ratio between the flow rate inside the central coolers of the external module and the flow rate inside the central coolers of the internal module goes from 1.37 to 1.1.

Full battery pack



Graph 26: Distribution of the coolant volume flow rate inside the battery pack coolers following balancing

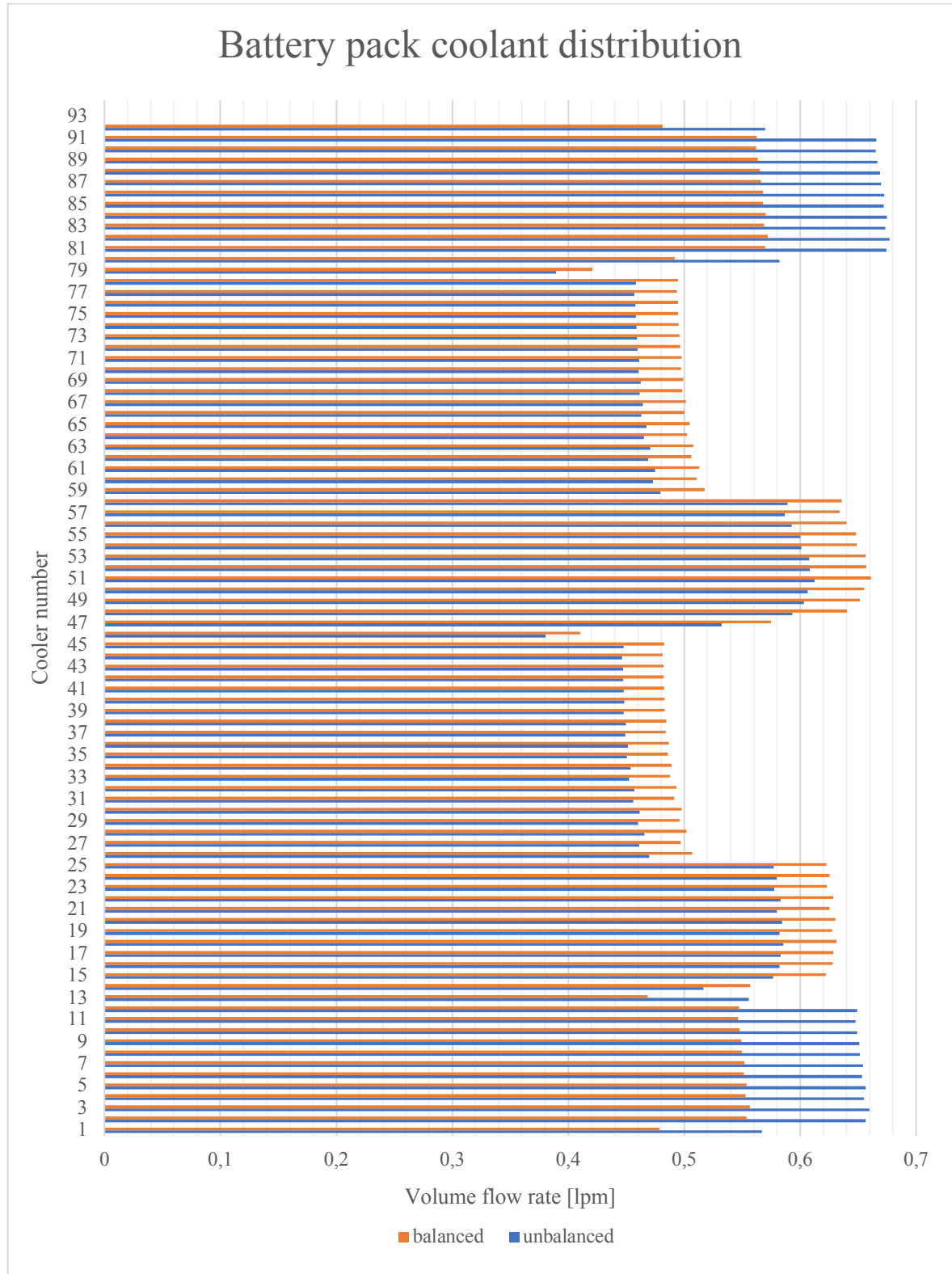
Graph 26 represents the flow distribution inside the battery pack in the final configuration. An homogeneous flow distribution is evident from the graph.

Volume flow rate	Value
QA [lpm]	34.5
QB [lpm]	35.5
Q4 [lpm]	9.8
Q3 [lpm]	24.7
Q2 [lpm]	25.4
Q1 [lpm]	10.1
Q3/Q4	2.52
Q2/Q1	2.52

Table 38: Volumetric flow rate of the coolant inside the battery pack modules following hydraulic balancing

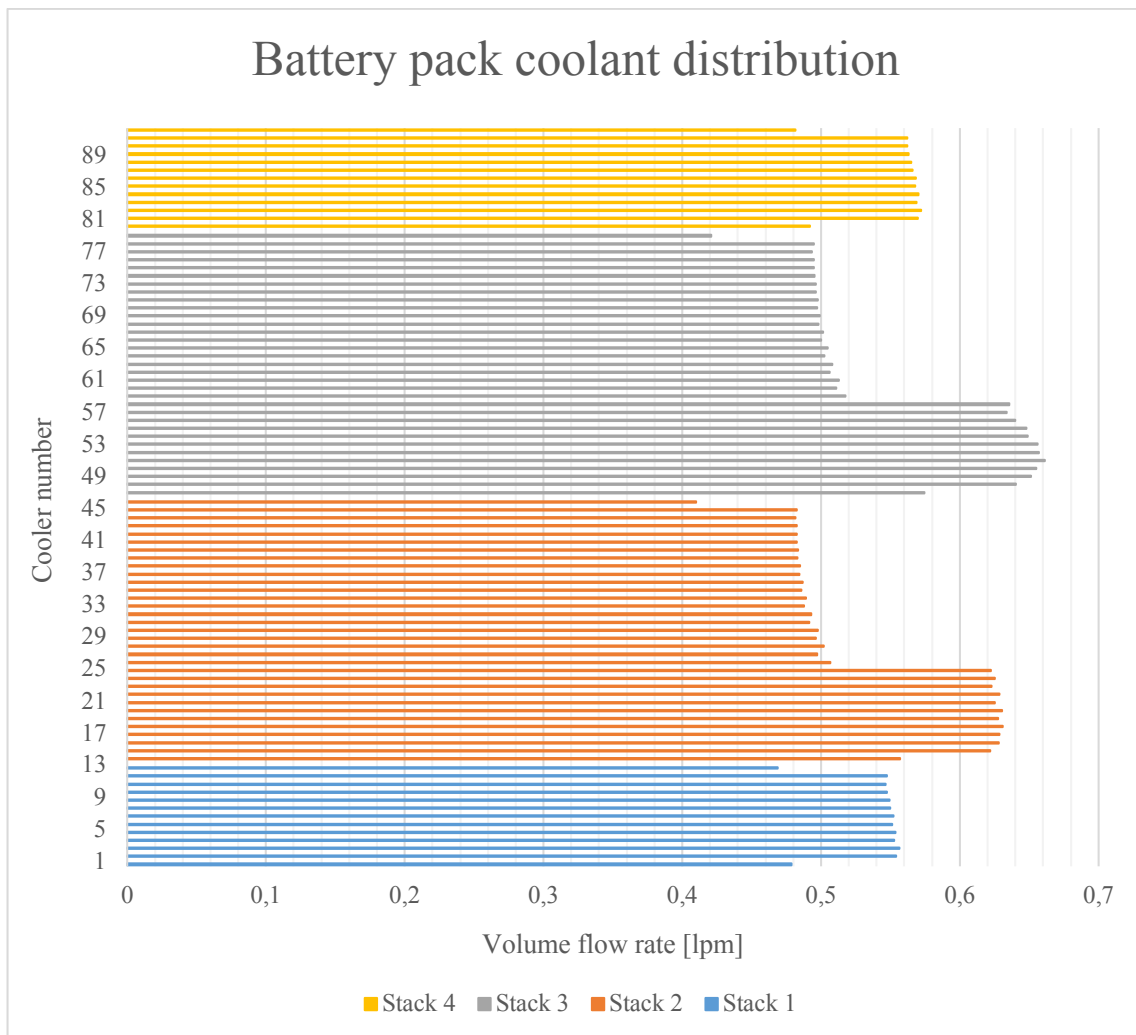
Table 38 indicates the flow rate values in each branch of the system. Stacks 1 and 2 receive 34.5 lpm of coolant while stacks 3 and 4 receive 35.5 lpm. The values of the Q3/Q4 and Q2/Q1 ratios equal to 2.52 provide confirmation that the hydraulic balancing has occurred correctly, leading to an optimal flow distribution.

3.4.4.3 Coolant volume flow rate at 50 lpm



Graph 27: Volume flow rate distribution of coolant in each cooler of battery pack. The orange bars represent the distribution obtained after balancing while the blue bars represent the unbalanced distribution

Graph 27 shows the distribution of the coolant flow rate that passes inside the coolers of the complete battery pack in the case of an inlet flow rate of 50 lpm. The blue bars represent the distribution before the balance. The orange bars show the distribution after balancing. Also in this case, the addition of the clamps downstream of the side modules leads to a significant improvement in the balance of the coolant flow rate with consequent homogeneity in the cooling of the cells. The ratio between the coolant flow inside the central coolers of the external module and those of the internal module goes from 1.37 of the initial configuration to 1.12 of the final configuration.



Graph 28: Distribution of the coolant volume flow rate inside the battery pack coolers following balancing

Full battery pack

Graph 28 shows the distribution of the coolant flow rate in each cooler of the battery pack following balancing.

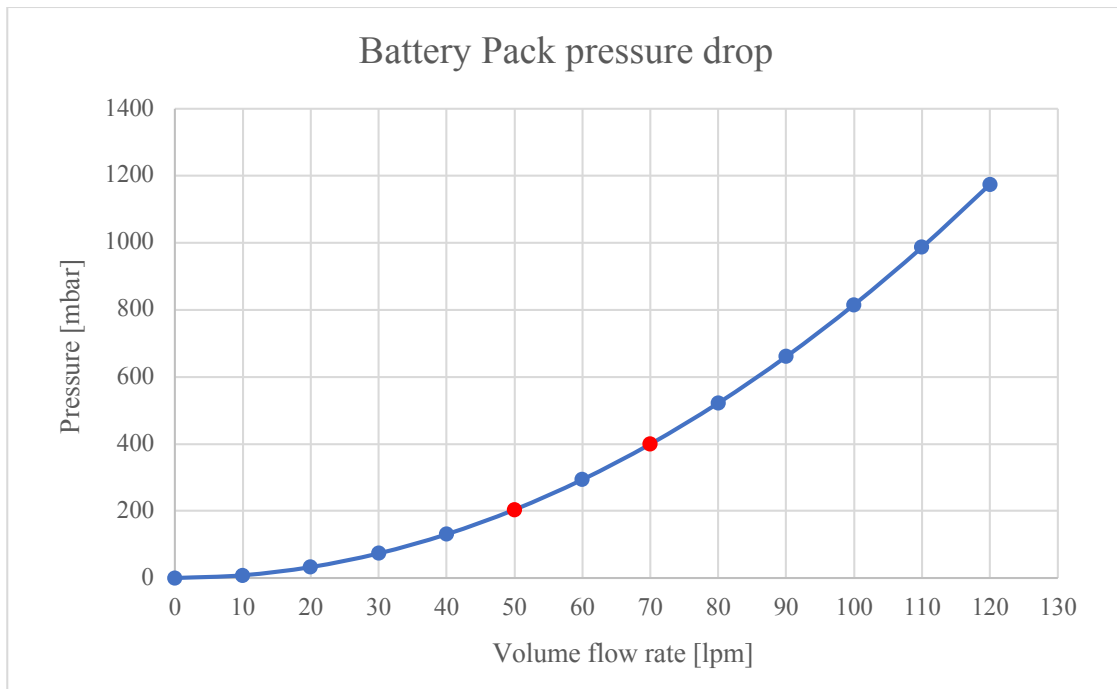
Table 39 indicates the flow rate values in each branch of the system. Stacks 1 and 2 receive 24.7 lpm of coolant while stacks 3 and 4 receive 25.3 lpm. The values of the Q3/Q4 and Q2/Q1 ratios equal to 2.52 and 2.51 provide confirmation that the hydraulic balancing has occurred correctly, leading to an optimal flow distribution.

Volume flow rate	Value
QA [lpm]	24.7
QB [lpm]	25.3
Q4 [lpm]	7
Q3 [lpm]	17.7
Q2 [lpm]	18.1
Q1 [lpm]	7.2
Q3/Q4	2.52
Q2/Q1	2.51

Table 39: Volumetric flow rate of the coolant inside the battery pack modules following hydraulic balancing

3.4.5 Total pressure drop

This subparagraph describes the trend of the pressure drop along the entire battery pack. The determination of the total pressure drop as a function of the coolant flow rate in the system is necessary for the correct choice of the pump.



Graph 29: Trend of the pressure drop along the battery pack as a function of the coolant volumetric flow rate

Graph 29 shows the pressure drop of the entire battery pack as a function of the coolant flow rate. The extremes of the operating range are shown in red (50 lpm and 70 lpm).

As can be seen from the graph, the pressure drop at the end of the operating range (70 lpm) is equal to 400 mbar. This value confirms the achievement of the project target which foresees not to exceed the threshold of 500 mbar at 70 lpm.

Full battery pack

Figure 61 represents the final layout of the battery pack cooling system. The choice of radiator and pump will be made later by the customer.

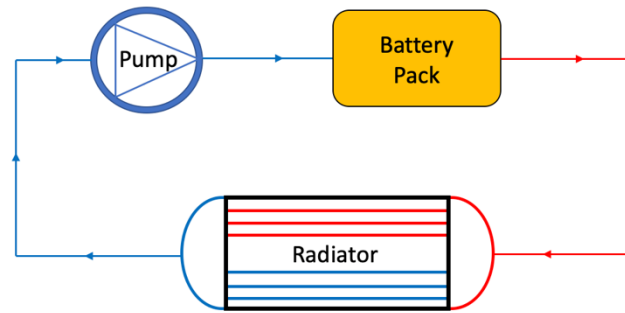
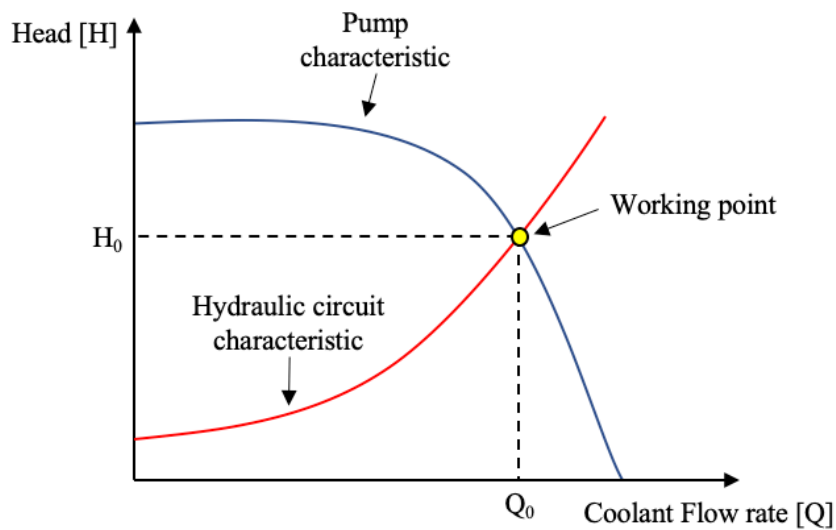


Figure 61: Schematic diagram of the complete cooling system of the battery pack inside the vehicle

After determining the pressure drop across the radiator and pipes, the customer can choose the pump according to the total pressure drop of the circuit (ΔP Battery Pack + ΔP Radiator + ΔP Piping).



Graph 30: Pump and hydraulic circuit characteristic curves

Graph 30 represents the trend of the hydraulic head of the pump and the circuit as a function of coolant flow rate. The blue curve represents the characteristic of the pump while the red one represents the characteristic of the circuit. After having determined the overall characteristic of the circuit (Battery Pack + Radiator + Pipes), the customer will have to insert in the system a pump with features able to achieve the desired working point.

4 CONCLUSIONS

This chapter summarizes the results obtained from the activities carried out in the BLIZZ PRIMATIST and P084 projects.

4.1 BLIZZ PRIMATIST

Project objective: Maximum cell temperature after 15 hours of charging < 30 °C.

Result obtained: Maximum cell temperature after 15 hours of charging equal to 26.5 °C.

The cooling system created for the BLIZZ PRIMATIST vehicle has achieved the fixed goal by bringing it to a maximum cell temperature of 26.5 °C. The lumped parameter model used to simulate the behaviour of the cooling system was found to be effective, leading to an error on the measurement of the maximum cell temperature after 15 hours of charging equal to 1.4 °C.

4.2 PROJECT P084

Project objective:

- Maximum pressure drop in the system: 500 mbar at 70 lpm.
- Stacks coolant flow rate ratio equal to 2.5 at 50 lpm and 70 lpm.

Result obtained:

- Maximum pressure drop in the system: 400 mbar at 70 lpm.
- Stacks coolant flow rate ratio equal to 2.52 at 50 lpm and 70 lpm.

The fluid dynamics analysis carried out on the cooling system of the P084 project confirmed the pressure drop values along the coolers provided by the suppliers. The thermo-fluid dynamics simulations and the thermal models with lumped parameters have demonstrated the effectiveness of the simplified battery pack cooling system. The fluid dynamics simulations and the lumped parameters hydraulic model of the complete battery pack allowed to correctly balance the coolant flow rates in the circuit, obtaining the ratio of 2.52 between the flow in the central and lateral stacks. The models created confirm the achievement of the project target with respect to the maximum pressure drop in the complete system. At 70 lpm the maximum pressure drop is 100 mbar lower than the expected limit.

References

- [1] Ahmad, P., Shriram, S., Gi-Heon, K. (2013). Large Format Li-Ion Batteries for Vehicle. 30th International Battery Seminar. Florida.
- [2] Alawee, W., H., Almolhem, Y., A., Yusuf, B., Mohammad, T., A., Dhahad, H., A. (2020). Variation of Coefficient of Friction and Friction Head Losses Along a Pipe with Multiple Outlets. *Water*, 12, 844. Retrieved from <https://www.mdpi.com/2073-4441/12/3/844/pdf>.
- [3] Bagabir, A. M., Khamaj, J. A., Hassan, A. S. (2013). Numerical Study of Turbulent Periodic Flow and Heat Transfer in a Square Channel with Different Ribs. *Journal of Applied Mathematics and Physics*, 1, 65-73.
- [4] Bravo, R. (2006). Using Equation Solver Programs to Teach Design of Pipe Networks. Tri-State University. 2006-1702. Retrieved from <https://peer.asee.org/using-equation-solver-programs-to-teach-design-of-pipe-networks.pdf>.
- [5] Han, J. C., Glicksman, L. R., Rohsenow, W. M. (1978). An investigation of heat transfer and friction for rib-roughened surfaces. *International Journal of Heat and Mass Transfer*, 21(8), 1143-1156.
- [6] Incropera, F., P., et al. (2011). Introduction to heat transfert sixth edition. Jefferson City: Wiley and sons.
- [7] Kalenik, M., Chalecki, M., Wichowski, P. (2020). Real Values of Local Resistance Coefficients during Water Flow through Welded Polypropylene T-Junctions. *Water* 2020, 12, 895. Retrieved from <https://www.mdpi.com/2073-4441/12/3/895>
- [8] Kudela, H. (n.d). Pipeline systems. Hydraulic losses in pipes. Retrieved from http://www.itcmp.pwr.wroc.pl/~znmp/dydaktyka/fundam_FM/Lecture_no7_Pipeline_Systems.pdf.

- [9] Makinejad, K., Arunachala, R., Arnold, S., Ennifar, H., Zhou, H., Jossen, A., Changyun, W. (2015). A Lumped Electro-Thermal Model for Li-Ion Cells in Electric Vehicle Application. *World Electr. Veh. J.* 7, 1-13. Retrieved from <https://doi.org/10.3390/wevj7010001>.
- [10] Maleki, H., Al Hallaj, S., Selman, J.R., Dinwiddie, R. B., & Wangb, H. (1999). Thermal Properties of Lithium-Ion Battery and Components. *Journal of The Electrochemical Society*, 146 (3), 947-954.
- [11] Munson, B., R., Okiishi, T., H., Huebsch, W., W., Rothmayer, A., P. (2013). *Fundamentals of fluid Mechanics*. USA: John Wiley & Sons, Inc.
- [12] Nerinckx, K., Vierendeels, J., & Dick, E. (2007). A mach-uniform algorithm: coupled versus segregated approach. *Journal of Computational Physics*, 224, 314-331.
- [13] OpenFOAM user guide Documentation. Retrieved from <https://www.openfoam.com/documentation/user-guide>.
- [14] Patel, P., D., Shah, K., N., Mahant, K., V., Yadav, C., O. (2013). Cfd Analysis Of Heat Exchanger Over A Staggered Tube Bank For Different Angle Arrangement Of Tube Bundles. *Int J Eng.* 2.
- [15] Roacher, P., J. (1994). Perspective: A Method for Uniform Reporting of Grid Refinement Studies. *Journal of Fluids Engineering*, 116(3), p. 405.
- [16] Roacher, P., J. (1997). Quantification of uncertainty in computational fluid dynamics. *Annual Review Fluid Mechanics*, 29, 123-160.
- [17] Sakib, S., Al-Faruk, A. (2018). Flow and Thermal Characteristics Analysis of Plate-Finned Tube and Annular-Finned Tube Heat Exchangers fo In-Line and Staggered Configurations. *Mechanics and Mechanical Engineering*, 22, 1407-1417.

References

- [18] Shabani, B., Biju, M. (2015). Theoretical Modelling Methods for Thermal Management of Batteries. *Energies*, 8, 10153-10177. Retrieved from <https://doi.org/10.3390/en80910153>.
- [19] Slater, J., W. (2021). Examining Spatial (Grid) Convergence. Retrieved from <https://www.grc.nasa.gov/WWW/wind/valid/tutorial/spatconv.html>.
- [20] Sundberg, J. (2006). Heat Transfer Correlations for Gas Turbine Cooling. Retrieved from <https://www.diva-portal.org/smash/get/diva2:21321/FULLTEXT01.pdf>.
- [21] Wilcox, D., C. (1993). *Turbulence Modeling for CFD*. La C nada: DCW Industries.